Dynamic Simulation of Power Systems using Three Phase Integrated Transmission and Distribution System Models: Case Study Comparisons with Traditional Analysis Methods

Himanshu Jain

Dissertation submitted to the faculty of the Virginia Polytechnic Institute and State University in partial fulfillment of the requirements for the degree of Doctor of Philosophy
In
Electrical Engineering

Robert P Broadwater, Chair
Saifur Rahman, Co-Chair
Alexander Elgart
Steve C Southward
Virgilio A Centeno

November 28, 2016
Blacksburg, VA

Keywords: Integrated Transmission and Distribution System Models, Dynamic simulations, Distributed Generation, Solar PV, Graph Trace Analysis

Dynamic Simulation of Power Systems using Three Phase Integrated Transmission and Distribution System Models: Case Study Comparisons with Traditional Analysis Methods

(Himanshu Jain)

ABSTRACT (academic)

Solar PV-based distributed generation has increased significantly over the last few years, and the rapid growth is expected to continue in the foreseeable future. As the penetration levels of distributed generation increase, power systems will become increasingly decentralized with bi-directional flow of electricity between the transmission and distribution networks. To manage such decentralized power systems, planners and operators need models that accurately reflect the structure of, and interactions between the transmission and distribution networks. Moreover, algorithms that can simulate the steady state and dynamics of power systems using these models are also needed. In this context, integrated transmission and distribution system modeling and simulation has become an important research area in recent years, and the primary focus so far has been on studying the steady state response of power systems using integrated transmission and distribution system models.

The primary objective of this dissertation is to develop an analysis approach and a program that can simulate the dynamics of three phase, integrated transmission and distribution system models, and use the program to demonstrate the advantages of evaluating the impact of solar PV-based distributed generation on power systems dynamics using such models. To realize this objective, a new dynamic simulation analysis approach is presented, the implementation of the approach in a program is discussed, and verification studies are presented to demonstrate the accuracy of the program. A new dynamic model for small solar PV-based distributed generation is also investigated. This model can interface with unbalanced networks and change its real power output according to the incident solar irradiation. Finally, application of the dynamic simulation program for evaluating the impact of solar PV units using an integrated transmission and distribution system model is discussed.

The dissertation presents a new approach for studying the impact of solar PV-based distributed generation on power systems dynamics, and demonstrates that the solar PV impact studies performed using the program and integrated transmission and distribution system models provide insights about the dynamic response of power systems that cannot be obtained using traditional dynamic simulation approaches that rely on transmission only models.

Dynamic Simulation of Power Systems using Three Phase Integrated Transmission and Distribution System Models: Case Study Comparisons with Traditional Analysis Methods

(Himanshu Jain)

ABSTRACT (public)

To ensure that electricity is delivered to consumers in a reliable manner, power system planners and operators rely on computer-based modeling and analysis of the electric grid. The software currently being used for this purpose are designed to simulate either the high voltage transmission networks, or the low voltage distribution networks. Till now these software have worked well as the electricity flow in the electric grid is largely unidirectional, from the transmission network to the distribution network. Neglecting the distribution network topology in transmission network models or vice-versa in such a structure of the electric grid does not introduce significant calculation errors. However, the rapid growth of consumer-owned and operated solar photovoltaics (PV) based distributed generation over the last few years, which is expected to continue in the foreseeable future, has necessitated a rethink of this modeling and analysis paradigm. As the penetration levels of distributed generation increase, the electric grid will become increasingly decentralized and there will be bi-directional flow of electricity between the transmission and distribution networks. Accurate analysis of such a decentralized electric grid cannot be performed if either the distribution or the transmission network topology is neglected in the models. Integrated transmission and distribution system modeling and simulation, where transmission and distribution networks are modeled as one single unit, has, therefore, become an important research area in recent years.

This dissertation makes a contribution to this research area by presenting an analysis approach and a program that can be used to simulate the dynamics (time varying behavior of the electric grid when subjected to disturbances such as short-circuits) of integrated transmission and distribution system models. A dynamic model of solar PV-based distributed generation that can be used to simulate their behavior during dynamic simulations is also investigated. Finally, an application of the program is discussed where the impact of solar PV-based distributed generation on the dynamics of the electric grid is studied by using the solar PV model and an integrated transmission and distribution system model.

The dissertation shows that by simulating integrated transmission and distribution system models using the dynamic simulation program, insights about the impact of solar PV-based distributed generation on the dynamics of the electric grid can be obtained, which the transmission only models cannot provide.

DEDICATION

This dissertation is dedicated to my grandmother, Smt. Rajkumari Jain, who passed away earlier this year. Without her love, affection and blessings I would not have been able to complete this work.

ACKNOWLEDGEMENT

Words are not enough to express my gratitude and appreciation to my advisor, Dr. Robert Broadwater, for his guidance and support all through the PhD. Dr. Broadwater was a constant source of encouragement and made the PhD fun, and a great learning experience. I also want to thank Dr. Saifur Rahman, Dr. Alexander Elgart, Dr. Steve Southward, and Dr. Virgilio Centeno for serving on my committee and promptly providing any guidance and help that I needed.

I want to acknowledge the constant support of my parents, Mr. Hemant Kumar Jain and Mrs. Sunita Jain, who ensured that I had everything I needed to do well in studies. I also want to thank my younger brother, Akshay Kumar Jain, who was always there to help me.

Finally, I want to say a big thank you to my wife, Surabhi, who stood like a wall behind me and took care of all other responsibilities so that I could focus on my research. I cannot thank her enough for the support she provided during the PhD, and for being incredibly patient with me.

Table of Contents

List of Figures

List of Tables

CHAPTER 1: INTRODUCTION AND LITERATURE REVIEW

The objective of this chapter is twofold. First, discuss the current approaches for modeling and simulation of power systems and highlight their limitations in addressing the analysis challenges posed by the rapidly de-centralizing electric grid. Second, introduce dynamic simulation of power systems using three phase integrated transmission and distribution system models as a new analysis approach that can address the limitations of existing methods. This chapter will set the stage for more detailed discussions about the presented method and its applications to be explored in the following chapters.

1.1 Brief History of Power Systems Analysis

The primary objective of the electricity network, or the electric grid, is to provide reliable (e.g., minimum outages) and good quality (e.g., minimum voltage fluctuations) electricity to consumers. Electric grids (used interchangeably with power systems hereafter) are often very large, and it is not possible to duplicate them in laboratories. Computer based models of power systems are therefore used universally to study their steady-state and dynamic behaviors.

Since the early days of computer based modeling and simulation of power systems, the model of the electric grid is divided into two distinct networks – Transmission System and Distribution System. The transmission system is characterized by high voltages (typically 69 kV or above); multiple power generation sources (e.g., thermal, nuclear and wind power plants); networked topology; and a low resistance to reactance ratio (R/X ratio) of lines. The distribution system on the other hand is a low voltage network with radial (typically) topology, single source of power, and high R/X ratio of lines. It is important to note that the electric grid is a single network, from the very high voltage transmission lines to the low voltage service mains that supply consumers. If the electric grid is one large network, why do the models not reflect this reality? The answer to

this question is twofold; historic design of the power systems, and relatively higher importance accorded to the simulation of transmission systems.

The high voltage transmission network was historically designed to be physically and electrically balanced. All the generators that supplied power to the grid were designed such that the three phase voltages generated were nearly equal in magnitude and had phase angles that were symmetrically placed around a circle. Similarly, many transmission lines were transposed (i.e., each phase occupied the position of other two phases for equal distance over the length of the line) [1], so that each phase had the same average inductance, which resulted in nearly balanced voltages across the transmission network. The distribution networks on the other hand were physically unbalanced with single phase, two phase and three phase lines (typically un-transposed) and loads.

As the transmission network(s) became increasingly interconnected, it became necessary to develop software for helping to ensure safe and reliable operation. A lot of effort was spent on developing transmission system models and algorithms that could analyze these models. As a result of these efforts, optimally ordered triangular factorization based Newton Raphson methods for power flow analysis [2]-[5], and partitioned solution approaches based differential algebraic equation solvers for simulating power systems dynamics [6], [7] were developed in the late 60s and early 70s and quickly became the norm for the modeling and simulation of transmission systems. These methods continue to be widely used in power systems analysis programs [8].

Distribution systems on the other hand continued to be planned and operated with little or no analysis, even when analysis based planning and operations of the transmission systems had become the norm [9]. In the 80s and 90s, however, research into developing algorithms for modeling and analyzing distribution systems gathered pace. It was observed that the algorithms that were used to analyze the transmission systems could not be used to solve distribution systems

due to their poor convergence on distribution networks [9]. Therefore, separate algorithms for analyzing distribution networks were developed that exploited the radial topology of most distribution networks. The most successful of these algorithms was based on the forward/backward sweep methods, where voltages were calculated during the forward sweep and currents were calculated in the reverse sweep [9], [10]. Reference [11] extended the forward/backward sweep method by presenting an algorithm that could be used to analyze weakly meshed transmission and distribution networks. The authors in [11] noted that as the number of loops increased, the efficiency of their program decreased, and the potential for divergence of the algorithm increased. As a result, the practical applicability of the method was restricted to weakly meshed distribution and transmission systems. Almost all the distribution analysis programs being used today are based on forward/backward sweep methods [12].

The above discussion shows that the development of analysis algorithms for transmission and distribution systems took place independently, and algorithms developed for transmission networks have not proven to be successful for solving distribution networks and vice versa. Till recently, the need was not felt for analyzing transmission and distribution systems together, and hence separate software for analyzing transmission and distribution networks were considered to be adequate. However, with the rapid increase in the adoption of distributed generation (DG) at the distribution level, there is an increasing need for integrated transmission and distribution network models, and algorithms that can analyze such models.

1.2 Distributed Generation: Need for Integrated Transmission and Distribution Systems Analysis

DG refers to those sources of electricity that are significantly smaller than the centralized power generation facilities and that are typically connected at low voltages, at or near the locations where

electricity is consumed [13]. DG has grown rapidly in the last few years, and the rapid growth is expected to continue over the next decade [14]. Of the various DG technologies, solar photovoltaics, or solar PV, has elicited the most interest. This is due to the commercially and technologically mature status of solar PV generation, which puts it far ahead of other renewable energy based DG technologies [15]. In the rest of the dissertation, solar PV will refer to solar PV-based DG unless otherwise specified.

Solar PV differs from conventional power generation sources in three ways. First, the "fuel" for solar PV, i.e., solar irradiation, cannot be controlled. Second, nominal frequency[1] alternating current is synthesized from the direct current generated by the solar panels using power electronics based inverters. Third, there is no rotating mass in solar PV. The intermittency of solar PV output increases the difficulty of balancing demand and supply. Moreover, during a severe disturbance, such as the loss of a large power plant or load, the kinetic energy of synchronous generators is naturally converted into electrical energy to maintain the demand/supply balance, and the rotating mass inertia prevents the system frequency from changing rapidly. The concern with increasing penetration of solar PV is that as the synchronous generators are displaced, the system inertia will reduce, resulting in larger frequency excursions during disturbances, which can adversely impact stability [16].

As a result, many authors have attempted to study the impact of DG on power system stability in recent years [17]. Many of these studies assume the distribution systems to be balanced [18], [19], and/or use small distribution networks to test their approaches [20]-[22]. In [23], authors used PSCAD/EMTPDC software to perform transient stability studies on a very small distribution network. Authors in [24] studied the impact of DG using a balanced transmission network model,

[1] Nominal frequency in the dissertation refers to the 60 Hz power system frequency used in the US.

which allowed them to use traditional dynamic simulation programs that need balanced network topology for simulating power systems dynamics. Moreover, DG, which is added in the distribution system, was lumped at the transmission buses, which prevents the impacts of spatially diverse DG units to be considered in the simulations. References [25]-[30] are other recent papers and reports in which the impact of solar PV generation on power system dynamics has been studied using transmission system models. These studies provide interesting insights about the impact of disturbances, such as faults, generator trips, and changes in solar irradiation [29] on the dynamic response of the power system. The impact of various control capabilities of solar PV generators, such as unity power factor operation, automatic voltage control, and frequency control are also studied [25], [26] and [29]. Similar to [24], however, the two common assumptions made in these studies are – (i) use of traditional dynamic simulation programs that need positive sequence transmission only models to represent network topology; (ii) aggregation of distribution connected solar PV generation at transmission buses. These assumptions limit the scope of the analyses to assess the impact of PV. For example, it is not possible to study the impact of solar PV-based distributed generators on the dynamic response of the distribution system in which these generators are connected. Similarly, the impact of cloud induced solar transients that affect each solar PV unit differently within a distribution network cannot be accurately studied.

This discussion shows that even though solar PV is being added to the distribution systems, and there is interest in evaluating its impact on the dynamics of power systems (both the transmission and distribution systems), the research so far has continued to treat the power system as two distinct sets – transmission and distribution. There is, therefore, a need for developing new dynamic simulation methods that can model and analyze integrated transmission and distribution system models, and provide accurate assessment of the impact of DG on power systems dynamics.

1.3 Studying Power Systems Dynamics using Three Phase Integrated Transmission and Distribution System Models

Limited research has been performed on modeling and analyzing integrated transmission and distribution systems. References [31]-[33] discuss integrated T&D modeling of large networks. While the transmission lines are not assumed to be transposed in [31], references [32] and [33] assume transposition of transmission lines, as indicated by the choice of the positive sequence power flow solvers used for simulating the transmission system. Although the transmission network is typically assumed to be balanced, this assumption is not particularly valid for integrated transmission and distribution models, because connecting an unbalanced distribution system to a transmission bus will automatically propagate the unbalance into the transmission system. Moreover, many transmission lines, particularly the newer lines, are not transposed [34]-[38], and assuming so can result in simulation errors and missing potentially adverse power system events [38]. In addition, the response of various transformer configurations to unbalance cannot be accurately modeled. Therefore, power systems modeling and simulation using integrated T&D models necessitates creation of three phase transmission models that do not assume balance.

In addition, [31]-[33] evaluate only the steady state behavior of power systems using integrated T&D models. The ability to simulate dynamics (slow, electromechanical transients) of integrated T&D models, however, is critical for evaluating the stability of power systems, particularly in the presence of DG as discussed above. The literature review suggests that, except for the electromagnetic transient programs, no programs exist that can be used to simulate the dynamics of power systems using three phase, integrated T&D system models. The existing electromagnetic transient programs, however, have system size and speed limitations that make them unattractive for studying electromechanical transients in real world power systems using their integrated T&D

models. Electromagnetic transient programs require a small integration time step for solving the stiff systems of differential equations that arise from time domain modeling of electric networks and electric machines, which significantly increases the simulation time for studying slow, electromechanical transients. For example, [39] shows that an electromagnetic transient simulation program required 32 minutes to simulate 11 nominal frequency cycles in one distribution network containing around 2,300 three phase nodes. Even a small integrated transmission and distribution system model can have many more nodes [17], [31], which suggests that the time required to simulate electromechanical transients in such systems using electromagnetic transient programs can be prohibitive.

1.4 Objective of the Dissertation

The discussion is this chapter has highlighted two major deficiencies in existing power systems modeling and simulation approaches:

(i) Lack of a software tool that can simulate dynamics of power systems using three phase, integrated transmission and distribution system models; and

(ii) The consequent inability to accurately evaluate the impact of solar PV on the dynamics of power systems.

The objective of this dissertation is to address these limitations by providing a new approach to dynamics analysis that facilitates analysis of the impacts of distributed generation resources, particularly solar PV, on the dynamics of power systems.

1.5 Organization of the Dissertation

The rest of the dissertation is organized into six chapters. A brief description of the chapters is given below:

Chapter 2: This chapter discusses the fundamentals of graph trace analysis, which is the network modeling and simulation approach used in the Distributed Engineering Workstation (DEW) software [40]. Since DEW is used as the network algebraic equations solver in the dynamic simulation program presented in the dissertation, the basic concepts of solving radial and looped electric circuits with graph trace analysis are discussed in this chapter.

Chapter 3: This chapter presents the program that can simulate the dynamics of power systems using three phase integrated transmission and distribution network models. The algorithm behind the program, its key features and limitations are discussed in detail in this chapter.

Chapter 4: This chapter presents a dynamic model of small solar PV units that can interface with balanced and unbalanced networks during dynamic simulations. The need for developing this model, its key features, and the equations used to control the real and reactive powers generated by the model are discussed in the chapter.

Chapter 5: Chapter 5 presents a number of studies that were performed to verify the dynamic simulation program and the dynamic solar PV model that were developed in chapters 3 and 4, respectively. The verification is performed with software that are widely used in the power systems industry.

Chapter 6: The objective of this chapter is to demonstrate the application of the dynamic simulation program in evaluating the impact of solar PV-based DG on the dynamics of power systems. Through a series of case studies, the advantages of using integrated transmission and distribution system models for evaluating the impact of solar PV-based DG are highlighted.

Chapter 7: This chapter summarizes the work presented in the dissertation and provides recommendations for future research using integrated transmission and distribution system models.

CHAPTER 2: FUNDAMENTALS OF GRAPH TRACE ANALYSIS BASED POWER FLOW ANALYSIS PROGRAMS

2.1 Introduction

This chapter discusses the fundamental concepts behind Graph Trace Analysis (GTA) based power flow analysis programs that have been used for analyzing transmission, distribution and integrated transmission and distribution models of power systems for more than two decades [17], [41]-[44]. The discussion in this chapter is important as the GTA based power flow analysis engine of the Distributed Engineering Workstation (DEW) software is used in the three phase dynamic simulation program which will be discussed in the next chapter.

This chapter will first discuss the concept of edge-edge graphs that are fundamental to writing GTA based algorithms. The approach for writing power flow analysis algorithms using the edge-edge graphs of electric networks will be discussed next. Finally, iterative equations developed using GTA will be presented and used to solve a number of simple electric circuits to solidify the concepts discussed, and demonstrate the accuracy and convergence characteristics of GTA based power flow analysis algorithms.

2.2 Edge-Edge Graphs: An Alternative to Matrix-based Modeling and Storage of Electric Networks

The analysis of electric networks begins with storing their topology and parameters of their constituents in computers. Two commonly used ways of storing graphs are matrices and lists [45]. Electrical engineers are most familiar with the matrix approach for storing graphs, using adjacency and incidence matrices. In real world networks the degree of any node (number of edges incident on a node) is much smaller than the number of nodes in the network, which results in sparse adjacency and incidence matrices, and sparse matrix storage schemes are typically used to reduce

the memory storage requirements. Algorithms that exploit the sparsity of matrices to efficiently analyze networks have been developed [2]-[4].

Lists offer a more efficient way of storing sparse networks [45], as they only store the edges that exist. In other words, lists inherently exploit the sparse structure of real world networks. Adjacency Lists and Adjacency Multi-Lists are the two commonly used forms of storing graphs as lists [46]. In this section, an alternative approach to storing graphs as lists is presented, which only uses the edges, and not any nodes, to store a graph. Such a graph is referred to as an edge-edge graph. By storing edges of an edge-edge graph in an appropriate order, algorithms can be written to analyze real world networks without creating, storing and manipulating large matrices. This approach of writing algorithms is discussed in some detail in the next section. The rest of this section focuses on creating edge-edge graphs and demonstrating the inherent sparsity of these graphs.

2.2.1 Obtaining the Edge-Edge Graph of a Network

In this section a method for converting a graph, which is given as a node-edge graph (each edge defined by its starting and ending nodes) into an edge-edge graph is discussed. The method is by no means the only one that may be used, or the optimal one, for creating edge-edge graphs. However, it is designed such that the steps are easy to follow; the terminology and algorithms used in each step is known to electrical and computer engineers; and the resulting graph can be analyzed simply by tracing through it (i.e., by accessing each edge of the graph in a specified order). Interested readers are encouraged to explore other ways of creating edge-edge graphs that can facilitate writing of graph trace based analysis algorithms.

The method used in this section to obtain an edge-edge graph involves the following three steps:

- Obtain a spanning tree (referred to as tree hereafter) of the graph, followed by its complementary spanning tree (referred to as cotree hereafter).
- For each edge of the tree, identify the adjacent edge that is closer to a reference source ("Source" in Fig. 1) and which provides the physical path back to the reference source. This edge is referred to as the "feeder path".
- For each edge in a cotree, identify the edges between which it is connected.

Fig. 1(b) and 1(c) show the tree and cotree of the graph of Fig. 1(a), respectively. The node numbers are in red while the edge numbers are in black and encircled. In Fig. 1, the feeder path for edges {2, 3, 4} is edge {1}, and the feeder path for edge {5} is edge {4}.

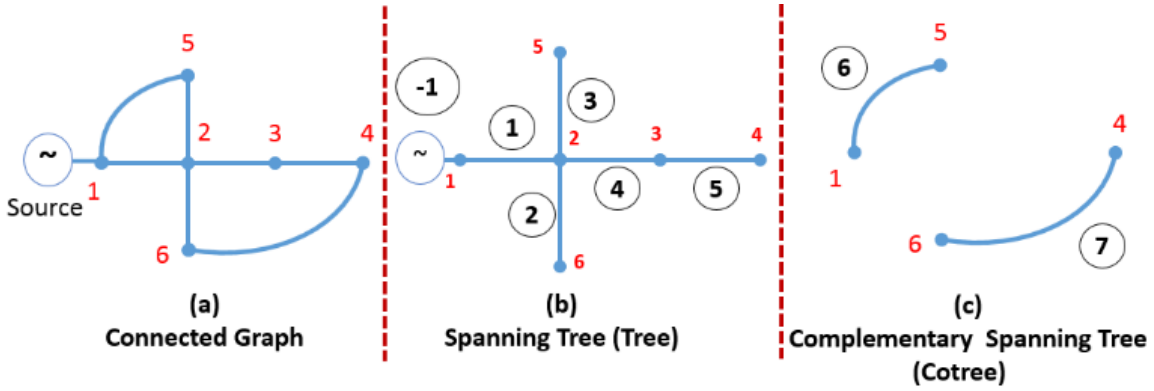

Fig. 1: Tree and Cotree of a Graph

It should be noted that for obtaining the edge-edge graph, any node can be selected as the reference source node. However, as will be discussed later, for network analysis using GTA the reference source node is always associated with a physical source of energy, such as an electric substation or a power plant. Therefore, the reference source node in Fig. 1 is node 1. Also note that each edge in the cotree forms exactly one loop in the graph. Therefore, there are as many loops in the graph as there are edges in a cotree [47]. This characteristic of graphs can be used to identify all the independent loop "through" variables (e.g., currents in electric networks [48]). This property is also evident from the graph of Fig. 1a that has two loops, which is the same as the number of

edges in its cotree. Steps A – C below illustrate obtaining an edge-edge graph from node-edge graph.

Step A: Obtaining the Spanning Tree of a Graph

The spanning tree of a node-edge graph can be obtained using either a depth-first search or a breadth-first search. Once a tree is obtained, the remaining edges form the cotree.

Step B: Assigning Feeder Paths to the Tree of the Graph

Once a tree is obtained, feeder paths are assigned to each edge of the tree. Feeder path assignment involves selecting a node (called the root node) and assigning the feeder path to all of its incident edges. This step is repeated continually till each edge in the tree has been traversed. The application of the feeder path assignment algorithm to the tree of Fig. 1(b) is discussed in detail below:

Step 1: Select a source as the reference source, which is also the first root node, and assign -1 as its corresponding feeder path. In the tree of Fig. 1(b), the first root node is 1. Node 1 is pushed on top of the stack (referred to as root node stack) along with its feeder path. The root node stack is now {1, -1}.

Step 2: Assign all of the edges incident on the root node the same feeder path. This feeder path is the edge number in the second column of the root node stack, corresponding to the current root node. Next, select an edge that is incident on the root node, and has not been used for branching before, and push its node (other than the current root node) to the top of the root node stack. Also store this edge's number as the feeder path corresponding to the node that was put on the top of the stack. The node at the top of the stack becomes the new root node. In the tree of Fig. 1(b), edge 1 is the only edge incident on node 1, hence the new root node is 2, and its corresponding feeder path is edge 1. Therefore, the root node stack becomes {2, 1; 1, -1}.

Step 3: Repeat step 2 with root node 2, while ensuring that the feeder path for edge 1 is not assigned again, as it has already been used for branching in step 2. The feeder paths assigned to edges {2, 3, 4} is edge 1. Select one of the three edges incident on node 2 that have not been used for branching yet. If edge 3 is selected, node 5 is pushed on top of the stack, edge 3 becomes its corresponding feeder path, and the root node stack becomes {5, 3; 2, 1; 1, -1}.

Step 4: Step 2 is repeated again. However, there is no incident edge for node 5 that has not been used for branching. Hence, the end of a tree branch is reached. Since the node stack is not empty, it means that the tree has not been completely traversed yet. Therefore, the root node at the top of the stack is popped out along with its feeder path. After this step, the root node stack becomes {2, 1; 1,-1}.

Step 5: Repeat step 2 with root node 2 but skip the feeder path assignment to incident edges of node 2, as that has been done earlier. Select one of two branches that have not been used for branching yet. If edge 2 is selected, node 6 is pushed on top of the stack along with the corresponding feeder path which is edge 2. The root node stack now becomes {6, 2; 2, 1; 1, -1}.

Step 6: Repeat step 2 with node 6 as the root node. However, as there is no edge incident on node 6 that has not been branched yet, node 6 is removed from the top of the stack along with the corresponding feeder path. The root node stack now becomes {2, 1; 1, -1}.

Step 7: Repeat step 2 with root node 2, but skip the feeder path assignment to incident edges of node 2, as that has been done earlier. The only remaining edge that has not been branched yet, edge 4, is selected. Therefore, node 3 and the corresponding feeder path, edge 4, are pushed on top of the root node stack, which now becomes {3, 4; 2, 1; 1 -1}.

Step 8: Repeat step 2 with the only incident branch on node 3 that has not been branched yet, edge 5, whose feeder path becomes 4. Node 4 becomes the new root node and the corresponding feeder path becomes edge 5. The root node stack becomes {4, 5; 3, 4; 2, 1; 1, -1}.

Step 9: On repeating step 2 again, since there is no unbranched edge left which is incident on root node 4, it is removed from the stack, and node 3 becomes the new root node. The root node stack now becomes {3, 4; 2, 1; 1, -1}.

Step 10: On repeating step 2 again, there is no unbranched edge left which is incident on root node 3, and thus node 3 is removed from the stack and node 2 becomes the new root node. The root node stack now becomes {2, 1; 1, -1}.

Step 11: Repeat step 2 with root node 2, but skip the feeder path assignment to incident edges of node 2, as that has been done earlier. Since there is no unbranched edge left which is incident on root node 2, it is removed from the stack and node 1 becomes the new root node. The root node stack now becomes {1, -1}.

Step 12: Repeat step 2 with root node 1 but skip the feeder path assignment to incident edges of node 1, as that has been done earlier. Since there is no unbranched edge left which is incident on root node 1, it is removed from the stack.

After the 12^{th} step, the root node stack is empty, indicating that the tree of Fig. 1(b) has been traversed and the feeder path assignment for the tree is complete. Table 1 shows the contents of the root node stack at each of the 12 steps that it took to assign feeder paths to the tree of Fig. 1(b). By following the node numbers in bold in Table 1, the path followed by the feeder path assignment algorithm can be traced. Table 2 gives the feeder paths assigned to each edge of the tree in Fig. 1(b), and shows that combination of edge numbers and corresponding feeder paths enable tracing through a tree without making an adjacency or an incidence matrix.

Table 1: Root Node Stack during Feeder Path Assignment for Fig. 1(b)

Step	Root Node Stack
1	{1,-1}
2	{2, 1; 1, -1}
3	{5, 3; 2, 1; 1, -1}
4	{2, 1; 1,-1}
5	{6, 2; 2, 1; 1, -1}
6	{2, 1; 1 -1}
7	{3, 4; 2, 1; 1 -1}
8	{4, 5; 3, 4; 2, 1; 1, -1}
9	{3, 4; 2, 1; 1, -1}
10	{2, 1; 1, -1}
11	{1, -1}
12	{}

Table 2: Edge-Edge Graph of Fig. 1(b)

Edge #	Feeder Path Index	Interpretation of the row
1	-1	Feeder path of edge 1 is edge -1
2	1	Feeder path of edge 2 is edge 1
3	1	Feeder path of edge 3 is edge 1
4	1	Feeder path of edge 4 is edge 1
5	4	Feeder path of edge 5 is edge 4

Step C: Identifying Adjacent Edges for each Cotree Edge

Once the feeder paths are assigned to the tree of a graph, the location of each cotree edge can be identified. Two indices are needed to uniquely mark the location of a cotree edge. These indices are the feeder paths of the two nodes at either end of a cotree edge. One of these two feeder path indices is called the cotree index to indicate that the branch forms a loop. During feeder path assignment to the tree, root nodes and the corresponding feeder paths can be saved in a separate variable and used for identifying the adjacent edges of each cotree edge. Applying this logic to the cotree of Fig. 1(c), the complete edge-edge representation for the graph of Fig. 1(a) can be obtained, which is shown in Table 3.

Table 3: Complete Edge-Edge Graph of Fig. 1(a)

Edge	Feeder Path Index	Cotree Index (0 implies edge does not belong to a cotree)
1	-1	0
2	1	0
3	1	0
4	1	0
5	4	0
6	-1	3
7	2	5

2.2.2 Comparing the Sparse Matrix of an Electric Network with its Edge-Edge Graph

To demonstrate the inherent sparsity of edge-edge graphs, the edge-edge graph of the IEEE 39 bus system [49] prepared using the method outlined above is compared with its adjacency matrix (created using the *sparse()* function of Matlab). Fig. 2 shows the tree and cotree edges of the IEEE 39 bus system, while Table IV shows the feeder path and cotree indices of its edge-edge graph (The tree and cotree pair are not unique).

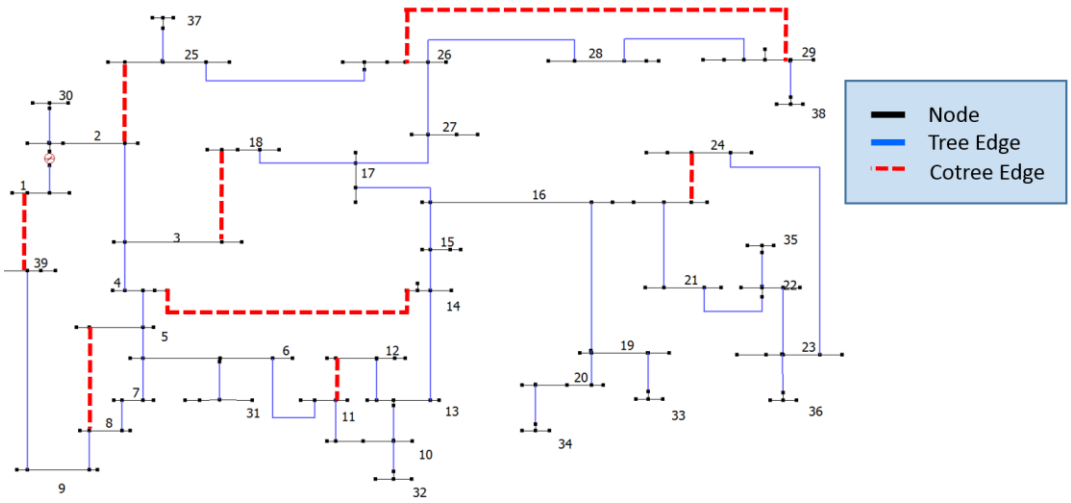

Fig. 2: Tree and Cotree of the IEEE 39 Bus System

Table 4 also shows that the space needed to store the IEEE 39 bus system is 46X3 units which is the same as that needed using the coordinate (COO) sparse matrix format (since there are 46 edges in the 39 bus system). This is expected, as the edge-edge graph only stores the edges that exist.

Table 4: Edge-Edge Graph of the IEEE 39 Bus Network Topology

From Node	To Node	Edge #	Feeder Path	Cotree Index	From Node	To Node	Edge #	Feeder Path	Cotree Index
1	2	1	-1	0	14	15	18	17	0
1	39	39	-1	12	15	16	19	18	0
2	3	2	1	0	16	17	20	19	0
2	30	3	1	0	16	19	21	19	0
2	25	40	1	33	16	21	22	19	0
3	4	4	2	0	16	24	44	19	31
3	18	41	2	23	17	18	23	20	0
4	5	5	4	0	17	27	24	20	0
4	14	42	4	17	19	20	25	21	0
5	6	6	5	0	19	33	26	21	0
5	8	43	5	10	21	22	28	22	0
6	7	7	6	0	26	27	35	24	0
6	11	8	6	0	20	34	27	25	0
6	31	9	6	0	22	23	29	28	0
7	8	10	7	0	22	35	30	28	0
10	11	13	8	0	23	24	31	29	0
8	9	11	10	0	23	36	32	29	0
9	39	12	11	0	25	37	34	33	0
10	13	14	13	0	25	26	33	35	0
10	32	15	13	0	26	28	36	35	0
12	13	16	14	0	26	29	45	35	37
13	14	17	14	0	28	29	37	36	0
12	11	46	16	8	29	38	38	37	0

Another advantage of edge-edge graphs is that no special treatment is needed to store networks with parallel edges. This is not the case if matrices are used to store graphs. For instance, since the IEEE 39 bus system does not have parallel edges, the adjacency matrix was able to represent the entire network. However, if parallel edges existed (e.g., double circuit lines in electric networks), an incident matrix would be needed for storing the graph as a matrix, since an adjacency matrix cannot uniquely identify the presence of multiple edges between two nodes. Since an incident matrix is not symmetric, it may need more storage space than the adjacency matrix. For example, the sparse incidence matrix of the IEEE 39 bus system needs 92X3 units of storage (using the *sparse()* function of Matlab). Special treatment of networks with parallel edges is not needed in

the edge-edge graphs, as each edge is uniquely identified by its edge number. The resulting efficiency of storage becomes particularly important for large networks.

2.3 Edge-Edge Graphs and GTA

Using the tree of Fig. 1(b), it will now be shown how "across" and "through" quantities in a radial network can be obtained by the application of GTA to its edge-edge graph.

2.3.1 Re-assigning Edge Indices and Solving Radial Circuits using GTA

The edge-edge graph of the tree shown in Fig. 1(b) was obtained using the 12 steps given in Table 1. If an index is assigned to an edge the first time it is used for branching, and the index is incremented every time a new edge is reached while tracing the graph, this index can uniquely identify each edge. Let this index be called the forward trace index, and the set of forward trace indices can be used to replace the earlier edge numbers and feeder path indices. The new edge numbers, which are the same as forward trace indices, and the new feeder path indices for the graph of Fig. 1(b) are shown in Fig. 3. The assignment of forward trace indices using this logic makes it very simple to calculate the "across" and "through" variables of a network by tracing through the graph in the ascending and descending order of its forward trace indices, respectively. An example of calculating the "across" and "through" variables is discussed next.

Let it be assumed that the network to be analyzed is an electric network and has the radial topology of the graph of Fig. 3. Any real electric network will have loads connected at the end of some of the edges. Addition of loads does not change the network topology, or the number of voltages that should be calculated. However, the number of currents that need to be calculated increase. Therefore, loads are treated as an edge during the conversion of a node-edge graph into an edge-edge graph, and the feeder path, cotree and forward trace indices are assigned in the same manner as discussed earlier.

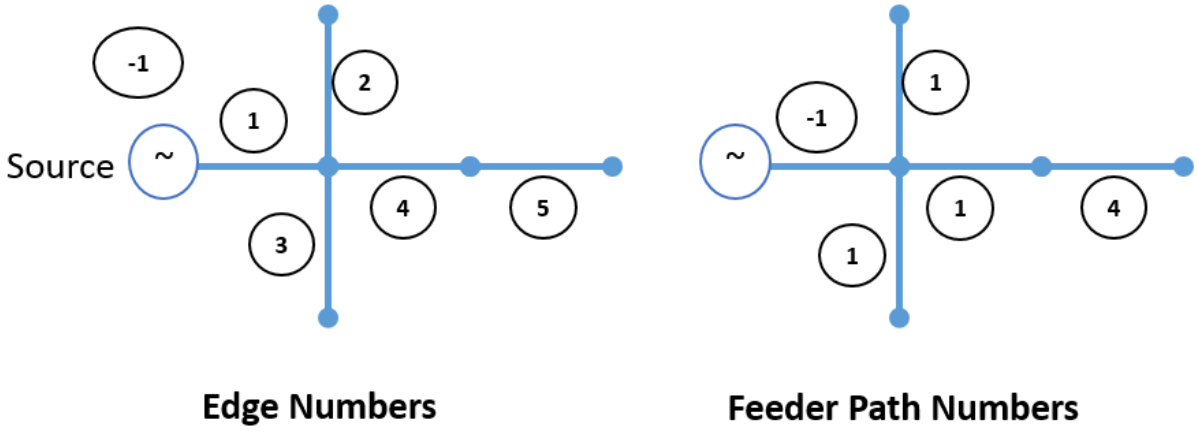

Fig. 3: Forward Trace based Edge and Feeder Path Numbering

In the graph of Fig. 3, if loads are added at the end of edges 2, 3 and 5, the edge numbers and feeder path indices will change as shown in Fig. 4 (assuming that the graph is traced such that loads are encountered in the order L_2, L_3 and L_5). Application of GTA to this network will iteratively calculate the voltage ("across" variable) and current ("through" variable) for each edge as discussed next.

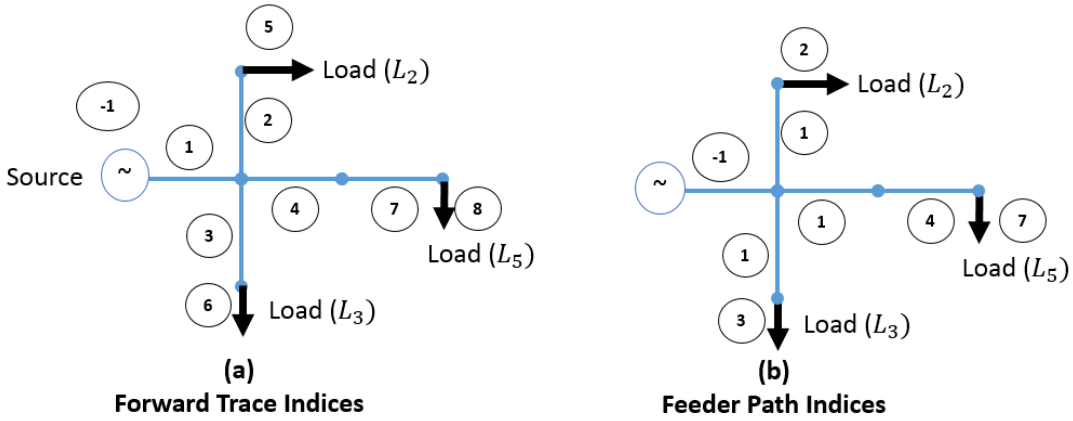

Fig. 4: Forward Trace based Edge and Feeder Path Numbering for Graph of Fig. 3 with Loads

The first iteration calculates the voltages at the end of each edge as shown in Table 5 by tracing the graph in the increasing order of the forward trace indices (if the forward trace index corresponds to a load, it is skipped). It is assumed that the edge currents are zero at the start of the iterations. Therefore, all the voltages are identical, as can be seen by substituting zero for edge

currents in Table 5. In the next step, with the voltages known at the end of each edge, the graph is traced in the descending order of the forward trace indices. If the forward trace index corresponds to a load, its current is calculated using the load model, which in Fig. 4 is assumed to be constant resistance. Therefore, load current is voltage of its feeder path divided by its resistance. Next, an "+=" operation is performed to accumulate the current flowing in an edge's feeder path and satisfy KCL as shown in Table 6. These two steps are repeated till the difference in voltages calculated between two iterations becomes less than a specified threshold.

Table 5: Calculating Voltages at the End of Edges by Tracing the Graph based on Forward Trace Indices (forward trace indices of loads are skipped)

Edge with Forward Trace Index	Voltage at the end of the edge
1	$\boldsymbol{V_1} = V_{-1} - Z_1 I_1$
2	$\boldsymbol{V_2} = \boldsymbol{V_1} - Z_2 I_2$
3	$\boldsymbol{V_3} = \boldsymbol{V_1} - Z_3 I_3$
4	$\boldsymbol{V_4} = \boldsymbol{V_1} - Z_4 I_4$
7	$\boldsymbol{V_7} = \boldsymbol{V_4} - Z_7 I_7$

Table 6: Calculating Edge Currents by Tracing the Graph in the Reverse Order of Forward Trace Indices

Edge with Forward Trace Index	Feeder Path Index	Current in the edge
8	7	$I_7 += I_8 = V_7 / R_{L_5}$
7	4	$I_4 += I_7$
6	3	$I_3 += I_6 = V_3 / R_{L_3}$
5	2	$I_2 += I_5 = V_2 / R_{L_2}$
4	1	$I_1 += I_4$
3	1	$I_1 += I_3$
2	1	$I_1 += I_2$
1	-1	$I_{-1} += I_1$

In general, the voltage at the end of each edge can be calculated using (1) while the current flowing through an edge can be calculated using (2).

$$V_k = V_{feedepath\_of\_k} - I_k Z_k \tag{1}$$

$$I_{feeder\_path\_k} = I_{feeder\_path\_k} + I_{edge\_with\_feeder\_path\_k} \tag{2}$$

If in the network of Fig. 4, $V_{-1} = 1V$, resistance of all the branches is 0.01Ω and load resistances are $R_{L_2} = 0.5\Omega$, $R_{L_3} = 0.2\Omega$ and $R_{L_5} = 1\Omega$, the GTA approach as discussed above and summarized in equations (1) and (2) results in voltages and currents calculated as shown in the last column of Tables 7 and 8, respectively. Interested reader can verify that these results are the same (to the 4th decimal place) as those calculated using mesh analysis that is taught in elementary circuit analysis courses. Reference [10] should be referred to for convergence properties of forward/backward sweep methods on general radial circuits.

Table 7: Voltages at the end of Edges for Network of Fig. 4

Voltage	Iterations									
	1	**2**	**3**	**4**	**5**	**6**	**7**	**8**	**9**	**10**
V_{-1}	1	1.0000	1.0000	1.0000	1.0000	1.0000	1.0000	1.0000	1.0000	1.0000
V_1	1	0.9200	0.9230	0.9286	0.9289	0.9285	0.9284	0.9285	0.9285	0.9285
V_2	1	0.9800	0.9004	0.9050	0.9105	0.9107	0.9103	0.9102	0.9103	0.9103
V_3	1	0.9500	0.8725	0.8794	0.8846	0.8847	0.8843	0.8842	0.8843	0.8843
V_4	1	0.9900	0.9101	0.9132	0.9196	0.9199	0.9194	0.9193	0.9194	0.9194
V_7	1	0.9900	0.9801	0.9003	0.9042	0.9105	0.9108	0.9103	0.9102	0.9103

Table 8: Edge Currents for Network of Fig. 4

Forward Trace Index	Iterations									
	1	**2**	**3**	**4**	**5**	**6**	**7**	**8**	**9**	**10**
1	8.0000	7.7000	7.1434	7.1072	7.1481	7.1555	7.1528	7.1519	7.1521	7.1522
2	2.0000	1.9600	1.8008	1.8100	1.8209	1.8214	1.8206	1.8205	1.8205	1.8206
3	5.0000	4.7500	4.3625	4.3969	4.4230	4.4235	4.4214	4.4212	4.4213	4.4213
4	1.0000	0.9900	0.9801	0.9003	0.9042	0.9105	0.9108	0.9103	0.9102	0.9103
7	1.0000	0.9900	0.9801	0.9003	0.9042	0.9105	0.9108	0.9103	0.9102	0.9103

It should be noted that while in the example above the circuit is assumed to be single phase, this is done to simplify the discussion. Three phase circuits with a combination of one phase, two phase and three phase components can be easily solved with GTA as has been demonstrated in a number of studies [41]-[43], [17].

Equations (1) and (2) above are sufficient to solve single source, radial networks, where the spanning tree of the network is the network itself. If a network has loops and/or multiple sources,

additional equations are needed to solve the network. The formulation of these equations is discussed in the next section.

2.3.2 Power Flow Analysis on Circuits with Loops using GTA

When loops are present in a circuit such as in Fig. 1(a), the spanning tree of the circuit is first re-numbered as discussed in the last section. The co-tree edges are then assigned edge indices starting from the index that is one larger than the last forward trace index assigned to the tree's edges. There is no particular order in which indices to the co-tree edges should be assigned. With this re-numbering scheme the forward trace and feeder path indices of Fig. 1(a) are shown in Fig. 5.

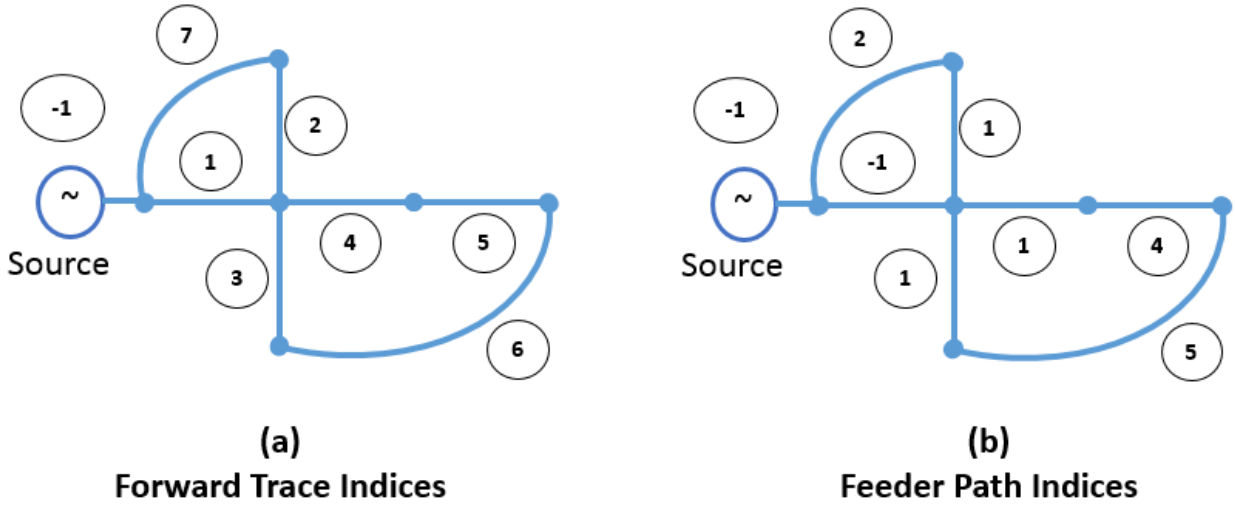

Fig. 5: Forward Trace and Feeder Path Indices for Fig. 1(a)

In Fig. 5, the feeder path indices for the two cotree edges could also have been -1 and 3 instead of 2 and 7, respectively because each cotree edge is connected between two edges. In GTA, one of the two possible feeder paths is called the *feeder path* side of the cotree while the other is called its *adjacent* side. The feeder path sides and adjacent sides play an important role in solving looped circuits in GTA as discussed below.

Using GTA looped circuits can be solved iteratively where each iteration is divided into two steps. In the first step, the looped circuit, such as that shown in Fig. 5, is converted into a radial circuit by disconnecting its adjacent side from the rest of the circuit. The radial circuit so formed includes the cotree edge as shown in Fig. 6. Application of forward and reverse traces using (1) and (2) to the radial circuit results in a voltage difference between the adjacent and feeder path sides of the cotree edge (see Fig. 6).

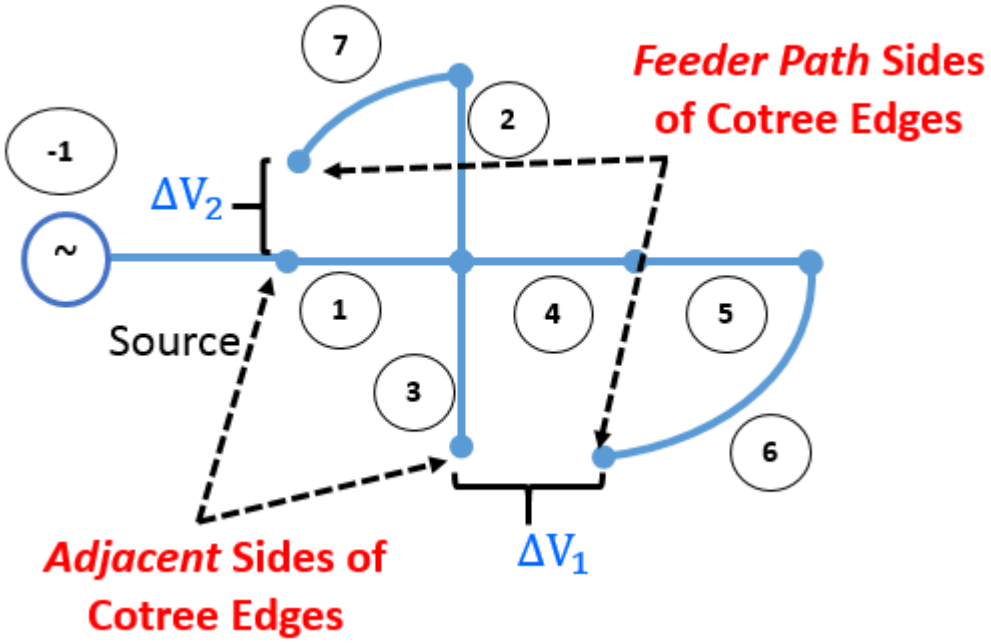

Fig. 6: Converting a Looped Circuit into a Radial Circuit

In a circuit with only one reference source there are as many voltage differences (called cotree voltages hereafter) as there are cotree edges. Since the cotree voltages are zero in the original circuit, these are made zero in the second step of the iteration. These two step iterations are repeated till a convergence criterion is met and the original circuit is solved.

The process of driving the cotree voltages to zero is based on the multi-port compensation technique, which was first introduced in [11] where an algorithm for solving weakly meshed distribution networks was discussed. The convergence performance of this algorithm, however, is

not satisfactory and is dependent on the location of cotree edges. Building upon the work of [11], [41] presented a GTA based power flow algorithm that was able to solve highly meshed distribution circuits within a few seconds and load stepping was presented as an approach for eliminating the dependence of convergence on the location of cotree edges. The basic concepts for solving looped circuits based on [11] and [41] are discussed below. To this end simple circuits that represent most of the commonly found circuit configurations in electric networks are used. Using GTA iterative equations are developed for solving these circuits. Iterations for all the circuits are plotted and compared with the exact solutions to demonstrate the accuracy and convergence characteristics of GTA based power flow analysis algorithms. Similar to the example shown in the last section for radial circuits, the simple circuits below are also assumed to be single phase to simplify the discussion. Three basic circuit configurations are used:

1. One reference source, one loop
2. One reference source, two loops
3. Two reference sources, two loops

Circuit with One Reference Source and One Loop

Fig. 7(a) shows the configuration of the one reference source, one loop circuit. The tree and cotree of the circuit along with the forward trace (encircled numbers in black) and feeder path indices (encircled numbers in red), which are assigned according to the discussion of the last section, are shown in Fig. 7(b) and Fig. 7(c), respectively. The modified radial circuit or tree for power flow analysis using GTA in the presence of loops, which is developed according to the procedure discussed earlier in this section, is shown in Fig. 7(d). Fig. 7(d) also shows that the location of cotree voltage (ΔV) that will appear as a result of disconnecting the cotree edge at the adjacent side. As discussed earlier in this section, each iteration of the power flow analysis algorithm applied to this circuit will involve two steps – apply (1) and (2) to the radial circuit of

Fig. 7(d) to obtain the cotree voltage ΔV; make the cotree voltage zero using the compensation technique.

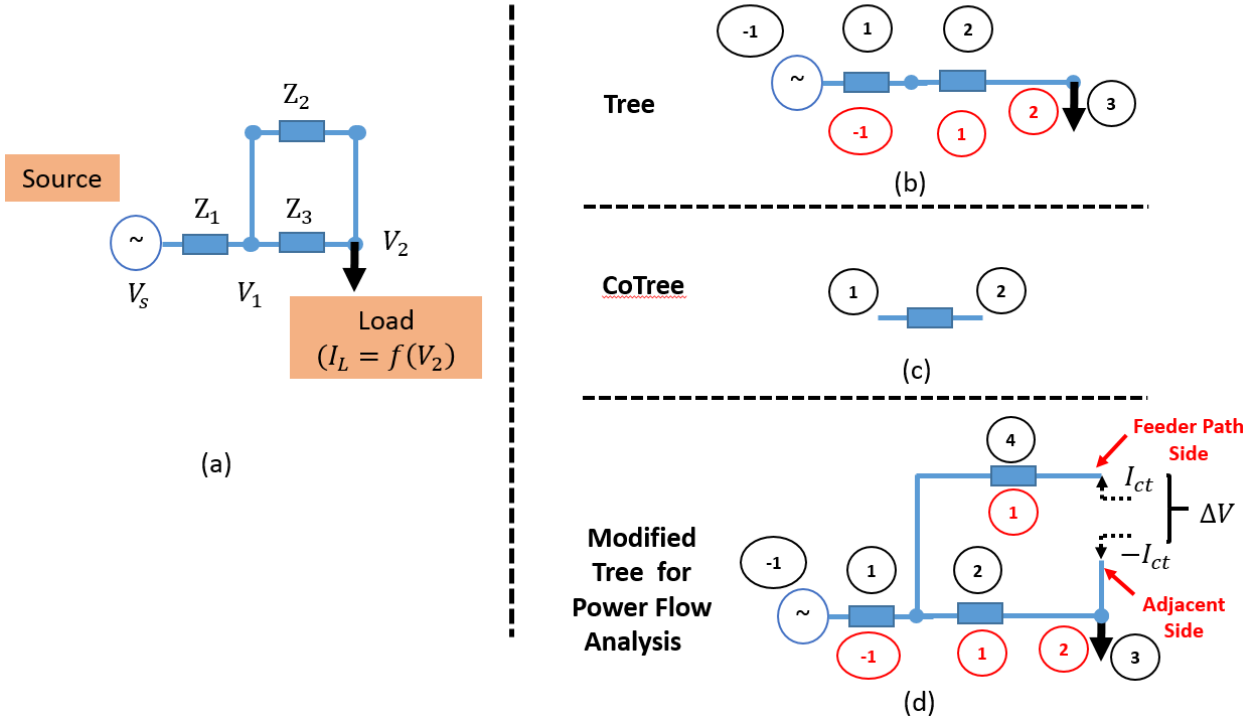

Fig. 7: Circuit with one Reference Source and One Loop

To understand how the cotree voltage is made zero in Fig. 7(d) using the compensation technique, let it be assumed that at the end of the 1^{st} iteration the application of (1) and (2) results in ΔV as the cotree voltage. If the load (or any other shunt element) is neglected, the Thevenin equivalent circuit as seen from the terminals across which the cotree voltage appears becomes as shown in Fig. 8(a).

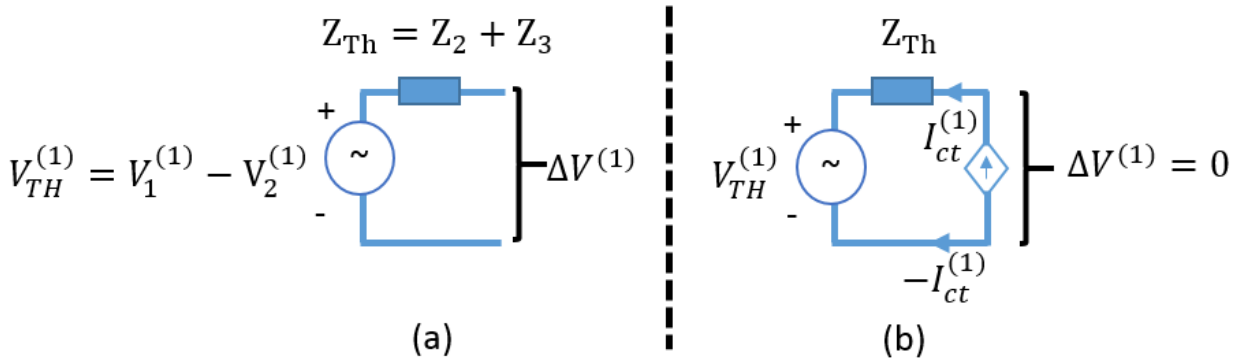

Fig. 8: Thevenin Equivalent of Fig. 7(d) as seen from the Location of Cotree Voltage in 1st Iteration

Therefore, according to the direction of the cotree current (I_{ct}^{1}) shown in Fig. 7(b), the cotree or loop current needed to make the cotree voltage zero in the first iteration is given by (3).

$$-V_{TH}^{(1)} - I_{ct}^{(1)} Z_{TH} = 0$$

$$\Rightarrow -V_{TH}^{(1)} - I_{ct}^{(1)} Z_{TH} = 0$$

$$\Rightarrow I_{ct}^{(1)} = -\frac{V_{TH}^{(1)}}{Z_{TH}} = -\frac{(V_1^{(1)} - V_2^{(1)})}{Z_{TH}} \quad (3)$$

Since the Thevenin equivalent circuit of Fig. 8(a) is made by neglecting the loads, it is not the exact Thevenin equivalent as seen from the terminals where the cotree voltage appears. As a result, the cotree voltage is not zero when the radial circuit solution is repeated with the cotree current of (3). Hence, iterations must be repeated till the cotree voltage becomes negligible to obtain the solution for the circuit of Fig. 7(a).

In the second iteration, application of (2) for calculating the currents in the radial circuit includes the cotree current calculated using (3) in the first iteration. If the solution of the radial circuit in the second iteration results in a cotree voltage of $\Delta V^{(2)}$, the new Thevenin equivalent circuit as seen from the terminals of the cotree becomes as shown in Fig. 9(a). Therefore, the additional cotree current needed that will make the cotree voltage zero is given by (4) and shown in Fig. 9(b) and the total cotree current at the end of the second iteration is given by (5).

$$\Delta I_{ct}^{(2)} = -\frac{V_{TH}^{(2)}}{Z_{TH}} = -\frac{V_1^{(2)} - V_2^{(2)} + I_{ct}^{(1)} Z_2}{Z_{TH}} \tag{4}$$

$$I_{ct}^{(2)} = I_{ct}^{(1)} + \Delta I_{ct}^{(2)} \tag{5}$$

Using (4) and (5), the change in cotree current and the total cotree current at the end of the k^{th} iteration is given by (6) and (7), respectively.

$$\Delta I_{ct}^{(k)} = -\frac{V_{TH}^{(k)}}{Z_{TH}} = -\frac{V_1^{(k)} - V_2^{(k)} + I_{ct}^{(k-1)} Z_2}{Z_{TH}} \tag{6}$$

$$I_{ct}^{(k)} = I_{ct}^{(k-1)} + \Delta I_{ct}^{(k)} \tag{7}$$

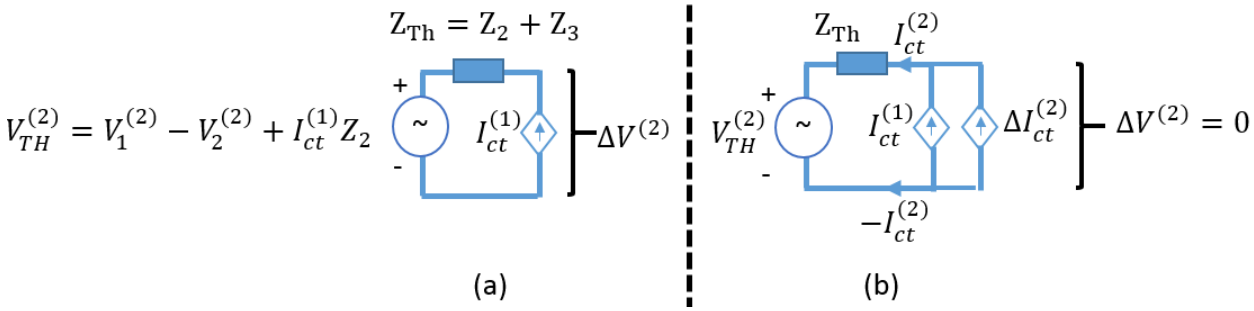

Fig. 9: Thevenin Equivalent of Fig. 7(d) as seen from the Location of Cotree Voltage in 2nd Iteration

Equations (6) and (7) also suggest that the process of updating the cotree currents to drive the cotree voltage to zero is a fixed tangent method [11] of finding the zero of the unknown equation that relates the cotree voltage and cotree current. This is illustrated in Fig. 10. Fig. 10(a) shows that the cotree current calculated using the Thevenin impedance (obtained after neglecting loads and other shunt elements) at the end of the first iteration will not result in zero cotree voltage in the second iteration. However, it will be much smaller than the cotree voltage in the first iteration and will gradually converge to zero in subsequent iterations. Fig. 10(b) shows that in the circuit of Fig. 7(a) if the load is assumed to be a constant impedance load and its impedance is significantly

larger than that of the line impedances, the actual Thevenin impedance will be close to that used in (3) for calculating the cotree currents. Therefore, the speed of convergence will increase.

Compared to local tangent methods such as Newton-Raphson, which may find the zero of equations faster, the fixed tangent method avoids the need for calculating the derivatives of the equations at every iteration thereby significantly simplifying the solution (The fixed tangent, which is the Thevenin equivalent impedance Z_{TH}, can be calculated once at the start of the power flow algorithm using traces as has been shown in [41]).

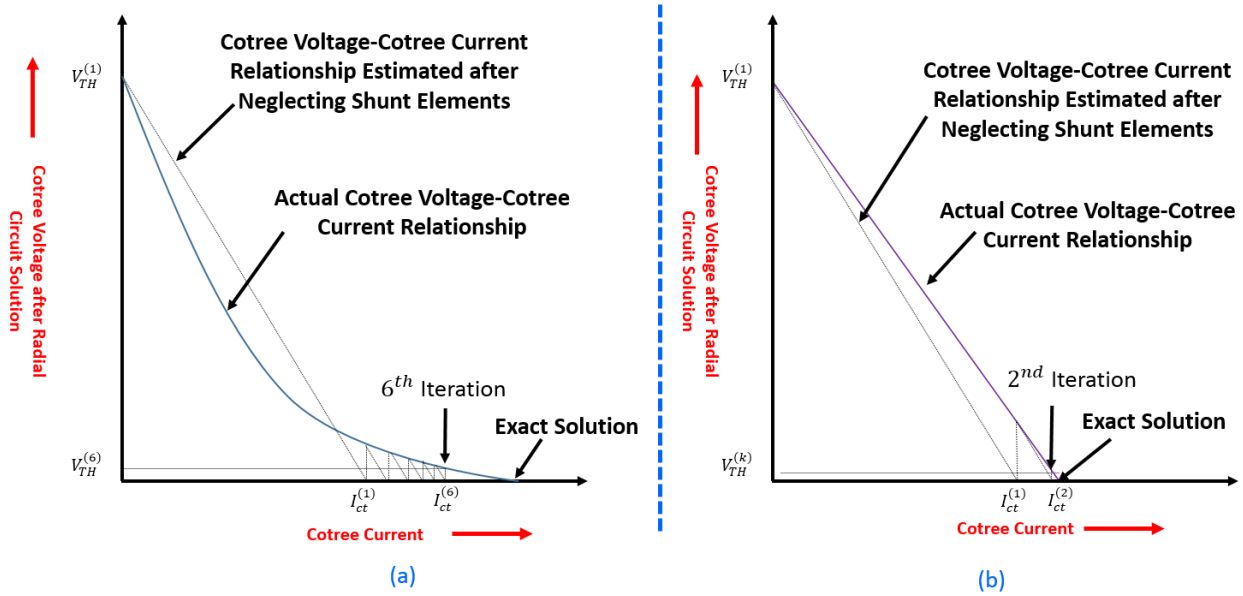

Fig. 10: Fixed Tangent Method of Finding Zero of the Cotree Voltage-Cotree Current Equation

For the circuit of Fig. 7(a), each forward and reverse trace iteration for the solution of the radial system shown in (1) and (2) when combined with iterations of (6) and (7) yield (8)-(10) that can be solved iteratively to obtain the solution of the circuit.

$$V_2^{(k)} = V_s - f\left(V_2^{(k-1)}\right)(Z_1 + Z_3) - I_{ct}^{(k-1)} Z_3 \tag{8}$$

$$V_1^{(k)} - V_2^{(k)} = Z_3 \left(I_{ct}^{(k-1)} + f\left(V_2^{(k)}\right)\right) \tag{9}$$

$$I_{ct}^{k} = -\frac{\left(\left(V_1^{(k)} - V_2^{(k)}\right) + Z_2 I_{ct}^{k-1}\right)}{Z_{TH}} + I_{ct}^{(k-1)} \tag{10}$$

Assuming values of $Z_1 = Z_2 = Z_3 = 0.2\Omega; V_s = \frac{13800}{\sqrt{3}}; f(V_2) = \frac{P}{V_2} = 42320000/V_2$, Fig. 11 shows plots of V_2 and I_{ct} for all the iterations till convergence is reached. The convergence criterion is $\left|V_2^{(k)} - V_2^{(k-1)}\right| < 0.0001$. Fortunately, the closed form solution for the circuit of Fig. 7(a) can be obtained by solving the quadratic equation (11).

$$V_2^2 - V_s V_2 + P(Z_1 + Z_2) = 0 \tag{11}$$

$$\Rightarrow V_2 = \frac{V_s \pm \sqrt{(V_s^2 - 4P\left(Z_1 + \frac{Z_3 Z_2}{Z_2 + Z_3}\right)}}{2} \tag{12}$$

For electric networks the feasible voltage value is obtained by using the + sign in (12) which is the same as that obtained by the iterative solution of (8)-(10) as shown in Fig. 11.

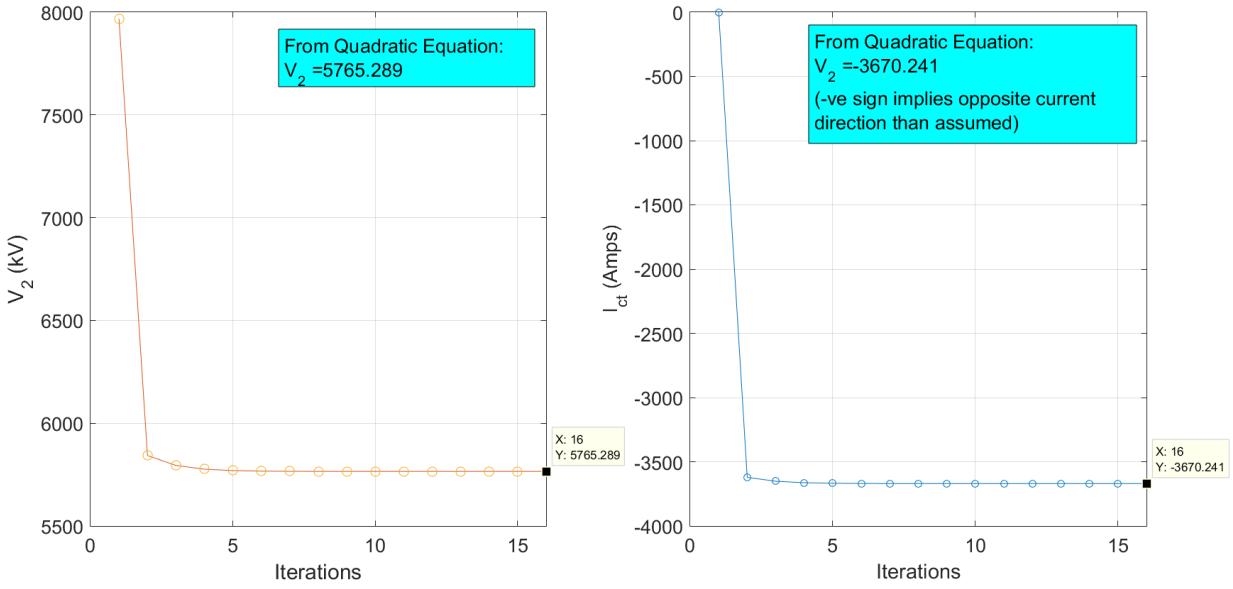

Fig. 11: Iterations for Solving the Circuit of Fig. 7(a)

Circuit with One reference source and two loops

This circuit has the same basic topology as the circuit of Fig. 7(a), but with an additional loop as shown in Fig. 12. Fig. 12 also shows the topology of the circuit and the modified tree for power flow analysis.

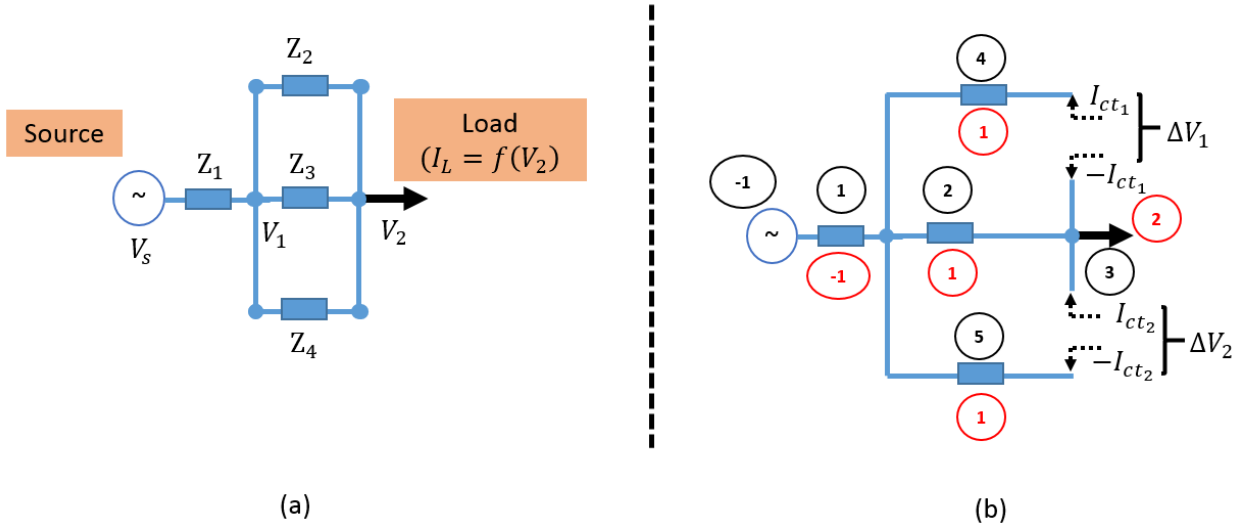

Fig. 12: Circuit with One Reference Source and Two Loops

Extending the concept of Thevenin equivalent impedance for single loops, the cotree currents for multi-loop circuits can be calculated using the multi-port Thevenin impedance matrices which are built assuming the loads or other shunt elements are absent. The procedure to automatically build these matrices using traces is discussed in [41]. Conceptually, the k^{th} row of the multi-port Thevenin equivalent impedance matrix (square matrix) for linear circuits with N loops is obtained by applying (13), which is equivalent to injecting a cotree current I_k with all other cotree currents being zero and measuring all the cotree voltages $V_{i,k}$.

$$Z_{TH}(i,k) = \frac{V_{i,k}}{I_{i,k}}; i = 1{:}N; I_k \neq 0 \; and \; I_j = 0, j \in [1,N]{\sim}k \tag{13}$$

For the circuit of Fig. 12(a), the 2-port Thevenin equivalent impedance matrix can be obtained by applying (13) in Fig. 12(b) which results in (14).

$$Z_{TH} = \begin{bmatrix} Z_2 + Z_3 & -Z_3 \\ -Z_3 & Z_4 + Z_3 \end{bmatrix} \tag{14}$$

The expressions for cotree voltages in the k^{th} iteration, $\Delta V_1^{(k)}$ and $\Delta V_2^{(k)}$, are as given in (15) and (16), respectively.

$$\Delta V_1^{(k)} = V_1^{(k)} + Z_2 I_{ct_1}^{(k-1)} - V_2^{(k)}$$

$$\Rightarrow \Delta V_1^{(k)} = Z_2 I_{ct_1}^{(k-1)} + Z_3 \left(I_{ct_1}^{(k-1)} + f\left(V_2^{(k-1)}\right) - I_{ct_2}^{(k-1)} \right) \tag{15}$$

Similarly,

$$\Delta V_2^{(k)} = V_2^{(k)} + Z_4 I_{ct_2}^{(k-1)} - V_1^{(k)}$$

$$\Rightarrow \Delta V_2^{(k)} = Z_4 I_{ct_2}^{(k-1)} - Z_3 \left(I_{ct_1}^{(k-1)} + f\left(V_2^{(k-1)}\right) - I_{ct_2}^{(k-1)} \right) \tag{16}$$

Using (14), (15) and (16), the change in cotree currents at the end of the k^{th} iteration can be calculated using (17) while the updated cotree currents at the end of the k^{th} iteration can be calculated using (18) (assuming Z_{TH} is invertible).

$$\begin{bmatrix} \Delta I_1^{(k)} \\ \Delta I_2^{(k)} \end{bmatrix} = -\begin{bmatrix} Z_2 + Z_3 & -Z_3 \\ -Z_3 & Z_4 + Z_3 \end{bmatrix}^{-1} \begin{bmatrix} \Delta V_1^{(k)} \\ \Delta V_2^{(k)} \end{bmatrix} \tag{17}$$

$$\begin{bmatrix} I_1^{(k)} \\ I_2^{(k)} \end{bmatrix} = \begin{bmatrix} I_1^{(k-1)} \\ I_2^{(k-1)} \end{bmatrix} + \begin{bmatrix} \Delta I_1^{(k)} \\ \Delta I_2^{(k)} \end{bmatrix} \tag{18}$$

Application of (1) and (2) to the radial circuit of Fig. 12(b) results in the expression of $V_2^{(k)}$ as given in (19). Equations (17)-(19) are solved iteratively to obtain the solution of the circuit of Fig. 12(a).

$$V_2^{(k)} = V_s - Z_1 f\left(V_2^{(k-1)}\right) - Z_3 \left(I_{ct_1}^{(k-1)} + f\left(V_2^{(k-1)}\right) - I_{ct_2}^{(k-1)} \right)$$

$$\Longrightarrow V_2^{(k)} = V_s - (Z_1 + Z_3) f\left(V_2^{(k-1)}\right) - Z_3 \left(I_{ct_1}^{(k-1)} - I_{ct_2}^{(k-1)} \right) \tag{19}$$

The iterations required to obtain the converged solution for the circuit of Fig. 12a using the same tolerance as in the previous example and $Z_2 = 0.2\Omega;\ Z_4 = 0.6\Omega$ is shown in Fig. 13. The actual solution for V_2 can still be obtained with (12) if $\frac{Z_3 Z_2}{Z_2+Z_3}$ is replaced with $\frac{1}{\frac{1}{z_2}+\frac{1}{z_3}+\frac{1}{z_4}} = \frac{Z_2 Z_3 Z_4}{Z_2 Z_3+Z_3 Z_4+Z_2 Z_4}$. The actual solution is also shown in Fig. 13.

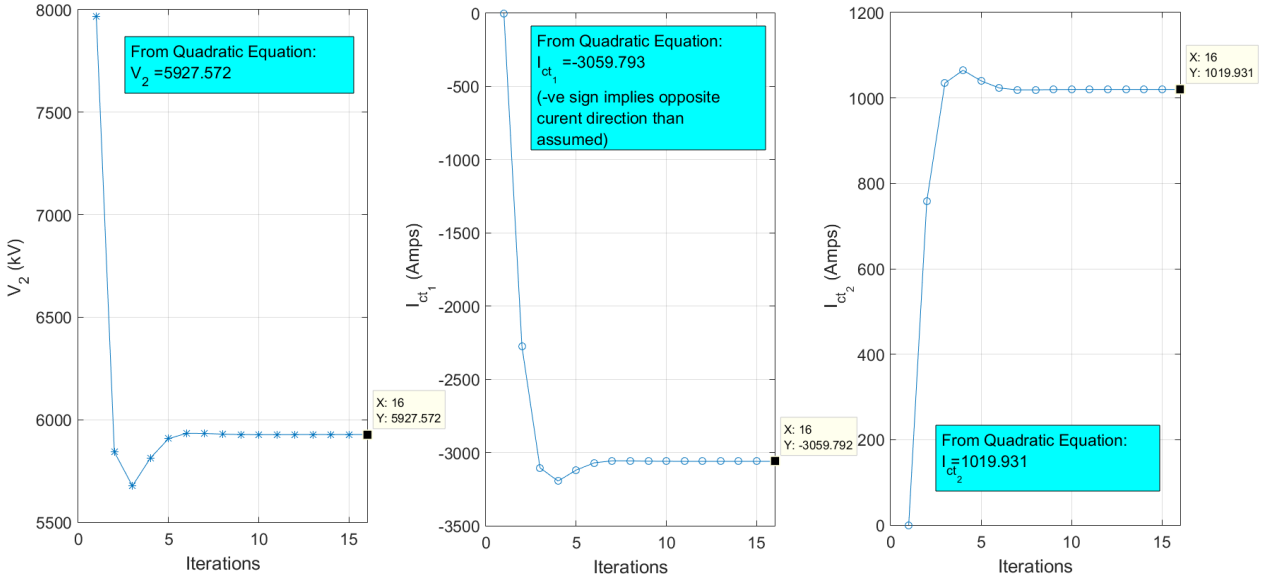

Fig. 13: Iterations for Solving the Circuit of Fig. 12(a)

Circuit with Two Reference Sources and Two Loops

When a circuit has multiple voltage sources, such as substations, the circuit is split into as many circuits with only one reference source in each circuit. As a result, when each circuit is solved using the methods described so far a voltage difference appears at the location of the split that can be reduced to zero using the same approach as has been described in the last two examples. Therefore, addition of multiple voltage sources increases the size of the Thevenin equivalent impedance matrix even though the number of loops remain the same.

Fig. 14(a) shows the circuit with two loops and two reference sources. This circuit is similar to the circuit of Fig. 12(a) except for an additional voltage source, V_{s_2}. Fig. 14(b) shows the locations

of the three cotree voltages. It also shows that traces restart at each reference source (indicated in Fig. 14(b) with two -1s assigned as forward trace indices to the two reference sources) and there can be only one reference source for each element of the circuit. When the tree for this circuit is obtained starting from reference source V_{s_1} using the procedure discussed in the last section, the feeder path and forward traces get assigned such that all the circuit elements are assumed to be supplied from this source. Hence, the cotree corresponding to the second reference source is assumed to be right where this source connects with the rest of the circuit. Therefore, the second reference source doesn't act as the feeder path for any of the circuit elements.

It is possible to move the location of the cotree associated with the second reference source. If that is done, radial solution will proceed separately for elements supplied by the two sources and convergence properties may be affected by the location of this cotree [11], [41]. However, for the conceptual discussion here the cotree associated with reference source 2 is not moved.

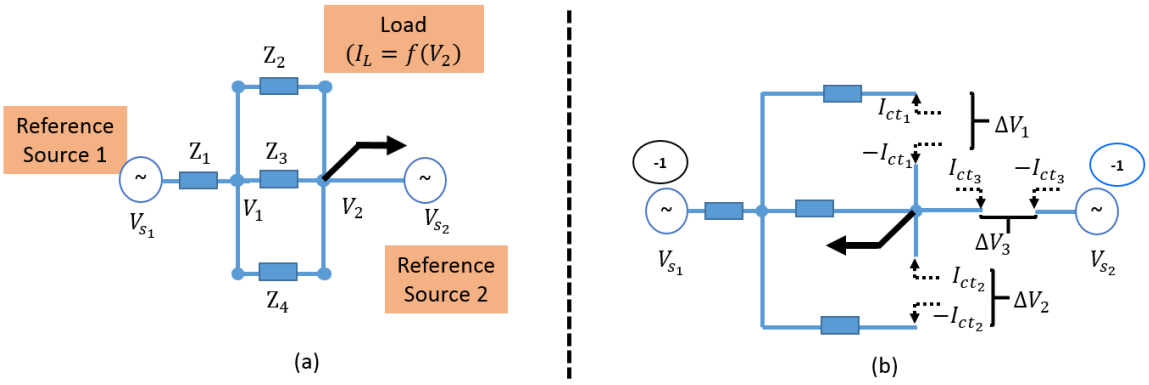

Fig. 14: Circuit with Two Reference Sources and Two Loops

Based on (13), the Thevenin equivalent impedance matrix will be a 3X3 matrix as shown in (20).

$$Z_{TH} = \begin{bmatrix} Z_2 + Z_3 & -Z_3 & -Z_3 \\ -Z_3 & Z_4 + Z_3 & Z_3 \\ -Z_3 & Z_3 & Z_1 + Z_3 \end{bmatrix} \tag{20}$$

The expressions for the three cotree voltages can be calculated as in the previous examples and are given in (21)-(23).

$$\begin{aligned}\Delta V_1^{(k)} &= Z_2 I_{ct_1}^{(k-1)} + Z_3\left(I_{ct_1}^{(k-1)} - I_{ct_3}^{(k-1)} + f\left(V_2^{(k-1)}\right) - I_{ct_2}^{(k-1)}\right)\\ &= (Z_2+Z_3)I_{ct_1}^{(k-1)} - Z_3 I_{ct_2}^{(k-1)} - Z_3 I_{ct_3}^{(k-1)} + Z_3 f\left(V_2^{(k-1)}\right)\end{aligned} \tag{21}$$

$$\begin{aligned}\Delta V_2^{(k)} &= Z_4 I_{ct_2}^{(k-1)} - Z_3\left(I_{ct_1}^{(k-1)} - I_{ct_3}^{(k-1)} + f\left(V_2^{(k-1)}\right) - I_{ct_2}^{(k-1)}\right)\\ &= (Z_4+Z_3)I_{ct_2}^{(k-1)} - Z_3 I_{ct_1}^{(k-1)} + Z_3 I_{ct_3}^{(k-1)} - Z_3 f\left(V_2^{(k-1)}\right)\end{aligned} \tag{22}$$

$$\begin{aligned}\Delta V_3^{(k)} &= V_{s_1} - Z_1\left(f\left(V_2^{(k-1)}\right) + I_{ct_3}^{(k-1)}\right) - Z_3\left(I_{ct_1}^{(k-1)} - I_{ct_3}^{(k-1)} + f\left(V_2^{(k-1)}\right) - I_{ct_2}^{(k-1)}\right) - V_{s_2}\\ &= V_{s_1} - (Z_1+Z_3)\left(f\left(V_2^{(k-1)}\right) - I_{ct_3}^{(k-1)}\right) - Z_3\left(I_{ct_1}^{(k-1)} - I_{ct_2}^{(k-1)}\right)\\ &\quad - V_{s_2}\end{aligned} \tag{23}$$

The expression for $V_2^{(k)}$ is given in (24).

$$\begin{aligned}V_2^{(k)} = V_{s_1} - (Z_1+Z_3)(f\left(V_2^{(k-1)}\right) - I_{ct_3}^{(k-1)}) - Z_3\left(I_{ct_1}^{(k-1)} -\\ I_{ct_2}^{(k-1)}\right)\end{aligned} \tag{24}$$

The iterative and actual solution for this circuit is shown in Fig. 15 where it is assumed that $V_{s_2} = 1.08V_{s_1}$ and the rest of the circuit parameters are assumed to be the same as in the last example.

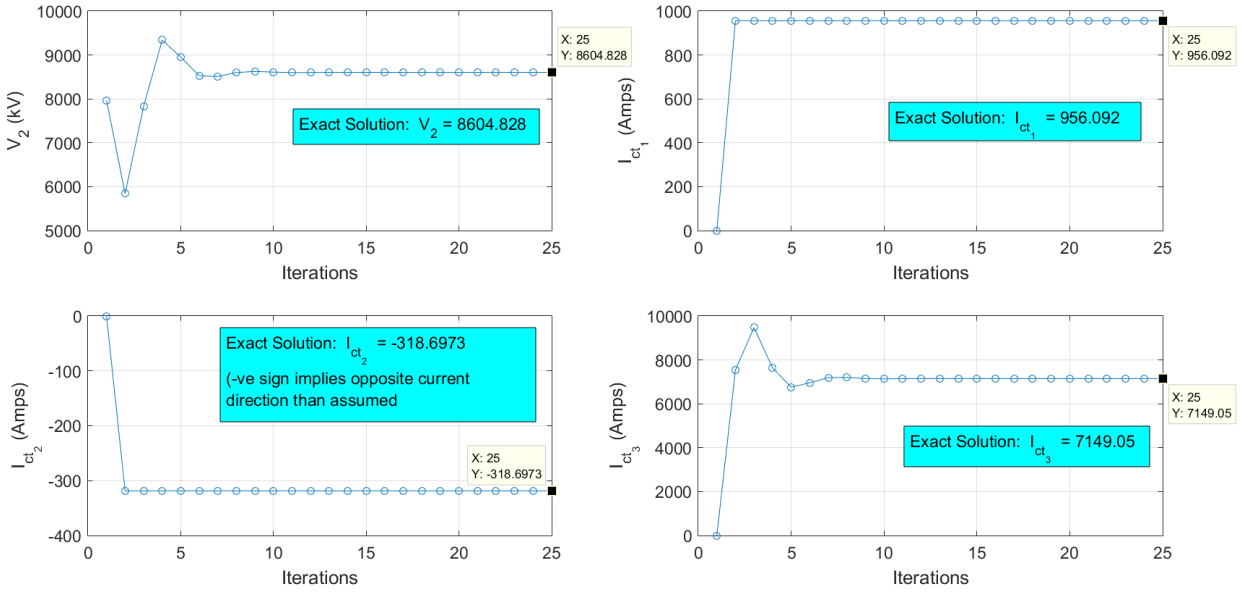

Fig. 15: Iterations for Solving the Circuit of Fig. 14(a)

2.4 Concluding Remarks

The discussion is this chapter was intended to discuss the basic concepts behind GTA and to show how iterations can be formed using GTA for solving radial and looped circuits with one or more voltage sources. Using simple examples, the steps that can be followed to split a network into a number of radial networks were discussed, and the application of forward and reverse traces to solve a radial circuit was also presented. The basic concepts of solving networks with loops in GTA by using Thevenin equivalent impedance matrix to drive the cotree voltages to zero was also discussed. The Thevenin equivalent impedance matrix can be formulated using traces as discussed in [41]. By means of simple examples it was shown that GTA based iterations can converge to the exact solution of the circuit in radial, looped and multi-source circuits.

With the concepts behind GTA explained here, the next chapter discusses a program that has been developed to study the dynamics of power systems using three phase, integrated T&D models. This program uses the GTA based power flow engine of the Distributed Engineering

Workstation (DEW®) software for solving the algebraic equations in the system of Differential Algebraic Equations (DAEs).

CHAPTER 3: DYNAMIC SIMULATION OF POWER SYSTEMS USING THREE PHASE NETWORK MODELS

3.1 Introduction

Power systems analyses can be broadly put into two categories – steady state and dynamics. Steady state analyses are intended to study the new equilibrium state that a power system attains after a disturbance, including a determination of whether the new equilibrium point is feasible. The transition period between two equilibrium states is neglected and power systems are modeled using non-linear algebraic equations in the frequency domain. The frequency domain analyses are typically performed using nominal frequency phasors. However, harmonics analysis can also be performed for power quality studies [50].

Studying the transition period between two equilibrium states is the domain of power systems dynamics studies. Depending on the frequencies of interest in the transition period, the dynamics studies are divided into two categories – electromagnetic transient studies and electromechanical transient studies. High frequency transients associated with events such as switching and lightning strikes are studied in electromagnetic transient studies (e.g., calculation of transient recovery voltage during breaker opening), whereas low frequency transients that bring into play the response of electromechanical equipment such as electrical machines and their controllers are studied in electromechanical transient studies.

Because of the significant difference in the time constants associated with electric networks and those associated with electromechanical equipment such as synchronous generators [51], electromechanical transient studies have become the norm for evaluating power systems stability. In these studies fast dynamics associated with electric networks and other equipment are neglected. As a result, power systems are modeled using Differential Algebraic Equations (DAEs) -

differential equations corresponding to the slow dynamics of interest, and algebraic equations corresponding to the fast dynamics, which are assumed to transition from one steady state to another [48], [7] at the nominal frequency. Since the program discussed in this dissertation is also intended to study electromechanical transients, and slow transients associated with solar irradiation transients, power systems are modeled using DAEs. However, unlike the existing electromechanical transient programs, this program models the electric networks in three phases (at nominal frequency), which gives it the ability to model unbalanced and integrated T&D networks. The program is called the Three Phase Dynamics Analyzer (TPDA) [17]. From hereafter, dynamic simulation will refer to the simulation of electromechanical transients in power systems.

The rest of the chapter discusses the key features of the program that give it the ability to simulate the dynamics of power systems using three phase network models. Validation results for the program will be discussed in the next chapter.

3.2 Challenge of DAEs based Modeling of Power Systems using Three Phase Network Models

Traditionally, the DAEs used to model the power systems are developed on the assumption of balanced electric networks [7], [48]. Moreover, the differential equations for equipment that interface with the network, which are typically rotating electric machines, are expressed in the rotating reference frame (fixed to a machine's rotor), which eliminates time varying inductances from their models. These rotating frames are represented using d, q and 0 axes which are related to the abc frame through Park's transformation. The discussion in this section will assume that a two pole synchronous generator is the machine that interfaces with the network.

If the network is balanced, the three Park's transformation equations reduce to a single phasor equation that relates the $dq0$ frame quantities to the abc frame phasor magnitudes and angles. Equations (25) and (26) show the Park's transformation and its simplified version that is obtained under balanced network conditions, respectively [48].

$$\mathbf{x}_{dq0}(t) = \mathbf{T}(t)\mathbf{x}_{abc}(t) \tag{25}$$

$$(x_d + jx_q)e^{j\left(\delta - \frac{\pi}{2}\right)} = |X|e^{j(\theta)} \tag{26}$$

Where,

$$\mathbf{T}(t) = \left(\frac{2}{3}\right)\begin{bmatrix} \sin(\delta + \omega_s t) & \sin(\delta + \omega_s t - 2\pi/3) & \sin(\delta + \omega_s t + 2\pi/3) \\ \cos(\delta + \omega_s t) & \cos(\delta + \omega_s t - 2\pi/3) & \cos(\delta + \omega_s t + 2\pi/3) \\ \frac{1}{2} & \frac{1}{2} & \frac{1}{2} \end{bmatrix}$$

$\mathbf{T}(t)$=Park's transformation matrix

$\mathbf{x}_{abc}(t)$ =3X1 vector of three phase abc frame quantity

$\mathbf{x}_{dq0}(t)$ =3X1 vector of three phase $dq0$ frame quantity

δ=angle that the direct axis of generator's rotor makes with the direct axis of a synchronously rotating reference frame

ω_s=Synchronous speed in radians/second

$|X|$=balanced abc frame phasor magnitude

θ= balanced abc frame phasor, phase A angle

Equation (26) shows that assuming a balanced network significantly simplifies the solution of DAEs for simulating power systems dynamics. This is because during each integration step the L.H.S of (26) can be used to obtain the d and q axis quantities, and once the updated d and q axis

quantities are available, these can be substituted in (26) to obtain the updated abc frame phasors, i.e., the R.H.S of (26).

However, if the network is unbalanced its algebraic equations must be modeled in three phase, which, as can be seen from (25), results in three $dq0$ frame quantities at the start of each integration step that can be used to solve the generator differential equations and calculate the updated $dq0$ frame quantities. However, three equations are not sufficient for calculating the three abc frame phasors from the updated $dq0$ frame quantities since a magnitude and phase angle needs to be calculated for each phasor resulting in a total of six quantities that must be calculated at each integration step. This problem is shown in (27), which is an expansion of (26) when the network is modeled in three phase using nominal frequency phasors.

$$\begin{bmatrix} x_d \\ x_q \\ x_0 \end{bmatrix} = \mathbf{T}(t) \begin{bmatrix} \sqrt{2}|x_a| \cos(\omega_s t + \theta_a) \\ \sqrt{2}|x_b| \cos(\omega_s t + \theta_b) \\ \sqrt{2}|x_c| \cos(\omega_s t + \theta_c) \end{bmatrix} \tag{27}$$

where, $|x_i|, \theta_i$ is the phasor magnitude and angle of phase i

Equation (27) shows that when going from the $dq0$ frame to the abc frame during an integration step there are not enough equations to obtain unique abc frame phasors. In the next section, a method is discussed that overcomes this challenge and enables the calculation of unique abc frame phasors at each integration step, even when the network is unbalanced.

3.3 Impact of Network Unbalance on $dq0$ Frame Quantities

Equation (28) is the famous Fortescue transformation that is used to decompose unbalanced abc frame phasors into a set of three symmetrical phasors - positive sequence (X_+), negative sequence (X_-) and zero sequence (X_0). Fig. 16 shows the graphical interpretation of the Fortescue transformation.

$$\begin{bmatrix} X_0 \\ X_+ \\ X_- \end{bmatrix} = \left(\frac{1}{3}\right)\begin{bmatrix} 1 & 1 & 1 \\ 1 & \alpha & \alpha^2 \\ 1 & \alpha^2 & \alpha \end{bmatrix}\begin{bmatrix} X_a \\ X_b \\ X_c \end{bmatrix} \tag{28}$$

Where, $[X_a\ X_b\ X_c]^T = \begin{bmatrix} x_a e^{j\theta_a} & x_b e^{j\theta_b} & x_c e^{j\theta_c} \end{bmatrix}^T$; $\alpha = e^{\frac{j2\pi}{3}}$; $\mathbf{A} = \begin{bmatrix} 1 & 1 & 1 \\ 1 & \alpha^2 & \alpha \\ 1 & \alpha & \alpha^2 \end{bmatrix}$

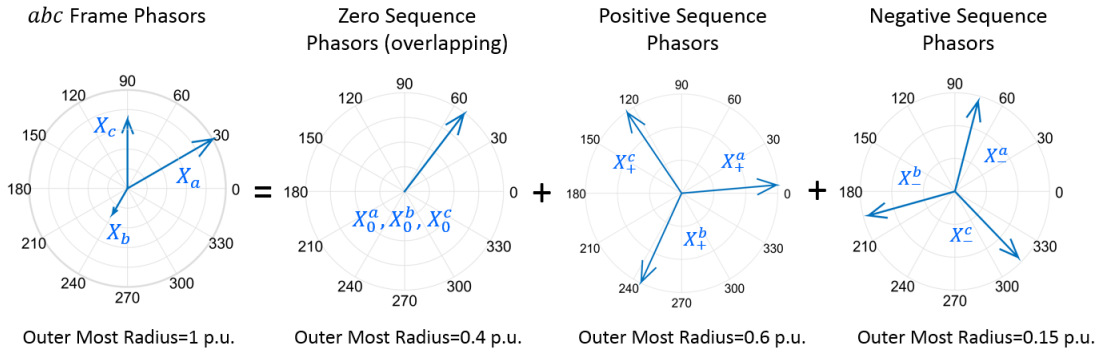

Fig. 16: Three phase *abc* Frame Phasors as Sum of Positive, Negative and Zero Sequence Phasors

Taking the inverse of the Fortescue transformation matrix in (28), the *abc* frame phasors can be written as (29).

$$\begin{bmatrix} X_a \\ X_b \\ X_c \end{bmatrix} = 3\begin{bmatrix} 1 & 1 & 1 \\ 1 & \alpha & \alpha^2 \\ 1 & \alpha^2 & \alpha \end{bmatrix}^{-1}\begin{bmatrix} X_0 \\ X_+ \\ X_- \end{bmatrix}$$

$$\Rightarrow \begin{bmatrix} X_a \\ X_b \\ X_c \end{bmatrix} = \begin{bmatrix} 1 & 1 & 1 \\ 1 & \alpha^2 & \alpha \\ 1 & \alpha & \alpha^2 \end{bmatrix}\begin{bmatrix} X_0 \\ X_+ \\ X_- \end{bmatrix} \tag{29}$$

Equation (29) can also be written as (30), which is the same decomposition as shown in Fig. 1.

$$\begin{bmatrix} X_a \\ X_b \\ X_c \end{bmatrix} = \begin{bmatrix} 1 & 0 & 0 \\ 1 & 0 & 0 \\ 1 & 0 & 0 \end{bmatrix}\begin{bmatrix} X_0 \\ 0 \\ 0 \end{bmatrix} + \begin{bmatrix} 0 & 1 & 0 \\ 0 & \alpha^2 & 0 \\ 0 & \alpha & 0 \end{bmatrix}\begin{bmatrix} 0 \\ X_+ \\ 0 \end{bmatrix} + \begin{bmatrix} 0 & 0 & 1 \\ 0 & 0 & \alpha \\ 0 & 0 & \alpha^2 \end{bmatrix}\begin{bmatrix} 0 \\ 0 \\ X_- \end{bmatrix} \tag{30}$$

Including the implicit nominal frequency rotation of phasors into (30) yields (31).

$$\begin{bmatrix} X_a \\ X_b \\ X_c \end{bmatrix} e^{j\omega_s t} = \begin{bmatrix} 1 & 0 & 0 \\ 1 & 0 & 0 \\ 1 & 0 & 0 \end{bmatrix} \begin{bmatrix} X_0 \\ 0 \\ 0 \end{bmatrix} e^{j\omega_s t} + \begin{bmatrix} 0 & 1 & 0 \\ 0 & \alpha^2 & 0 \\ 0 & \alpha & 0 \end{bmatrix} \begin{bmatrix} 0 \\ X_+ \\ 0 \end{bmatrix} e^{j\omega_s t} + \begin{bmatrix} 0 & 0 & 1 \\ 0 & 0 & \alpha \\ 0 & 0 & \alpha^2 \end{bmatrix} \begin{bmatrix} 0 \\ 0 \\ X_- \end{bmatrix} e^{j\omega_s t} \tag{31}$$

Using (31), the instantaneous values of the abc frame quantities can be written as (32).

$$\sqrt{2}Re\left(\begin{bmatrix} X_a \\ X_b \\ X_c \end{bmatrix} e^{j\omega_s t}\right)$$

$$= \sqrt{2}\left(Re\left(\begin{bmatrix} 1 & 0 & 0 \\ 1 & 0 & 0 \\ 1 & 0 & 0 \end{bmatrix} \begin{bmatrix} X_0 \\ 0 \\ 0 \end{bmatrix} e^{j\omega_s t} + \begin{bmatrix} 0 & 1 & 0 \\ 0 & \alpha^2 & 0 \\ 0 & \alpha & 0 \end{bmatrix} \begin{bmatrix} 0 \\ X_+ \\ 0 \end{bmatrix} e^{j\omega_s t} + \begin{bmatrix} 0 & 0 & 1 \\ 0 & 0 & \alpha \\ 0 & 0 & \alpha^2 \end{bmatrix} \begin{bmatrix} 0 \\ 0 \\ X_- \end{bmatrix} e^{j\omega_s t}\right)\right)$$

$$= \sqrt{2}Re\left(\begin{bmatrix} 1 & 0 & 0 \\ 1 & 0 & 0 \\ 1 & 0 & 0 \end{bmatrix} \begin{bmatrix} |X_0|e^{j\theta_0} \\ 0 \\ 0 \end{bmatrix} e^{j\omega_s t} + \begin{bmatrix} 0 & 1 & 0 \\ 0 & \alpha^2 & 0 \\ 0 & \alpha & 0 \end{bmatrix} \begin{bmatrix} 0 \\ |X_+|e^{j\theta_+} \\ 0 \end{bmatrix} e^{j\omega_s t} + \begin{bmatrix} 0 & 0 & 1 \\ 0 & 0 & \alpha \\ 0 & 0 & \alpha^2 \end{bmatrix} \begin{bmatrix} 0 \\ 0 \\ |X_-|e^{j\theta_-} \end{bmatrix} e^{j\omega_s t}\right)$$

$$= \sqrt{2}Re\left(\begin{bmatrix} 1 & 0 & 0 \\ 1 & 0 & 0 \\ 1 & 0 & 0 \end{bmatrix} \begin{bmatrix} |X_0|e^{j(\theta_0+\omega_s t)} \\ 0 \\ 0 \end{bmatrix} + \begin{bmatrix} 0 & 1 & 0 \\ 0 & \alpha^2 & 0 \\ 0 & \alpha & 0 \end{bmatrix} \begin{bmatrix} 0 \\ |X_+|e^{j(\theta_+ +\omega_s t)} \\ 0 \end{bmatrix} + \begin{bmatrix} 0 & 0 & 1 \\ 0 & 0 & \alpha \\ 0 & 0 & \alpha^2 \end{bmatrix} \begin{bmatrix} 0 \\ 0 \\ |X_-|e^{j(\theta_- +\omega_s t)} \end{bmatrix}\right)$$

$$= \sqrt{2}Re\left(\begin{bmatrix} e^{j(\theta_0+\omega_s t)} & 0 & 0 \\ e^{j(\theta_0+\omega_s t)} & 0 & 0 \\ e^{j(\theta_0+\omega_s t)} & 0 & 0 \end{bmatrix}\begin{bmatrix} |X_0| \\ 0 \\ 0 \end{bmatrix} + \begin{bmatrix} 0 & e^{j(\theta_+ +\omega_s t)} & 0 \\ 0 & e^{j(\theta_+ +\omega_s t-\frac{2\pi}{3})} & 0 \\ 0 & e^{j(\theta_+ +\omega_s t+\frac{2\pi}{3})} & 0 \end{bmatrix}\begin{bmatrix} 0 \\ |X_+| \\ 0 \end{bmatrix} + \right.$$

$$\left. \begin{bmatrix} 0 & 0 & e^{j(\theta_- +\omega_s t)} \\ 0 & 0 & e^{j(\theta_- +\omega_s t+\frac{2\pi}{3})} \\ 0 & 0 & e^{j(\theta_- +\omega_s t-\frac{2\pi}{3})} \end{bmatrix}\begin{bmatrix} 0 \\ 0 \\ |X_-| \end{bmatrix}\right)$$

$$= \sqrt{2}\left(\begin{bmatrix} \cos(\theta_0+\omega_s t) & 0 & 0 \\ \cos(\theta_0+\omega_s t) & 0 & 0 \\ \cos(\theta_0+\omega_s t) & 0 & 0 \end{bmatrix}\begin{bmatrix} |X_0| \\ 0 \\ 0 \end{bmatrix} + \begin{bmatrix} 0 & \cos(\theta_+ +\omega_s t) & 0 \\ 0 & \cos\left(\theta_+ +\omega_s t-\frac{2\pi}{3}\right) & 0 \\ 0 & cos\left(\theta_+ +\omega_s t+\frac{2\pi}{3}\right) & 0 \end{bmatrix}\begin{bmatrix} 0 \\ |X_+| \\ 0 \end{bmatrix} + \right.$$

$$\left. \begin{bmatrix} 0 & 0 & \cos(\theta_- +\omega_s t) \\ 0 & 0 & \cos\left(\theta_- +\omega_s t+\frac{2\pi}{3}\right) \\ 0 & 0 & cos\left(\theta_- +\omega_s t-\frac{2\pi}{3}\right) \end{bmatrix}\begin{bmatrix} 0 \\ 0 \\ |X_-| \end{bmatrix}\right) \quad (32)$$

Equation (32) shows that any abc frame quantity at the interface between network and synchronous generator (which is modeled using differential equations) can be decomposed into decoupled positive, negative and zero sequence components. Therefore, application of the Park's transformation as shown in (25), will result in the expression of (33) for the $dq0$ frame quantities.

$$\begin{bmatrix} x_d \\ x_q \\ x_0 \end{bmatrix} = \sqrt{2}\mathbf{T}\begin{bmatrix} \cos(\theta_0+\omega_s t) & 0 & 0 \\ \cos(\theta_0+\omega_s t) & 0 & 0 \\ \cos(\theta_0+\omega_s t) & 0 & 0 \end{bmatrix}\begin{bmatrix} |X_0| \\ 0 \\ 0 \end{bmatrix}$$

$$+\sqrt{2}\mathbf{T}\begin{bmatrix} 0 & \cos(\theta_+ +\omega_s t) & 0 \\ 0 & \cos\left(\theta_+ +\omega_s t-\frac{2\pi}{3}\right) & 0 \\ 0 & cos\left(\theta_+ +\omega_s t+\frac{2\pi}{3}\right) & 0 \end{bmatrix}\begin{bmatrix} 0 \\ |X_+| \\ 0 \end{bmatrix}$$

$$+\sqrt{2}\mathbf{T}\begin{bmatrix} 0 & 0 & \cos(\theta_- +\omega_s t) \\ 0 & 0 & \cos\left(\theta_- +\omega_s t+\frac{2\pi}{3}\right) \\ 0 & 0 & cos\left(\theta_- +\omega_s t-\frac{2\pi}{3}\right) \end{bmatrix}\begin{bmatrix} 0 \\ 0 \\ |X_-| \end{bmatrix}$$

$$\Rightarrow \begin{bmatrix} x_d \\ x_q \\ x_0 \end{bmatrix} = \sqrt{2} \begin{bmatrix} 0 \\ 0 \\ |X_0|\cos(\theta_0 + \omega_s t) \end{bmatrix} + \sqrt{2} \begin{bmatrix} |X_+|\sin(\delta - \theta_+) \\ |X_+|\cos(\delta - \theta_+) \\ 0 \end{bmatrix} + \sqrt{2} \begin{bmatrix} |X_-|\sin(\delta + \theta_- + 2\omega_s t) \\ |X_-|\cos(\delta + \theta_- + 2\omega_s t) \\ 0 \end{bmatrix} \tag{33}$$

Equation (33) shows that in the $dq0$ frame, the d and q axes see contributions from both positive and negative sequence components of abc frame quantities, while the zero axis is identical in the abc and $dq0$ frames and is only impacted by the zero sequence component. Equation (33) also implies that if torsional vibrations are neglected at steady state, i.e., δ is assumed to be constant [52], nominal frequency negative sequence quantities in the abc frame show up as second harmonic components in the $dq0$ frame. The physical reason for the appearance of second harmonic components associated with negative sequence quantities of the abc frame is their opposite direction of rotation w.r.t the rotor of the synchronous generator, which rotates in the same direction as the positive sequence quantities.

3.4 Synchronous Generator Model and its Interface under Network Unbalance

The DAE model of synchronous generators that is typically used in power systems dynamics studies is given in (34)-(42) [48].

Rotor Differential Equations

Electrical Equations

$Field\ winding$:
$$T'_{d0}\frac{dE'_q}{dt} = -E'_q - A\left[I_d - B\left(\psi_{1d} + CI_d - E'_q\right)\right] + E_{fd} + S_{fd} \tag{34}$$

$d-axis\ damper\ winding$:
$$T''_{d0}\frac{d\psi_{1d}}{dt} = -\psi_{1d} + E'_q - CI_d \tag{35}$$

$1^{st}\ q$ $-\ axis\ damper\ winding$:

$$T'_{q0}\frac{dE'_d}{dt} = -E'_d + A_1\left[I_q - B_1\left(\psi_{2q} + C_1 I_q + E'_d\right)\right] + S_{1q} \tag{36}$$

$2^{nd}\ q$ $-\ axis\ damper\ winding$:

$$T''_{q0}\frac{d\psi_{2q}}{dt} = -\psi_{2q} - E'_d - C_1 I_q \tag{37}$$

Mechanical Equations

Stator Algebraic Equations

$$v_d = -\psi_q - R_s I_d \tag{40}$$

$$v_q = \psi_d - R_s I_q \tag{41}$$

$$v_0 = -Z_0 I_0 \tag{42}$$

Where, $T_e = \left(\psi_d I_q - \psi_q I_d\right)$

$\psi_d = -X''_d I_d + DE'_q + E\psi_{1d}$ and $\psi_q = -X''_q I_q - D_1 E'_d + E_1\psi_{2q}$

$\psi''_d = DE'_q + E\psi_{1d}$; $\psi''_q = -D_1 E'_d + E_1\psi_{2q}$; $|\psi''| = \sqrt{\psi''^2_d + \psi''^2_q}$

$$\frac{d\delta}{dt} = \omega - \omega_s \tag{38}$$

$$\frac{2H}{\omega_s}\frac{d\omega}{dt} = T_M - T_e \tag{39}$$

$S_{fd} = \frac{\psi''_d}{|\psi''|}S_G(|\psi''|)$; $S_{1q} = \frac{\psi''_q(X_q - X_{ls})}{|\psi''|(X_d - X_{ls})}S_G(|\psi''|)$

Symbols used in (34)-(42) are explained in Table 9. Reference [48] can be referred to for additional details about these equations.

Table 9: Meanings of Symbols used in (34)-(42)

ψ_d, ψ_q, ψ_0	$d, q, 0$ axis fluxes	A	$X_d - X'_d$
v_d, v_q, v_0	$d, q, 0$ axis voltages at stator terminals	B	$\frac{(X'_d - X''_d)}{(X'_d - X_{ls})^2}$
I_d, I_q, I_0	$d, q, 0$ axis stator currents	C	$(X'_d - X_{ls})$
E'_q, ψ_{1d}	State Variables associated with d-axis field winding and damper winding, respectively	A_1	$X_q - X'_q$
E'_d, ψ_{2q}	State Variables associated with q-axis slow and fast time constant damper windings, respectively	B_1	$\frac{(X'_q - X''_q)}{(X'_q - X_{ls})^2}$
R_s	Stator resistance	C_1	$(X'_q - X_{ls})$
X_d, X'_d, X''_d	d axis self, transient and sub-transient reactance, respectively	D	$\frac{(X''_d - X_{ls})}{(X'_d - X_{ls})}$
X_q, X'_q, X''_q	q axis self, transient and sub-transient reactance, respectively	E	$\frac{(X'_d - X''_d)}{(X'_d - X_{ls})}$
T'_{d0}, T''_{d0}	Time constant (seconds) associated with d-axis field winding and damper winding, respectively	D_1	$\frac{(X''_q - X_{ls})}{(X'_q - X_{ls})}$
T'_{q0}, T''_{q0}	Time constant (seconds) associated with q-axis slow and fast time constant damper windings, respectively	E_1	$\frac{(X'_q - X''_q)}{(X'_q - X_{ls})}$
H	Inertia Constant (seconds)	ω	Rotor angular speed (radians/second)
Z_0	Zero sequence impedance which is part of input data [52]	ω_s	Synchronous rotor speed (radians/second)
T_M	Mechanical Torque		

The differential equations (34)-(42) can also be written as shown in (43), which shows that generator differential equations are nonlinear. The causes of nonlinearity are the expressions for electromagnetic torque and the generator saturation as shown above. Therefore, although the positive, negative and zero sequence components in the dq0 frame quantities at the interface are decoupled, they get coupled in the generator due to its nonlinearities and the response of the generator to the $dq0$ frame currents cannot be written as the superposition of the responses to their positive, negative and zero sequence components.

$$\begin{bmatrix} \dot{E}'_q \\ \dot{\psi}_{1d} \\ \dot{E}'_d \\ \dot{\psi}_{2q} \\ \dot{\delta} \\ \dot{\omega} \end{bmatrix} = \begin{bmatrix} -\frac{1+AB}{T'_{d0}} & \frac{AB}{T'_{d0}} & 0 & 0 & 0 & 0 \\ \frac{1}{T''_{d0}} & -\frac{1}{T''_{d0}} & 0 & 0 & 0 & 0 \\ 0 & 0 & -\frac{1+A_1B_1}{T'_{q0}} & -\frac{A_1B_1}{T'_{q0}} & 0 & 0 \\ 0 & 0 & -\frac{1}{T''_{q0}} & -\frac{1}{T''_{q0}} & 0 & 0 \\ 0 & 0 & 0 & 0 & 0 & 1 \\ 0 & 0 & 0 & 0 & 0 & 0 \end{bmatrix} \begin{bmatrix} E'_q \\ \psi_{1d} \\ E'_d \\ \psi_{2q} \\ \delta \\ \omega \end{bmatrix}$$

$$+ \begin{bmatrix} \frac{-A+ABC}{T'_{d0}} & 0 & 0 & \frac{1}{T'_{do}} & 0 \\ -\frac{C}{T''_{d0}} & 0 & 0 & 0 & 0 \\ 0 & \frac{A_1 - A_1B_1C_1}{T'_{q0}} & 0 & 0 & 0 \\ 0 & -\frac{C_1}{T''_{q0}} & 0 & 0 & 0 \\ 0 & 0 & 0 & 0 & 0 \\ 0 & 0 & 0 & 0 & \frac{\omega_s}{2H} \end{bmatrix} \begin{bmatrix} I_d \\ I_q \\ I_0 \\ E_{fd} \\ T_M - T_e \end{bmatrix} \tag{43}$$

$$+ \begin{bmatrix} S_{fd} \\ 0 \\ S_{1q} \\ 0 \\ 0 \\ 0 \end{bmatrix}$$

If the generator were linear, generator differential equations could be excited separately with positive and negative sequence components of the d and q axis currents (by making two of the three components zero in (33)). Linearity of differential equations would ensure that the frequency of all the generator states and hence the updated terminal voltages in the dq0 frame would be the same as that of the excitation. The updated d and q axis voltages obtained with positive sequence excitation could then be substituted in (33) to give the updated positive sequence voltage phasor in the abc frame. Similarly, the updated d and q frame voltages obtained with negative sequence

component of the current would give the updated negative sequence voltage phasor in the abc frame. The updated zero sequence voltage phasor would simply be the voltage drop across the generator's zero sequence impedance, since the negative sequence currents do not affect the solution of differential equations as seen in (34)-(42). Once the updated sequence voltages were available, (29) would give the updated abc frame voltage phasors. Unfortunately, the generator nonlinearities mentioned above prevent the application of this simple procedure for correctly obtaining the three phase abc frame phasors during each integration step.

3.5 Approach Developed in TPDA to Obtain Three Phase Network Voltages

In this section the approach developed in TPDA to correctly interface unbalanced networks with differential equation equipment models, such as synchronous generators, is discussed. This approach involves first calculating six $dq0$ frame voltages during an integration step, three each at two time instants, and then using the six values to obtain the three abc frame voltage phasors. The details of the procedure are discussed below, which show that the developed approach works equally well for balanced networks.

3.5.1 Obtaining six dq0 Frame Voltages

A portion of [17], which is an article where the author of this dissertation is the first author, is used in this section. IEEE holds the copyright to the original article, [17], whose citation can be found in the Bibliography. The reuse is in accordance with IEEE's policy at the time of writing the dissertation, which can be found in the Appendix.

Let it be assumed that the present simulation time instant is t and the updated voltage phasor is to be obtained for time $t + \Delta T$ (ΔT is the integration step). In the first step, $\boldsymbol{I}_{dq0}(t) = [I_d(t), I_q(t), I_0(t)]$, calculated using (27), is used to solve the generator rotor differential equations. However, instead of solving the differential equations up to $t + \Delta T$, as is the normal

practice, TPDA solves the equations from t to $t + \Delta T - \epsilon;\ \epsilon \ll \Delta T$ (based on simulations run thus far, all ϵ values smaller than $\Delta T/10$ give similar results). Since ΔT is already very small (a minimum value of 1/4th of a cycle is used), negligible error is introduced in the dynamic states of the generator rotor from the states obtained if the integration step was $t + \Delta T$.

Next, the new generator states, along with $\boldsymbol{I}_{dq}(t)$, are used to calculate $\psi_q(t + \Delta T - \epsilon)$ and $\psi_d(t + \Delta T - \epsilon)$ (using the expressions shown with the stator algebraic equations above), which are substituted in (40) and (41) to obtain $\mathbf{v}_{dq}(t + \Delta T - \epsilon)$, while $I_0(t)$ is substituted in (42) to obtain $v_0(t)$. As a result, the first three of the desired six $dq0$ frame voltages are now available as a 3X1 vector $\mathbf{v}_{dq0}(t + \Delta T - \epsilon)$.

To obtain the remaining three $dq0$ frame voltages, $\boldsymbol{i}_{abc}(t + \Delta T - \epsilon)$ is calculated using the current phasors obtained at time t, since it is assumed that the current waveform does not change between t and $t + \Delta T$. $\boldsymbol{i}_{abc}(t + \Delta T - \epsilon)$ is transformed into $\boldsymbol{I}_{dq0}(t + \Delta T - \epsilon)$ using Park's transform and used along with the generator states at $t + \Delta T$ (same as the states at $t + \Delta T - \epsilon$) to obtain $\psi_q(t + \Delta T)$ and $\psi_d(t + \Delta T)$, which when substituted in (40)-(42) gives $\mathbf{v}_{dq0}(t + \Delta T)$. Therefore, six $dq0$ frame voltages are now available to uniquely calculate the three abc frame voltage phasors at the generator terminal.

3.5.2 Calculation of Three Phase Voltage Phasors from Six $dq0$ Frame Voltages

A portion of [17], which is an article where the author of this dissertation is the first author, is used in this section. IEEE holds the copyright to the original article, [17], whose citation can be found in the Bibliography. The reuse is in accordance with IEEE's policy at the time of writing the dissertation, which can be found in the Appendix.

For calculating the three phase voltage phasors, the six $dq0$ frame voltages are first converted into the abc frame instantaneous voltages using (25). If $t_1 = t + \Delta T - \epsilon$ and $t_2 = t + \Delta T$, the relation between the $dq0$ and abc frame voltages at t_1 and t_2 is:

$$\mathbf{v}_{dq0}(t_1) = \mathbf{T}(t_1) * \mathbf{v}_{abc}(t_1) \tag{44}$$

$$\mathbf{v}_{dq0}(t_2) = \mathbf{T}(t_2) * \mathbf{v}_{abc}(t_2) \tag{45}$$

Since $\mathbf{T}(t)$ is always invertible (determinant is $2/3\sqrt{3}$), (44) and (45) can be used to calculate unique values of $\mathbf{v}_{abc}(t_1)$ and $\mathbf{v}_{abc}(t_2)$.

Once the unique values of $\mathbf{v}_{abc}(t_1)$ and $\mathbf{v}_{abc}(t_2)$ are obtained, the three voltage phasors can be calculated using the Fourier series expansion for the nominal frequency. The derivation for obtaining the phasors is given below.

Let $Ve^{j\theta}$ be the voltage phasor of phase A. Let x_1 and x_2 be its instantaneous values at t_1 and t_2, which are equal to the first elements of vectors $\mathbf{v}_{abc}(t_1)$ and $\mathbf{v}_{abc}(t_2)$, respectively.

In the time domain the voltage phasor can be expressed as a cosine waveform such as the one in (46).

$$x(t) = \sqrt{2}Vcos(\omega_s t + \theta) \tag{46}$$

Equation (46) can be expanded using the standard trigonometric identity for the cosine of two angles into (47).

$$x(t) = \sqrt{2}Vcos(\omega_s t)\cos(\theta) - \sqrt{2}Vsin(\omega_s t)\sin(\theta) \tag{47}$$

Denoting $\sqrt{2}V\cos(\theta)$ by A and $-\sqrt{2}V\sin(\theta)$ by B, (47) can be written as (48)

$$x(t) = Acos(\omega_s t) + Bsin(\omega_s t) \tag{48}$$

Since x_1 and x_2 are two samples of (48) at times t_1 and t_2 these can be written as (49) and (50), respectively.

$$x_1 = Acos(\omega_s t_1) + Bsin(\omega_s t_1) \tag{49}$$

$$x_2 = Acos(\omega_s t_2) + Bsin(\omega_s t_2) \tag{50}$$

A and B can be calculated from (49) and (50) using the formula in (51) as long as $t_2 - t_1 \neq \frac{n\pi}{\omega_s}$; $n \in \mathbb{Z}_{\geq 0}$.

$$\begin{bmatrix} A \\ B \end{bmatrix} = \frac{\begin{bmatrix} sin(\omega_s t_2) & -sin(\omega_s t_1) \\ -cos(\omega_s t_2) & cos(\omega_s t_1) \end{bmatrix}}{sin(\omega_s(t_2 - t_1))} \begin{bmatrix} x_1 \\ x_2 \end{bmatrix} \tag{51}$$

The magnitude and phase angle of the voltage waveform can be obtained using (52)-(55) and the values of A and B obtained using (51).

$$\sqrt{2}Vcos(\theta) = \frac{x_1 sin(\omega_s t_2) - x_2 sin(\omega_s t_1)}{sin(\omega_s(t_2 - t_1))} \tag{52}$$

$$\sqrt{2}Vsin(\theta) = \frac{x_1 cos(\omega_s t_2) - x_2 cos(\omega_s t_1)}{sin(\omega_s(t_2 - t_1))} \tag{53}$$

$$V = \left(\frac{1}{\sqrt{2}}\right)\sqrt{\left(\sqrt{2}Vcos(\theta)\right)^2 + \left(\sqrt{2}Vsin(\theta)\right)^2} \tag{54}$$

$$\theta = atan2\left(\sqrt{2}Vsin(\theta), \sqrt{2}Vcos(\theta)\right) \tag{55}$$

The phase B and C voltage phasors at time $t + \Delta T$ are also calculated by applying (52) - (55) to the 2nd and 3rd elements of $\mathbf{v}_{abc}(t_1)$ and $\mathbf{v}_{abc}(t_2)$, respectively.

3.6 Architecture of TPDA and its Key Features

The previous section discussed the approach developed for interfacing the dynamic model of synchronous generators with three phase, unbalanced network models in TPDA. In this section, the overall architecture of TPDA, its key features, and the assumptions and limitations of TPDA are discussed.

3.6.1 Partitioned-Implicit Approach for Solving the DAEs

The algorithm of TPDA is presented in the flowchart of Fig. 17. Table 10 explains the symbols used in Fig. 17. A portion of [53], which is an article where the author of this dissertation is the first author, is used in this section. IEEE holds the copyright to the original article, [53], whose citation can be found in the Bibliography. The reuse is in accordance with IEEE's policy at the time of writing the dissertation, which can be found in the Appendix.

Table 10: Definition of Symbols Used in the Flowchart of Fig. 17 [17]. © 2016 IEEE

Symbol	Definition
$i; j$	Counter for buses with dynamic models; counter for simulation iterations
TOT_MC; MAXITER	Constant representing total # of buses with dynamic models; Constant representing total # of simulation iterations
ΔT; ϵ	Integration time step; a small number<<ΔT
$\bar{\mathbf{v}}_{abc_i}(t); \bar{\mathbf{I}}_{abc_i}(t)$	Vectors of voltage and current phasor at bus i at time t
$\mathbf{v}_{abc_i}(t); \mathbf{I}_{abc_i}(t)$	Instantaneous voltage and current vectors for bus i at time t
$\mathbf{v}_{dq0_i}(t); \mathbf{I}_{dq0_i}(t)$	$dq0$ frame voltage and current vectors for bus i at time t
Flag	Ensures that at each simulation iteration $\mathbf{v}_{dq0_i}(t + \Delta T - \epsilon)$ and $\mathbf{v}_{dq0_i}(t + \Delta T)$ are correctly calculated
$\mathbf{x}_{interface_i}(t)$	State vector of dynamic model (e.g. synchronous generator) that directly connects at the i^{th} bus

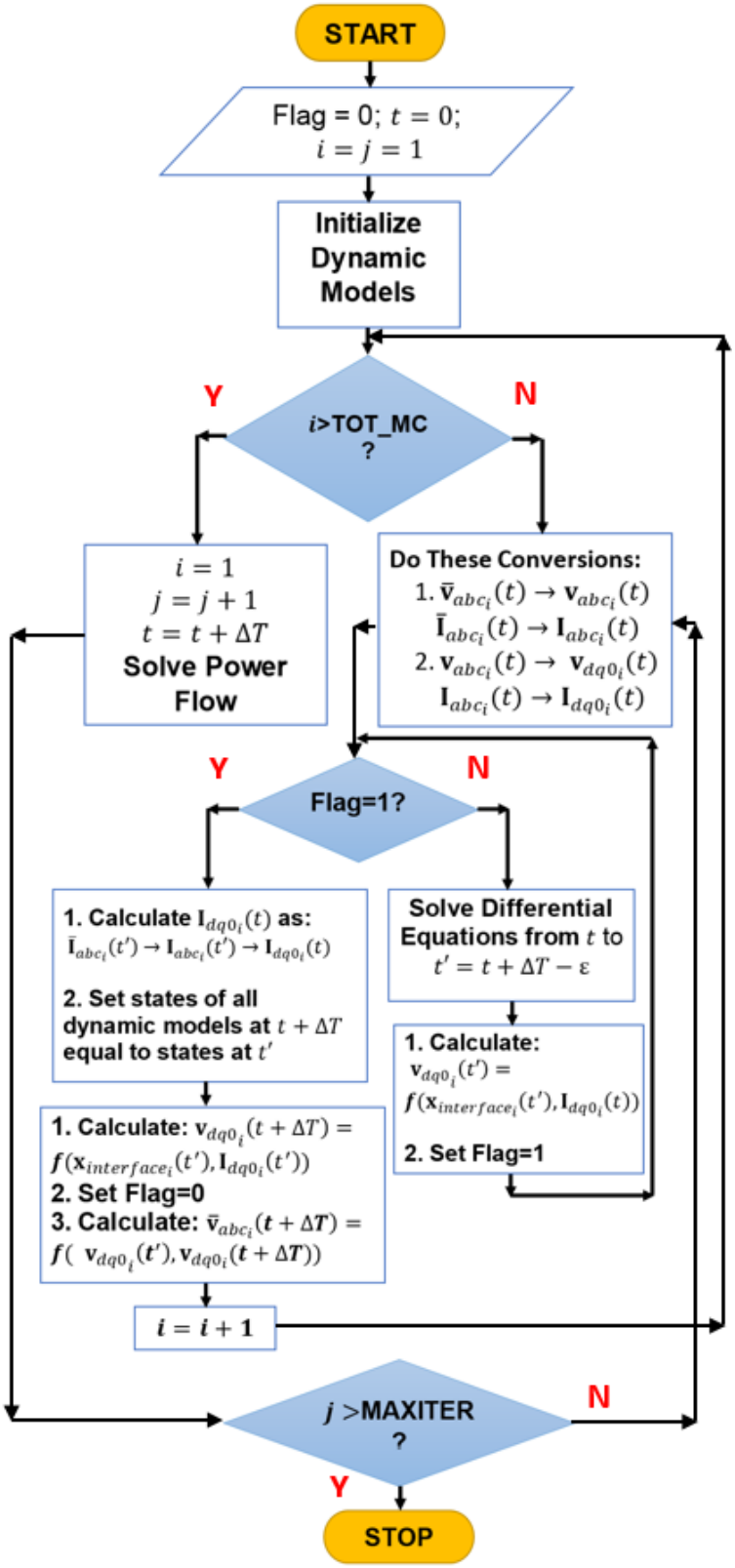

Fig. 17: Flowchart of Algorithm used in TPDA [17]. © 2016 IEEE

The algorithm shows that TPDA uses the sequential, or the partitioned method, for solving the DAEs. As a result, any integration method (explicit or implicit) can be used to solve the differential equations, and any nonlinear equation solver can be used for solving the algebraic equations. At present, the differential equations are solved using the trapezoidal method as implemented in the ode23t function of MATLAB, while the DEW software is used to solve the three phase, unbalanced network algebraic equations. As a result, the DAE solution approach adopted in TPDA is a partitioned approach with implicit integration (partitioned-implicit approach), since the trapezoidal method is an implicit integration method. Interested readers are referred to [6] for a detailed discussion on the various approaches for solving the DAEs for simulating power systems dynamics.

There are a number of reasons for using the partitioned-implicit approach instead of the simultaneous-implicit approach [48] where the non-linear DAEs are solved together in each integration step after converting the differential equations into algebraic equations using implicit integration methods such as the trapezoidal method. These include [17], [53]:

- The implementation of the partitioned approach is simple [48], [7] and it provides the flexibility to independently choose differential and algebraic equation solvers.
- DEW has been used for power flow analysis of large, multi-phase, unbalanced power systems for nearly two decades. Therefore, using DEW for solving the algebraic equations in the TPDA improves its reliability and robustness.
- This approach affords the flexibility to switch to a different numerical integration method if an existing method exhibits numerical instability. Moreover, new dynamic models can be easily added in the program with little modification to the code.

- As discussed in the last chapter, DEW uses GTA to perform power flow analysis. Since a network with loops is solved by splitting it into a number of smaller radial networks, it is possible to use parallel computation techniques to solve each radial network on a separate processor [54], which can reduce the time required to solve the algebraic equations during an integration step.
- Time for solving the DAEs can be further reduced if the differential equations are solved by distributing them across multiple cores because in the partitioned approach the differential equations can be solved in any order during an integration step.

3.6.2 Modeling of Synchronous Generators as Voltage Sources

As was discussed in the last section, at the end of each integration step voltages at the terminals of synchronous generators are made available for solving the network algebraic equations in the next time step. In other words, synchronous generators (or synchronous motors) are modeled as three-phase voltage sources at the interface with the network in TPDA, unlike many commercial programs, where synchronous generators are modeled as current sources. Representation of synchronous generators as voltage sources is closer to their actual operation.

3.6.3 Models for Synchronous Generator Exciters

A portion of [53], which is an article where the author of this dissertation is the first author, is used in this section. IEEE holds the copyright to the original article, [53], whose citation can be found in the Bibliography. The reuse is in accordance with IEEE's policy at the time of writing the dissertation, which can be found in the Appendix.

Exciters for synchronous generators use a direct current signal proportional to the terminal voltage for regulating the generator field current (and hence the terminal voltage). If the network is balanced, this input can be the voltage phasor magnitude of any phasor as the three phasors have

equal magnitude. Under unbalanced system conditions, however, some mechanism is needed to combine the three phase voltages and generate a single voltage input for the exciter. In TPDA, the average of the three phasor magnitudes is used to generate this signal. This strategy mimics the operation of a three phase rectifier generating the terminal voltage input for an exciter [55]. The exciter models included in TPDA are based on the IEEE standard 421.5-2005 [56].

3.6.4 Models for Synchronous Generator Turbine/Governors

The models for synchronous generator turbine/governors used in TPDA are the industry standard models that are used for dynamic simulations. GGOV1, TGOV1, and HYGOV [57], represent some of the turbine/governor models that have been included in TPDA. These models are written in Matlab.

Unlike the modeling of exciters, for which the three phase terminal voltages need to be reduced to a single input, no such modification is needed for turbine/governor models, because the inputs to these models are the generator rotor speed and/or the electrical power being generated by the generator.

3.6.5 Model for Distributed Solar PV

As was mentioned earlier, one of the primary objectives of TPDA is to study the impact of DG on power systems using Integrated T&D models. Of all the DG technologies that exist today, solar photovoltaics or solar PV is the dominant technology, and its penetration levels have increased exponentially over the last few years, and the trend is expected to persist in the near future [58]. Therefore, a model of small solar PV-based DG was developed that could interface with unbalanced networks. This model is discussed in the next chapter.

3.6.6 Initialization under Unbalance

Simulation of power systems dynamics begins with the initialization of all the dynamic equipment models in the study network (e.g., synchronous generators, exciters, governors, etc.). This section discusses the challenge of initializing the dynamic equipment models under unbalanced network conditions, and the approach used in TPDA for initializing them.

Initialization of a dynamic simulation typically starts from a solved power flow. The voltages and currents obtained from the power flow are used to calculate the initial states of dynamic equipment (e.g., synchronous generators) and their controllers (e.g., exciters and governors). To keep the discussion simple, the challenge for initializing dynamic equipment with unbalanced network models is highlighted first by focusing on the initialization of a synchronous generator. Later, the method used in TPDA to initialize synchronous generators and its controllers is discussed. The initialization of solar PV models will be discussed in the next chapter.

The state equations describing the generator were presented earlier and can be written compactly as (56).

$$\dot{\mathbf{x}} = f(\mathbf{x}, i_{dq0}(t)) \tag{56}$$

In (56), $\mathbf{x}$ is the state vector at time t; $i_{dq0}(t)$ is the terminal current obtained from the power flow expressed in the $dq0$ frame at time t; and $f()$ is the nonlinear function of derivatives.

As was shown earlier, in a balanced network, the d and q axis currents are always dc values and the zero sequence current is zero. Therefore, at steady state ($t = 0$) the generator can be initialized by solving (57), and the resulting states are used to calculate the field excitation voltage and mechanical power input values, which can be used to initialize the exciter and governor, if modeled.

$$\mathbf{0} = f(\mathbf{x}, i_{dq_{t=0}}) \tag{57}$$

As long as the network is not disturbed from its steady state at $t = 0$, the right hand side of (57) will continue to be zero (unless the equilibrium point is unstable or the software is numerically unstable). In other words, solving (57) for a balanced network will give the initial equilibrium point for the dynamic simulation, and the dynamic response of the network to various disturbances (e.g., faults, sudden change in load or generation, line outages) that move the system away from the equilibrium can be studied.

When the network is unbalanced, the $dq0$ frame currents and voltages vary with time, as was discussed earlier. Therefore, the left hand side of (56) cannot be zero for more than an instant, and the dynamic system can only attain an oscillatory equilibrium, i.e. all rotor quantities in the $dq0$ frame will have constant magnitudes and phase angles at the steady state. Therefore, the initialization procedure discussed above for the balanced system should be modified to obtain the oscillatory equilibrium of the system.

References [52] and [59] discuss a method for initializing the synchronous generators in unbalanced networks, provided the generator saturation is neglected, i.e., $f()$ in (56) is a linear function. As was discussed earlier, under the assumption of a linear rotor electrical circuit, the synchronous generator can be initialized separately with positive and negative sequence currents, and the results of each initialization can be superimposed to obtain the total initial values of generator states at $t = 0$. In this scenario, initial mechanical torque is calculated as the sum of positive sequence torque and the constant part of the negative sequence torque, while the field excitation voltage and rotor angle is calculated from the positive sequence initialization. Since the torsional vibrations are neglected, the generator is assumed to be at the synchronous speed at the time of initialization.

As is the normal practice, the above initialization procedure of [52] and [59] begins from a power flow. Since the network can be unbalanced, a three phase power flow is used to obtain the three phase currents and voltages at the generator terminals. For the power flow, the synchronous machine is represented in the abc frame as a symmetrical voltage source behind a symmetric impedance. The symmetric impedance matrix is obtained based on the assumption that the positive and negative sequence impedances are equal and the three sequence impedances are de-coupled [52]. For the nominal frequency negative sequence currents (network harmonics are neglected at the time of initialization in [52]), the imaginary part of the negative sequence impedance is very close to the average of X_d'' and $X_q{}''$, as shown in [7]. The zero sequence impedance values are part of the input data. However, as most generators are connected by delta-wye ground transformers, the zero sequence currents are zero, and hence the value of zero sequence impedance becomes immaterial.

This initialization procedure results in a system that is at its oscillatory equilibrium from $t = 0$ onwards. Unfortunately, as was shown earlier, in the presence of generator saturation, the positive and negative sequence initialization cannot be decoupled, as the saturation depends on both the d and q axis flux. Therefore, this approach cannot guarantee an oscillatory equilibrium right from the start when $f()$ in (56) is nonlinear. This limitation is discussed in [52], where the authors expect oscillations to persist for some time after initialization before the true steady state is established.

At present, the initialization procedure in TPDA is based on solving (57). This results in the calculation of the exact equilibrium point at the time of initialization when the network is balanced. When the network is unbalanced, however, this procedure generates initial conditions that are close to, but not at the true equilibrium, because the time derivatives of all the generator states in the $dq0$ frame cannot be assumed to be zero at the same time in the presence of negative sequence

currents, as the equilibrium point is an oscillatory equilibrium, and not a static one. Therefore, the simulation is allowed to run for a few iterations till an equilibrium is attained. Similar to [59], the synchronous machine is represented as a symmetrical voltage source behind a symmetrical impedance matrix at the time of initialization. Moreover, the mechanical torque that the turbine/governor is generating at the time of initialization is calculated using the sum of positive sequence torque and the average value of negative sequence torque. While the next chapter will show some of the case studies where this approach resulted in the steady state to be practically present right from the instant of initialization, the normal steady state operations of power systems also lends support for this approach of initialization as is discussed next.

The primary objective of dynamics studies in power systems is to study disturbances that push the power system away from its steady state operating conditions. Under steady state operating conditions the level of unbalance in the transmission system cannot exceed certain limits. For instance, the continuous negative sequence current in synchronous generators is restricted to 10% of the rated stator current [60], and grid codes set stringent limits on the acceptable voltage unbalance in the power system under normal operating conditions [61]. Therefore, at the time of initialization it can be reasonably assumed that while the generator states in the system are oscillating in the $dq0$ frame about a dc value, the amplitudes of the oscillations are significantly smaller than the magnitude of the dc component.

Please note that the above is not an argument for disregarding network unbalance at steady state for all power systems studies. It has been shown that neglecting unbalance at steady state can affect power systems design decisions, which in turn can affect the planning and operations of power systems [62]-[64]. The approach of initialization discussed is a simple way of starting the dynamic

simulations close to the actual steady state, and letting the system converge to its actual steady state fast by exploiting the power systems operating practices at steady state.

3.6.7 Assumptions and Limitations of TPDA

1. Network transients are neglected, and the network is assumed to transition from one steady state to the other at the nominal frequency. During transients, the network frequency will deviate from its steady state value. However, for stability studies variations in the nominal frequency are typically disregarded [7], and this assumption is also made in TPDA.
2. During an integration step, the current and voltage waveforms are assumed to be the same, i.e., their amplitudes and phase angles in the abc frame are kept fixed. This assumption was used in the calculation of three phase voltage phasors at the end of each integration step as discussed earlier.
3. Generator stator transients are also neglected to remain consistent with the assumption of neglecting network transients.
4. As a result of neglecting the network transients, electromagnetic transients cannot be studied using TPDA. For the study of such transients, an Electro-Magnetic Transients Program (EMTP), such as the Alternate Transients Program (ATP), should be used.

3.7 Concluding Remarks

The objective of this chapter was to discuss the approach developed in TPDA to perform dynamic simulations when the network is unbalanced. The reasons for selecting the particular approach and the key features of TPDA were discussed. The next chapter presents a dynamic model for small solar PV-based DG that will be used with TPDA for solar PV impact assessment studies using integrated T&D network models in chapter 6.

CHAPTER 4: DYNAMIC MODEL OF SOLAR PV-BASED DISTRIBUTED GENERATION

4.1 Introduction

Developing dynamic models of solar PV-based DG is complicated by the lack of publically available information about the controller models and control algorithms used in the inverters. These algorithms and models are proprietary and can vary widely with the vendor. Solar PV dynamic models developed by WECC [65], [66] are the only standard, vendor independent models known to the author that can be used in dynamic simulation studies involving large networks. Two types of WECC models are available: (i) models for simulating utility scale solar PV power plants, and (ii) a model for simulating small distribution connected solar PV units or the aggregated behavior of multiple distribution connected solar PV units at the high voltage transmission bus, which is called as PVD1 [65]. These models capture the general behavior expected of various control modules in a solar PV power plant without considering how such behavior is actually implemented by various vendors. As a result, it is possible to assess the impact of different solar PV plants on power systems dynamics by assigning different values to model parameters. At the same time, these models are designed to study slow electrical phenomenon (frequency less than 10 Hz) such as electromechanical transients, and hence do not need to model the high bandwidth power electronic switching controls, which makes them suitable for bulk power system dynamics studies.

These features of the WECC models, along with the phasor current output, are well suited for TPDA because TPDA is also intended to study slow transients in power systems using three phase, phasor based models of electric networks. The PVD1 model, therefore, became the basis for developing a dynamic model of small solar PV units that can be used to model solar PV-based

distributed generation in TPDA. From hereafter, unless specified, solar PV will refer to small solar PV units that are typically connected with the distribution network.

4.2 Dynamic Model for Small Solar PV Units

Solar panel arrays and grid tied inverter(s) are the primary components of a solar PV unit. This section discusses the key characteristics of the dynamic solar PV model developed in this work and the data flow between the model and the TPDA during dynamic simulations.

4.2.1 Key Features of the Solar PV Model

The PVD1 model is designed for use in traditional dynamic simulation programs that assume a balanced network topology [65]. Moreover, the PVD1 model is developed under the assumption that solar irradiance does not change from its initial value during the dynamic simulation. However, solar irradiation can change significantly within the typical time span of dynamic simulations (about 30 seconds) [65], [67]. Therefore, two modifications are made here to the PVD1 model for obtaining a solar PV model that can interface with unbalanced distribution networks, and whose real power output can be varied according to the incident solar irradiation. The modified PVD1 model is hereafter referred to as the D-PV model. The modifications made are:

- Reference active power in the D-PV model is calculated based on the typical solar panel array equations given in [68] and is changed if the solar irradiation changes. Reference reactive power is initialized based on the initial power flow, but can be changed by the user during the simulation.
- The model injects balanced currents into the network. Positive sequence voltage at the Point of Common Coupling (PCC) is used to calculate the currents needed by the D-PV model to generate the reference active and reactive powers.

The following two characteristics of power electronics based inverters justify the above modifications made to the PVD1 model:

- **High bandwidth of controllers used in inverters**: High bandwidth implies high speed control. In other words, solar PV units can transition from one steady state to the other very fast (e.g., within one nominal frequency cycle after a disturbance [69], [70]).
- **Flexibility afforded by power electronics to mold the behavior of solar PV units at the PCC** [69]: Unlike synchronous generators, whose interface with the network is governed by both physics and control, the interface of solar PV units is synthetic, i.e., for the time period of interest, behavior of solar PV units at the PCC is governed by the control algorithm implemented in the inverter.

Due to these characteristics, inverters can be designed to inject balanced currents, or generate balanced voltages, at their output terminals, even when the load at the terminals in unbalanced [70], [71]. Reference [72] also shows a real solar PV inverter that presents very high impedance to the flow of zero and negative sequence currents, implying that it predominantly generates balanced, positive sequence currents. Moreover, the injected current reaches its new steady state in less than a nominal frequency cycle, which demonstrates the high bandwidth of solar PV inverters.

Due to the injection of positive sequence currents at the PCC, the average real and reactive powers injected at the PCC can be calculated by using the positive sequence voltage at the PCC. This fact will be used later to develop expressions for currents that the D-PV model should inject to generate the reference real and reactive powers. Mathematically, this fact can be explained as follows. If V_a, V_b and V_c are the three phase line to neutral voltages at the PCC, and I_a, I_b and I_c are

the balanced currents that the solar PV unit is injecting, then the total complex power at the PCC is given by (58).

$$S = [V_a\ V_b\ V_c]\begin{bmatrix} I_a \\ I_b \\ I_c \end{bmatrix}^* \tag{58}$$

Based on the previous chapter, (58) can be written in terms of the sequence voltages and currents using the Fortescue Transformation.

$$S = [V_0\ V_1\ V_2]\mathbf{A}^T\mathbf{A}^*\begin{bmatrix} I_0 \\ I_1 \\ I_2 \end{bmatrix}^* \tag{59}$$

Since the current is balanced at the PCC, I_0 and I_2 are zero, which transforms (59) into (60) as $\mathbf{A}^T\mathbf{A}^* = 3\mathbf{I}$.

$$S = 3V_1I_1^* \tag{60}$$

Equation (60) shows that the actual real and reactive powers being injected at the PCC are a function of positive sequence voltages and currents.

It is important to note, however, that (60) does not imply that the instantaneous power at the PCC is constant and equal to the real part of (60), as is the case when the network is balanced. Under unbalance the instantaneous power includes a component that oscillates at twice the nominal frequency, and these oscillations can be attributed to the interaction between the negative sequence voltage at the PCC and the positive sequence currents injected by the D-PV model at the PCC, as shown below.

The instantaneous power at the PCC is given by (61).

$$P_{ac}(t) = [v_a(t)\ \ v_b(t)\ v_c(t)]\begin{bmatrix} i_a(t) \\ i_b(t) \\ i_c(t) \end{bmatrix}$$
$$= Re\left(\sqrt{2}[V_0\ V_1\ V_2]\mathbf{A}^T e^{j\omega_s t}\right) * Re\left(\sqrt{2}\mathbf{A}\begin{bmatrix} I_0 \\ I_1 \\ I_2 \end{bmatrix} e^{j\omega_s t}\right) \quad (61)$$

Since currents are balanced at the PCC, (61) can be written as (62).

$$P_{ac}(t) = Re\left(\sqrt{2}[V_0\ V_1\ V_2]\mathbf{A}^T e^{j\omega_s t}\right) * Re\left(\sqrt{2}\mathbf{A}\begin{bmatrix} 0 \\ I_1 \\ 0 \end{bmatrix} e^{j\omega_s t}\right) \quad (62)$$

If $[V_0;\ V_1;\ V_2] = [|V_0|e^{j\varphi_0};\ |V_1|e^{j\varphi_1};\ |V_2|e^{j\varphi_2}]$ and $[I_0;\ I_1;\ I_2] = [0;\ |I_1|e^{j\theta_1};\ 0]$, then (62) can be written as (63).

$$P_{ac}(t) = Re\left(\sqrt{2}[V_0\ V_1\ V_2]\mathbf{A}^T e^{j\omega_s t}\right) * Re\left(\sqrt{2}\mathbf{A}\begin{bmatrix} 0 \\ I_1 \\ 0 \end{bmatrix} e^{j\omega_s t}\right)$$

$= 2$

$$* \begin{bmatrix} |V_0|\cos(\omega_s t + \varphi_0) + |V_1|\cos(\omega_s t + \varphi_1) + |V_2|\cos(\omega_s t + \varphi_2) \\ |V_0|\cos(\omega_s t + \varphi_0) + |V_1|\cos\left(\omega_s t + \varphi_1 - \frac{2\pi}{3}\right) + |V_2|\cos\left(\omega_s t + \varphi_2 + \frac{2\pi}{3}\right) \\ |V_0|\cos(\omega_s t + \varphi_0) + |V_1|\cos\left(\omega_s t + \varphi_1 + \frac{2\pi}{3}\right) + |V_2|\cos\left(\omega_s t + \varphi_2 - \frac{2\pi}{3}\right) \end{bmatrix}^T \begin{bmatrix} |I_1|cos(\omega_s t + \theta_1) \\ |I_1|cos\left(\omega_s t + \theta_1 - \frac{2\pi}{3}\right) \\ |I_1|cos\left(\omega_s t + \theta_1 + \frac{2\pi}{3}\right) \end{bmatrix}$$

On simplifying, the above yields (63).

$$= 3|V_1||I_1|\cos(\varphi_1 - \theta_1) + 3|V_2||I_1|\cos(2\omega_s t + \varphi_2 + \theta_1) \quad (63)$$

Equation (63) confirms that while the constant part of the instantaneous power at the PCC is same as the real component of the complex power in (60), the second harmonic component arises due to the interaction between negative sequence voltages and the positive sequence currents, and its average value over one nominal frequency period is zero. From hereafter, in the context of the D-PV model, the use of terms real and reactive powers refers to their average values.

Since the ac power is time varying due to the control strategy implemented in the D-PV model, power balance between the dc and ac sides of a solar PV inverter that implements such a control strategy implies that the dc bus power should also vary with time. These variations appear as ripples on the voltage of the dc bus capacitor, although their magnitude can be limited by selecting a capacitor with large capacitance [69]. The assumption of large dc bus capacitance is made in the D-PV model, as the dc bus voltage is not changed from its initial value for the duration of the simulation. At present, no provision is made in the D-PV model to control or limit these oscillations. Although not included in the D-PV model, a simple protection function can be added that will trip the solar PV unit if the negative sequence voltage increases beyond a certain value that can damage the DC capacitor.

4.2.2 Equations for Controlling Real and Reactive Powers in the D-PV Model

In this section equations will be developed that can be used to implement independent real and reactive power control in the D-PV model. These equations relate the inverter currents to the real and reactive powers generated by the D-PV model, depending upon the type of transformer that connects the solar PV unit to the network.

Solar PV inverters typically connect with the ungrounded winding of the network transformer, and hence do not control the zero sequence component of the output current at the PCC [69]. Derivations of the real and reactive power control equations when the D-PV model of a solar PV unit connects to the grid through Wye-ground-Delta, Wye-ground-Wye and single phase transformers are discussed next.

Wye-ground-Delta Transformer

As stated earlier, the PCC is at the Wye-ground side of the Wye-ground-Delta transformer while the solar PV unit is connected on the Delta side. Since the inverter is assumed to inject balanced

currents at the PCC, the Delta side line current lags the Wye-ground side line current by 30 degrees (Ynd1 connection is being assumed). Therefore, if $I_Y = I_{abc}$ is the balanced current vector on the Wye-ground side and **T** is the Park's transformation matrix from the previous chapter with $\delta = 0$ then,

$$i_{dq0_Y} = \mathbf{T} * i_{abc_Y} \tag{64}$$

where $i_{abc_Y} = \left[\sqrt{2}I\cos(\omega t + \theta) \quad \sqrt{2}I\cos(\omega t + \theta - 120) \quad \sqrt{2}I\cos(\omega t + \theta + 120)\right]^T$; I and θ are the magnitude and phase angles of the balanced current phasor.

Since the currents being injected by the D-PV model are balanced, matrix $\mathbf{A_1} = \sqrt{3}Ne^{-\frac{j\pi}{6}}\mathbf{I}$ can be used to transform line current on the Wye-ground side to the line current on the Delta side. On the Delta side, the phasor line currents will transform as (65), which will result in the time domain expression of delta side line currents as given in (66).

$$I_{dq0_D} = \mathbf{A_1} * I_{dq0_Y} = \sqrt{3}e^{-\frac{j\pi}{6}}I_{dq0_Y} \tag{65}$$

$$\begin{aligned} & i_{abc_D} \\ & = \sqrt{3}\left[\sqrt{2}IN\cos(\omega t + \theta - 30) \quad \sqrt{2}IN\cos(\omega t + \theta - 150) \quad \sqrt{2}IN\cos(\omega t + \theta + 90)\right]^T \end{aligned} \tag{66}$$

Since the currents are balanced, the $dq0$ transformation of the Wye-ground side currents (in a frame of reference where the d axis of the $dq0$ frame is aligned with the positive sequence voltage vector on the Wye-ground side) results in a current vector that lags the d axis by $(\varphi - \theta)$ radians, where φ is the angle of the positive sequence voltage vector in the abc frame w.r.t to the real axis. Therefore, the angle of current in the synchronously rotating $dq0$ frame is $-(\varphi - \theta)$, and the d and q axis Wye-ground side currents become as given in (67).

$$i_{dq0_Y} = \left[\sqrt{2}Icos(-\varphi + \theta) \quad \sqrt{2}Isin(-\varphi + \theta) \quad 0\right]^T \tag{67}$$

Similarly, from (65), the Delta side $dq0$ currents in the above frame of reference become as given by (68).

$$i_{dq0_D} = \sqrt{3}\left[\sqrt{2}INcos(-\varphi + \theta - 30) \quad \sqrt{2}INsin(-\varphi + \theta - 30) \quad 0\right]^T \tag{68}$$

The expressions below show how the d and q axis currents on the Delta side affect the real and reactive powers injected by a solar PV unit at the PCC. Based on (60), the average real power at the PCC is given by (69), which can be written in terms of the Delta side d and q axis currents as shown in (70).

$$P_{ac} = real\left(3 * VI * e^{j(\varphi-\theta)}\right) \tag{69}$$

$$\Rightarrow P_{ac} = real\left(3 * Ve^{j\varphi}Ie^{-j\theta}\right)$$

$$\Rightarrow P_{ac} = real\left(3 * \frac{V}{N}e^{j\varphi}e^{-\frac{j\pi}{6}}e^{\frac{j\pi}{6}}NIe^{-j\theta}\right)$$

$$\Rightarrow P_{ac} = real\left(3 * \frac{V}{N}e^{j\varphi}e^{-\frac{j\pi}{6}}NIe^{-j\left(\theta-\frac{\pi}{6}\right)}\right)$$

$$\Rightarrow P_{ac} = real\left(3 * \frac{V}{N}e^{-\frac{j\pi}{6}}NIe^{-j\left(-\varphi+\theta-\frac{\pi}{6}\right)}\right)$$

$$\Rightarrow P_{ac} = real\left(\frac{\sqrt{3}}{\sqrt{2}} * \frac{V}{N}e^{-\frac{j\pi}{6}}\sqrt{3}\sqrt{2}NIe^{-j\left(-\varphi+\theta-\frac{\pi}{6}\right)}\right)$$

$$\Rightarrow P_{ac} = real\left(\frac{\sqrt{3}}{\sqrt{2}} * \frac{V}{N}\sqrt{3}\sqrt{2}NIe^{-j\left(-\varphi+\theta-\frac{\pi}{6}+\frac{\pi}{6}\right)}\right)$$

$$\Rightarrow P_{ac} = \frac{\sqrt{3}}{\sqrt{2}} * \frac{V}{N}real\left(\sqrt{3}\sqrt{2}NIe^{-j\left(-\varphi+\theta-\frac{\pi}{6}+\frac{\pi}{6}\right)}\right)$$

$$\Rightarrow P_{ac} = \frac{\sqrt{3}}{\sqrt{2}} * \frac{V}{N}\left(\sqrt{3}\sqrt{2}NIcos(-\varphi + \theta - \frac{\pi}{6} + \frac{\pi}{6})\right)$$

$$\Rightarrow P_{ac} = \frac{\sqrt{3}}{\sqrt{2}} * \frac{V}{N}\left(\sqrt{3}\sqrt{2}NI\left(cos\left(-\varphi + \theta - \frac{\pi}{6}\right)\cos\left(\frac{\pi}{6}\right) - sin\left(-\varphi + \theta - \frac{\pi}{6}\right)\sin\left(\frac{\pi}{6}\right)\right)\right)$$

$$\Rightarrow P_{ac} = \frac{\sqrt{3}}{\sqrt{2}} * \frac{V}{N}\left(i_{d_D}\cos\left(\frac{\pi}{6}\right) - i_{q_D}\sin\left(\frac{\pi}{6}\right)\right)$$

$$\Rightarrow P_{ac} = \frac{\sqrt{3}}{\sqrt{2}} * \frac{V}{N}\left(i_{d_D}\frac{\sqrt{3}}{2} - \frac{i_{q_D}}{2}\right) \tag{70}$$

To account for real power losses in the transformer, transformer impedance can be reflected on the network side, and three times the ohmic loss in each phase can be added to (70) because the current is balanced. The resulting total real power on the Delta side, or the inverter side of the solar PV unit, P_{ac_D}, is given by (71) by using (68) to express I in terms of the d and q axis currents on the Delta side.

$$P_{ac_D} = P_{ac} + 3 * I^2R$$

$$\Rightarrow P_{ac_D} = \frac{\sqrt{3}}{\sqrt{2}} * \frac{V}{N}\left(i_{d_D}\frac{\sqrt{3}}{2} - \frac{i_{q_D}}{2}\right) + \frac{1}{2N^2}\left(i_{d_D}^{\,2} + i_{q_D}^{\,2}\right)R \tag{71}$$

An expression, similar to (70), can be written for the average reactive power Q_{ac} injected by the inverter at the PCC. Based on (60), the expression for Q_{ac} at the PCC can be written as (72).

$$Q_{ac} = imag\left(3 * VI * e^{j(\varphi-\theta)}\right)$$

$$Q_{ac} = imag\left(3 * Ve^{j\varphi}Ie^{-j\theta}\right)$$

$$\Rightarrow Q_{ac} = imag\left(3 * \frac{V}{N}e^{j\varphi}e^{-\frac{j\pi}{6}}e^{\frac{j\pi}{6}}NIe^{-j\theta}\right)$$

$$\Rightarrow Q_{ac} = imag\left(3 * \frac{V}{N}e^{j\varphi}e^{-\frac{j\pi}{6}}NIe^{-j\left(\theta-\frac{\pi}{6}\right)}\right)$$

$$\Rightarrow Q_{ac} = imag\left(3 * \frac{V}{N}e^{-\frac{j\pi}{6}}NIe^{-j\left(-\varphi+\theta-\frac{\pi}{6}\right)}\right)$$

$$\Rightarrow Q_{ac} = imag\left(\frac{\sqrt{3}}{\sqrt{2}} * \frac{V}{N}e^{-\frac{j\pi}{6}}\sqrt{3}\sqrt{2}NIe^{-j\left(-\varphi+\theta-\frac{\pi}{6}\right)}\right)$$

$$\Rightarrow Q_{ac} = imag\left(\frac{\sqrt{3}}{\sqrt{2}} * \frac{V}{N}\sqrt{3}\sqrt{2}NIe^{-j\left(-\varphi+\theta-\frac{\pi}{6}+\frac{\pi}{6}\right)}\right)$$

$$\Rightarrow Q_{ac} = \frac{\sqrt{3}}{\sqrt{2}} * \frac{V}{N} imag\left(\sqrt{3}\sqrt{2}NIe^{-j\left(-\varphi+\theta-\frac{\pi}{6}+\frac{\pi}{6}\right)}\right)$$

$$\Rightarrow Q_{ac} = -\frac{\sqrt{3}}{\sqrt{2}} * \frac{V}{N}\left(\sqrt{3}\sqrt{2}NIsin\left(-\varphi+\theta-\frac{\pi}{6}+\frac{\pi}{6}\right)\right)$$

$$\Rightarrow Q_{ac} = -\frac{\sqrt{3}}{\sqrt{2}} * \frac{V}{N}\sqrt{3}\sqrt{2}NI\left(sin\left(-\varphi+\theta-\frac{\pi}{6}\right)\cos\left(\frac{\pi}{6}\right)+\sin\left(\frac{\pi}{6}\right)cos\left(-\varphi+\theta-\frac{\pi}{6}\right)\right)$$

$$\Rightarrow Q_{ac} = -\frac{\sqrt{3}}{\sqrt{2}} * \frac{V}{N}\left(i_{q_D}\frac{\sqrt{3}}{2}+\frac{i_{d_D}}{2}\right) \quad (72)$$

Similar to the calculations to account for real power losses in the transformer, the reactive power loss can be added to the expression of reactive power in (72) to yield the reactive power on the inverter side of the transformer, Q_{ac_D}, which is given in (73).

$$Q_{ac_D} = -\frac{\sqrt{3}}{\sqrt{2}} * \frac{V}{N}\left(i_{q_D}\frac{\sqrt{3}}{2}+\frac{i_{d_D}}{2}\right)+\frac{1}{2N^2}\left(i_{d_D}^2+i_{q_D}^2\right)X \quad (73)$$

Equations (71) and (73) can be solved for i_{q_D} and i_{d_D}, which when substituted in (68) will yield the magnitude and phase angle of the balanced three phase current that will generate the reference real and reactive powers, P_{ac_D} and Q_{ac_D} (the phase angle obtained will be for phase A, angles for phases B and C will lead the phase A angle by -120 degrees and 120 degrees, respectively). Equations (71) and (73) ensure that unless the voltage at the PCC becomes so low that the current exceeds the inverter ratings and the current output is capped at the rated value, the D-PV model can inject currents such that P_{ac_D} and Q_{ac_D} are generated on the Delta side of the transformer.

Please note that P_{ac_D} is the reference real power that is determined by the incident solar irradiation and the dc voltage at the panel terminals, which is not changed from its initial value in the D-PV model for the duration of the simulation. Therefore, the real power injected at the PCC will be P_{ac_D} minus the ohmic losses in the transformer. Similarly, the reactive power at the PCC

will be Q_{ac_D} minus the reactive power losses in the transformer. If the reference reactive power is specified at the PCC, (72) should be solved simultaneously with (71) to calculate the currents needed to generate the reference powers.

Wye-ground-Wye Transformer

The derivation of real and reactive power control expressions for the Wye-ground-Wye transformer is similar to that of the Delta-Wye-ground transformer. When a solar PV unit is interfaced to the network through a Wye-ground-Wye transformer, the PCC is on the Wye-ground side. Because of the Wye-ground-Wye transformer connection there is no phase shift in the currents on the primary and secondary sides. Therefore, if $I_{Yg} = I_{abc}$ is the positive sequence current vector on the Wye-ground side then:

$$i_{dq0_{Yg}} = \mathbf{T} * i_{abc_{Yg}} \tag{74}$$

where $i_{abc_{Yg}} = \left[\sqrt{2}I\cos(\omega t + \theta) \quad \sqrt{2}I\cos(\omega t + \theta - 120) \quad \sqrt{2}I\cos(\omega t + \theta + 120)\right]^T$.

Let matrix $\mathbf{A_1} = N\mathbf{I}$ be the matrix that transforms line current on the Wye-ground side to the line current on the Wye side. On the Wye side, the phasor line currents will transform as $I_{abc_Y} = \mathbf{A_1} * I_{Yg} = NI_{abc}$, which will result in the time domain expression of Wye side line currents as given in (75).

$$i_{abc_Y} = \left[\sqrt{2}IN\cos(\omega t + \theta) \quad \sqrt{2}IN\cos(\omega t + \theta) \quad \sqrt{2}IN\cos(\omega t + \theta)\right]^T \tag{75}$$

Since the currents are balanced, the $dq0$ transformation of the Wye-ground side currents (in a frame of reference where the d axis of the $dq0$ frame is aligned with the positive sequence voltage vector on the Wye-ground side) results in a current vector that lags the d axis by $(\varphi - \theta)$ radians, where φ is the angle of the positive sequence voltage vector in the abc frame w.r.t to the real axis.

Therefore, the angle of current in the synchronously rotating $dq0$ frame is $-(\varphi - \theta)$, and the d and q axis Wye-ground side currents become as shown in (76).

$$i_{dq0_{Yg}} = \begin{bmatrix} \sqrt{2}Icos(-\varphi + \theta) & \sqrt{2}Isin(-\varphi + \theta) & 0 \end{bmatrix}^T \tag{76}$$

Similarly, the Wye side $dq0$ frame currents in the above frame of reference become as shown in (77).

$$i_{dq0_{Y}} = \begin{bmatrix} \sqrt{2}INcos(-\varphi + \theta) & \sqrt{2}INsin(-\varphi + \theta) & 0 \end{bmatrix}^T \tag{77}$$

The expressions in (78) and (79) show the relation between the d and q axis currents on the Wye side and the average real and reactive powers injected by the solar PV inverter at the PCC.

$$P_{ac} = real\left(3 * VI * e^{j(\varphi-\theta)}\right)$$

$$\Rightarrow P_{ac} = 3 * \frac{V}{\sqrt{2}N}\sqrt{2}NIcos(\varphi - \theta)$$

$$\Rightarrow P_{ac} = \frac{3}{\sqrt{2}}\frac{V}{N} i_{dq0_Y}$$

$$\Rightarrow P_{ac} = \frac{3}{\sqrt{2}}\frac{V}{N} i_{d_Y} \tag{78}$$

$$Q_{ac} = imag\left(3 * VI * e^{j(\varphi-\theta)}\right)$$

$$Q_{ac} = 3 * VIsin(\varphi - \theta)$$

$$\Rightarrow Q_{ac} = 3 * \frac{V}{\sqrt{2}N}\sqrt{2}NIsin(\varphi - \theta)$$

$$\Rightarrow Q_{ac} = -3 * \frac{V}{\sqrt{2}N}\sqrt{2}NIsin(-\varphi + \theta)$$

$$\Rightarrow Q_{ac} = -3 * \frac{V}{\sqrt{2}N} i_{dq0_Y}$$

$$\Rightarrow Q_{ac} = -3 * \frac{V}{\sqrt{2}N} i_{q_Y} \tag{79}$$

Losses in the transformer can be accounted for as in the Wye-ground-Delta transformer case, which when added to (78) and (79) give the real and reactive powers on the Wye side as shown in (80) and (81), respectively. Equations (80) and (81) can be solved for i_{d_Y} and i_{q_Y}, which when substituted in (77) will yield the magnitude and phase angle of the balanced three phase current that should be injected by the solar PV unit to generate the reference real and reactive powers on the Wye side of the transformer. Similar to the Wye-ground-Delta transformer case, if the reference reactive power at the PCC is specified, (79) should be solved simultaneously with (80) to calculate the currents.

$$P_{ac_Y} = \frac{3}{\sqrt{2}}\frac{V}{N} i_{d_Y} + 3I^2R$$

$$= \frac{3}{\sqrt{2}}\frac{V}{N} i_{d_Y} + \frac{3}{2N^2}\left(i_{d_Y}^{\,2} + i_{q_Y}^{\,2}\right)R \tag{80}$$

$$Q_{ac_Y} = -3 * \frac{V}{\sqrt{2}N} i_{q_Y} + 3I^2X$$

$$= -3 * \frac{V}{\sqrt{2}N} i_{q_Y} + \frac{3}{2N^2}\left(i_{d_Y}^{\,2} + i_{q_Y}^{\,2}\right)X \tag{81}$$

Single Phase Transformer

For single phase solar PV units, independent control of real and reactive powers implies that the phase locked loop will follow the voltage vector, i.e., if $\bar{v} = Ve^{j\varphi}$ and $\bar{\imath} = Ie^{j\theta}$ at the PCC, then for control the orthogonal axes will be such that $v_{real} = V$ and $v_{imag} = 0$ resulting in the current vector getting modified to $i_{real} = Icos(-\varphi + \theta)$ and $i_{imag} = Isin(-\varphi + \theta)$. Therefore, real and reactive powers at the PCC are given by $P_{ac} = VIcos(-\varphi + \theta)$ and $Q_{ac} = -VIsin(-\varphi + \theta)$, respectively. As a result the real and reactive powers on the inverter side of the transformer can be written as (82) and (83), respectively (R and X are the transformer resistance and reactance values reflected on the network side).

$$P_{ac_I} = VIcos(-\varphi + \theta) + I^2R \tag{82}$$

$$Q_{ac_I} = VIsin(-\varphi + \theta) + I^2X \tag{83}$$

Equations (82) and (83) can be solved to calculate the magnitude and phase angle of the current that should be injected by the solar PV unit to generate the reference real and reactive powers on the inverter side of the transformer. If the reference reactive power at the PCC is specified, the reactive power loss term from (83) should be removed and the resulting equation should be solved with (82) to calculate the currents.

4.2.3 Simplifying the Equations for Controlling Real and Reactive Powers– Neglecting Real Power Losses

Equations (71), (73); (80), (81) and (82), (83) are non-linear equations. While closed form expressions relating d and q axis currents to the reference real and reactive powers can be obtained, these are quite involved. Given that distribution transformers have very high efficiencies [73], the real power loss can be neglected to simplify the control equations. With this simplification, the control equations for the three transformer connections become as given below.

Wye-ground-Delta:

$$P_{ac_D} = \frac{\sqrt{3}}{\sqrt{2}} * \frac{V}{N}\left(i_{d_D}\frac{\sqrt{3}}{2} - \frac{i_{q_D}}{2}\right) = P_{ac} \tag{84}$$

$$\Rightarrow i_{q_D} = \sqrt{3}i_{d_D} - \frac{2\sqrt{2}NP_{ac_D}}{\sqrt{3}V} \tag{85}$$

Substituting i_{q_D} from (85) into (73) gives (86)

$$Q_{ac_D} = -\frac{\sqrt{3}}{\sqrt{2}} * \frac{V}{N}\left(\frac{\sqrt{3}}{2}\left(\sqrt{3}i_{d_D} - \frac{2\sqrt{2}NP_{ac_D}}{\sqrt{3}V}\right) + \frac{i_{d_D}}{2}\right) + \frac{1}{2N^2}\left(\left(\sqrt{3}i_{d_D} - \frac{2\sqrt{2}NP_{ac_D}}{\sqrt{3}V}\right)^2 + i_{d_D}^2\right)X$$

$$= -\frac{\sqrt{3}}{\sqrt{2}} * \frac{V}{N}\left(\left(\frac{3i_{d_D}}{2} - \frac{\sqrt{2}NP_{ac_D}}{V}\right) + \frac{i_{d_D}}{2}\right) + \frac{1}{2N^2}\left(3i_{d_D}^2 + \frac{8N^2P_{ac_D}^2}{3V^2} - \frac{4\sqrt{2}NP_{ac_D}i_{d_D}}{V} + i_{d_D}^2\right)X$$

$$= -\frac{\sqrt{3}}{\sqrt{2}} * \frac{V}{N}\left(2i_{d_D} - \frac{\sqrt{2}NP_{ac_D}}{V}\right) + \frac{1}{2N^2}\left(3i_{d_D}^2 + \frac{8N^2P_{ac_D}^2}{3V^2} - \frac{4\sqrt{2}NP_{ac_D}i_{d_D}}{V} + i_{d_D}^{\ 2}\right)X$$

$$= -\frac{2\sqrt{3}}{\sqrt{2}} * \frac{Vi_{d_D}}{N} + \sqrt{3}P_{ac_D} + \frac{3Xi_{d_D}^2}{2N^2} + \frac{4XP_{ac_D}^2}{3V^2} - \frac{2\sqrt{2}XP_{ac_D}i_{d_D}}{NV} + \frac{2X}{N^2}i_{d_D}^{\ 2}$$

$$= \left(\frac{2X}{N^2}\right)i_{d_D}^{\ 2} - \left(\frac{2\sqrt{3}}{\sqrt{2}} * \frac{V}{N} + \frac{2\sqrt{2}XP_{ac_D}}{NV}\right)i_{d_D} + \sqrt{3}P_{ac_D} + \frac{4XP_{ac_D}^2}{3V^2}$$

$$\Rightarrow \left(\frac{2X}{N^2}\right)i_{d_D}^{\ 2} - \left(\frac{2\sqrt{3}}{\sqrt{2}} * \frac{V}{N} + \frac{2\sqrt{2}XP_{ac_D}}{NV}\right)i_{d_D} + \left(\sqrt{3}P_{ac_D} + \frac{4XP_{ac_D}^2}{3V^2} - Q_{ac_D}\right) = 0 \qquad (86)$$

Equation (86) is a quadratic equation, which can be solved to obtain an expression for i_{d_D}. This expression can be substituted in (85) to give the expression for i_{q_D}. The resulting expressions for i_{d_D} and i_{q_D} allow the reference real and reactive powers to be injected on the inverter side of the transformer during the dynamic simulation. As discussed earlier, if the reference reactive power at the PCC is specified, (85) should be solved simultaneously with (72) to calculate the currents.

Wye-ground-Wye

Neglecting ohmic losses in (80) gives (87), which when solved for i_{q_Y} gives (88).

$$P_{ac_Y} = \frac{3}{\sqrt{2}}\frac{V}{N}i_{d_Y} = P_{ac} \qquad (87)$$

$$\Rightarrow i_{d_Y} = \frac{\sqrt{2}}{3}\frac{NP_{ac_Y}}{V} \qquad (88)$$

Substituting (88) in (81) gives (89)

$$Q_{ac_Y} = -3 * \frac{V}{\sqrt{2}N}i_{q_Y} + \frac{3}{2N^2}\left(\frac{2}{9}\frac{N^2P_{ac_Y}^2}{V^2} + i_{q_Y}^{\ 2}\right)X$$

$$= -3 * \frac{V}{\sqrt{2}N}i_{q_Y} + \frac{XP_{ac_Y}^2}{3V^2} + \frac{3X}{2N^2}i_{q_Y}^{\ 2}$$

$$\Rightarrow \frac{3X}{2N^2} {i_{q_Y}}^2 - \frac{3V}{\sqrt{2}N} i_{q_Y} + \left(\frac{X P_{ac_Y}^2}{3V^2} - Q_{ac_Y} \right) = 0 \tag{89}$$

Equation (89) can be solved to obtain an expression for i_{q_Y}, which when substituted in (88) will give the expression for i_{d_Y}. Similar to the case for Wye-ground-Delta transformer, if the reference reactive power at the PCC is specified, (88) should be solved simultaneously with (79) to calculate the currents.

Single Phase Transformer

Neglecting the ohmic losses in (82) gives (90)

$$P_{ac_I} = VI\cos(-\varphi + \theta) = P_{ac} \tag{90}$$

Squaring (90) and adding it to the square of $\left(Q_{ac_I} - I^2 X\right)$ gives (91)

$$P_{ac_I}^2 + Q_{ac_I}^2 + I^4 X^2 - 2Q_{ac_I} I^2 X = V^2 I^2$$

$$\Rightarrow I^4 X^2 - 2Q_{ac_I} I^2 X - V^2 I^2 + P_{ac_I}^2 + Q_{ac_I}^2 = 0$$

$$\Rightarrow I^4 X^2 - \left(2Q_{ac_I} X - V^2\right) I^2 + P_{ac_I}^2 + Q_{ac_I}^2 = 0 \tag{91}$$

Equation (91) can be solved for I^2, and since I is a real number, only the positive value of I^2 should be used to calculate the value of I. Once the value of I is known, it can be substituted in (90) to obtain θ. If the reference reactive power at the PCC is specified, (90) should be solved simultaneously with (83), after removing the reactive power loss term, to calculate the current.

4.2.4 Simplifying the Equations for Controlling Real and Reactive Powers – Neglecting Real and Reactive Power Losses

If the transformers are assumed to be ideal, (71), (73); (80), (81) and (82), (83) become linear, and the d and q axis currents that the inverter should inject to generate the reference real and reactive powers at the inverter sides of the transformers are given by the expressions given in Table

11. Since transformer losses are neglected, the control of active and reactive powers on the inverter side of the transformer is equivalent to controlling the powers at the PCC.

Table 11: d and q axis Inverter Side Currents to Control Real and Reactive Powers when Transformer Losses are neglected

Transformer Connection	d axis inverter side current	q axis inverter side current
Wye-ground-Delta	$\left(\frac{N}{\sqrt{2}\sqrt{3}\lvert V\rvert}\right)(-Q_{ac}+\sqrt{3}P_{ac})$	$\left(\frac{N}{\sqrt{2}\sqrt{3}\lvert V\rvert}\right)(-\sqrt{3}Q_{ac}-P_{ac})$
Wye-ground-Wye	$\frac{\sqrt{2}N}{3\lvert V\rvert}P_{ac}$	$-\frac{\sqrt{2}N}{3\lvert V\rvert}Q_{ac}$
Single Phase	$\frac{N}{\lvert V\rvert}P_{ac}$	$-\frac{N}{\lvert V\rvert}Q_{ac}$

4.2.5 Interfacing the D-PV Model with the Network

Fig. 18 shows the block diagram of the D-PV model, including the data flow during dynamic simulations. The D-PV model includes a current limiter, which is implemented in the same manner as in the PVD1 model to limit the current supplied by the inverter during low voltage conditions at the PCC. It should be noted that the transformer that connects the inverter to the network is not part of the D-PV model. The transformer is part of the network model in which the solar PV unit is represented as a three phase current source. At the end of each integration step, the D-PV model of Fig. 18 uses the equations developed in the previous section to calculate the balanced three phase currents for the current source.

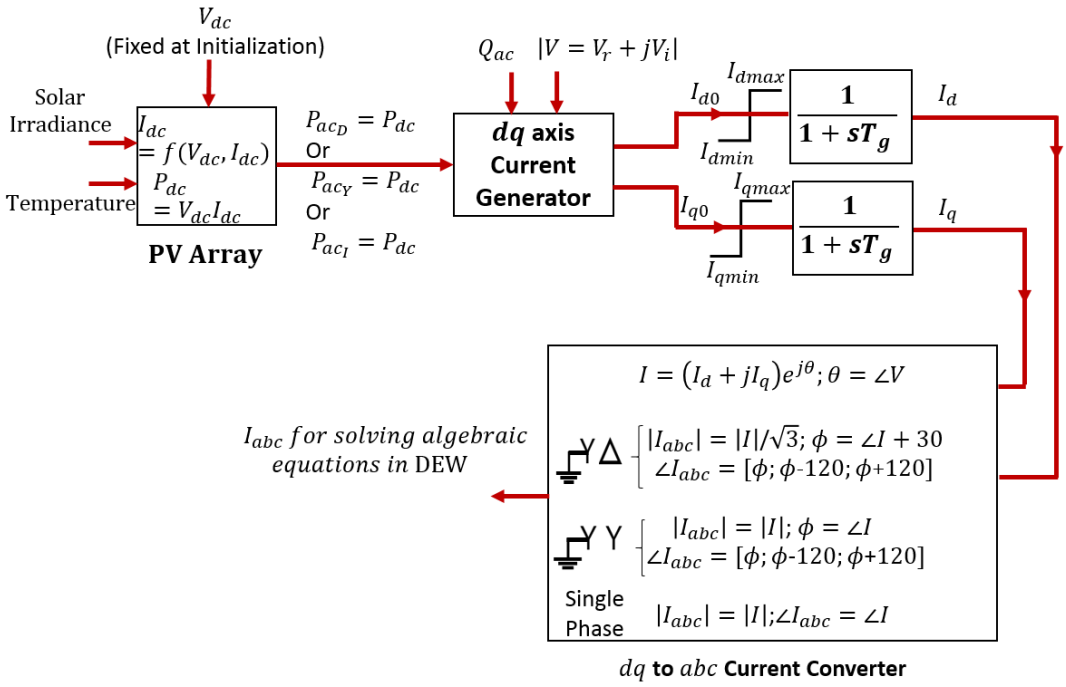

Fig. 18: Block Diagram of the D-PV Model during the Simulation

4.2.6 Initialization of the D-PV Model

The D-PV model is initialized using power flow analysis results. For initialization, the current source representing the solar PV unit is assigned balanced three phase currents such that it injects the desired average real and reactive powers at the PCC. The power flow is solved using this representation of the solar PV unit and, the positive sequence voltages and currents so obtained at the PCC are passed on to the D-PV model. The initialization function for the D-PV model calculates the dc voltage at the terminals of the solar panel array according to the real power injected at the PCC (plus transformer real power losses if considered) by solving the nonlinear solar panel array equations. As discussed earlier, the dc voltage is kept fixed for the duration of the simulation. The initialization function also calculates the initial states of the two first order transfer functions shown in Fig. 18.

4.3 Concluding Remarks

This chapter presented a dynamic model that can be used to model small solar PV units in dynamic simulation studies. The various assumptions made while developing the model and the justification for these assumptions was also provided. The D-PV model is capable of interfacing with unbalanced networks, and can control the generation of real and reactive powers. With the inclusion of the nonlinear model of solar panel arrays, the D-PV model is also capable of simulating the variation in real power output of solar PV units according to the incident solar irradiation.

The verification of the D-PV will be presented in the next chapter while the solar PV impact assessment studies performed using the model will be discussed in Chapter 6.

CHAPTER 5: VERIFICATION STUDIES FOR TPDA AND THE D-PV MODEL

5.1 Introduction

In chapters 3 and 4 the theoretical and logical foundations for TPDA and the D-PV model were presented. Since the objective of developing the TPDA program and the D-PV model is to study the dynamics of power systems using integrated T&D models, and evaluate the impact of distribution connected solar PV units on the dynamics of power systems using such network models, it is important that their performance be verified with programs that are widely used in the power systems industry. To this end, verification studies were performed using GE-PSLF® v16 (PSLF®), the Alternate Transients Program (ATP) windows version 5.9p4, and Matlab® versions R2014 and R2015. The results of these studies are discussed in detail in this chapter.

In the first part of this chapter verification studies for TPDA are presented. These verifications were performed with PSLF® and ATP. Table 12 below summarizes the TPDA verification studies.

Table 12: TPDA Verification Studies

Case Study #	Network Topology	Disturbance	Initial Network State
1	IEEE 9 Bus	Three phase Fault	Balanced
2	IEEE 9 Bus	Unbalanced Step Load Change	Balanced
3	IEEE 39 Bus	Balanced Step Load Change	Balanced
4	IEEE 39 Bus	Unbalanced Step Load Change	Balanced
5	IEEE 39 Bus	No Disturbance	Unbalanced

The second part of the chapter presents the results of verification studies performed with Matlab and a published paper on the verification the D-PV model.

5.2 Verification of TPDA

The discussion for all the studies in this section will follow the same format. First, the objective of the case study will be presented. Next, the network topology will be described. Then, the dynamic models used in the verifications will be presented along with their parameters. This will

be followed by a brief discussion on the disturbance simulated. Finally, comparison of results between TPDA and the verification program will be presented (except for case study 5).

5.2.1 Case Study 1

Objective: The objective of this case study was to verify the performance of TPDA with PSLF® for a balanced disturbance. Since PSLF® is a widely used program for studying electromechanical transients, a good match between the results of PSLF® and TPDA would verify both TPDA and the dynamic models of equipment used in TPDA.

Network Topology: The network topology used in this case study was the 230 kV WSCC 9 bus system [48], which had three loads (constant impedance load model) and three generators. The network also had three generator transformers and six transmission lines, which were modeled using the pi model. The network parameters, including steady state load and generation, can be found in [48]. The one line diagram of the WSCC 9 bus system is shown in Fig. 19.

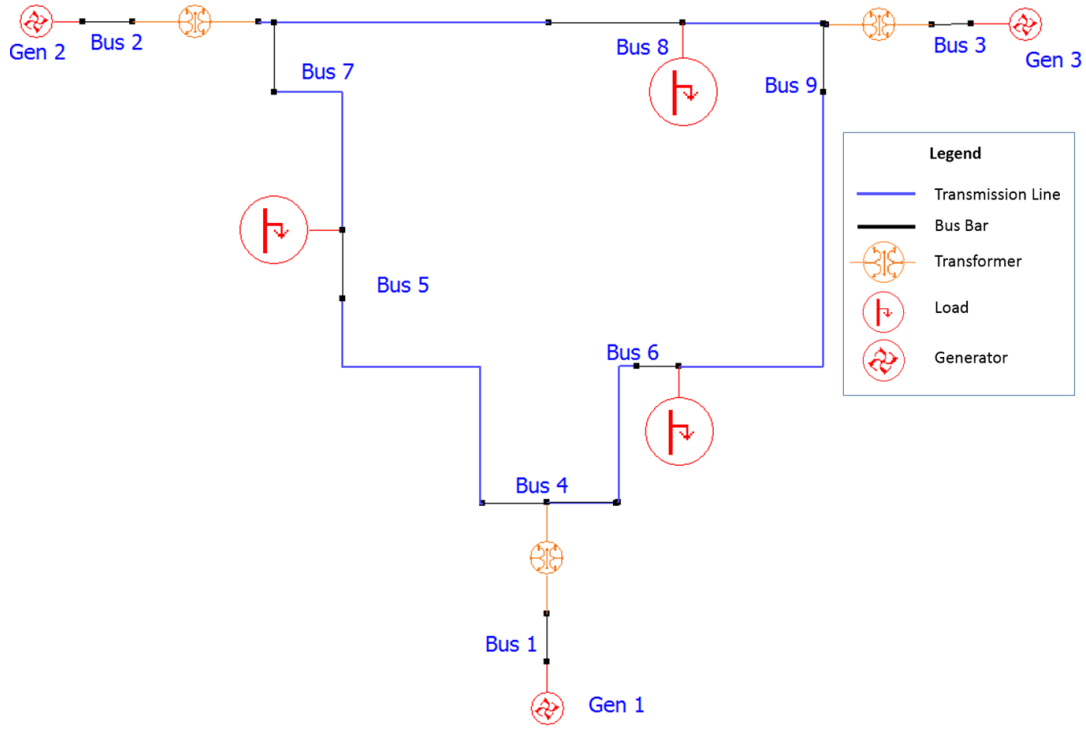

Fig. 19: One Line Diagram of the WSCC 9 Bus System built with DEW

Dynamic Equipment Models: The dynamic equipment models used in this case study are the standard dynamic models that are used for power systems dynamics studies. These models are summarized in Table 13. The models were developed in Matlab using the block diagrams given in [48], [56] and [74]. The parameters of the models are given in Tables 14-16.

Table 13: Dynamic Equipment Models used in TPDA Verification Case Study 1

Generator at Bus	Synchronous Generator	Generator Exciter	Generator Turbine/Governor
1	GENROU	GENROU	GENROU
2	ST1A	ST1A	ST1A
3	GGOV1	GGOV1	N/A

Table 14: GENROU Model Parameters used in TPDA Verification Case Studies 1 and 2 [53]. © 2015 IEEE

Parameters	Gen 1	Gen 2	Gen 3
$Rating$	90	190	110
$T'd0$	7.8	2.1	3
$T''d0$	0.021	0.04	0.047
$T'q0$	0.404	2.95	0.82
$T''q0$	0.06	0.15	0.07
H	8.4	1.38	6.01
D	0	0	0
Xd	2.1	2.32	1.137
Xq	1.88	2.15	0.95
$X'd$	0.25	0.245	0.146
$X'q$	0.27	0.4	0.48
$X''d$	0.01	0.0181	0.012
$X''q$	0.01	0.0181	0.012
Xl	0.0071	0.013	0.0078
$S(1.0)$	0.165	0.081	0.079
$S(1.2)$	0.414	0.271	0.265
Ra	0	0	0

Table 15: ST1A Exciter Model Parameters used in TPDA Verification Case Study 1 (Identical Parameters used for the Three Generators) [53]. © 2015 IEEE

Parameter	Value	Parameter	Value
tr	0.01	kc	0.065
$vimax$	0.1	kf	0
$vimin$	-0.1	tf	0
tc	1.5	$tc1$	0
tb	7.0	$tb1$	0
ka	140	klr	0
ta	0.008	$vamax$	99
$vrmax$	6.18	$vamin$	-99
$vrmin$	0.7	Ilr	99

Table 16: GGOV1 Turbine/Governor Parameters used in TPDA Verification Case Study 1 (Identical Parameters used for the Two Generators) [53]. © 2015 IEEE

Parameter	Gen 1	Gen 2	Parameter	Gen 1	Gen 2
$mwcap$	90	190	$Teng$	0	0
r	0.05	0.05	$Tfload$	3	3
$Rselect$	1	1	$Kpload$	4	4
$Tpelec$	0.5	0.1	$Kiload$	2	2
$Maxerr$	10	10	$Ldref$	1	1
$Minerr$	-10	-10	Dm	0	0
$Kpgov$	3	3	$ropen$	99	99
$Kigov$	0.55	0.55	$rclose$	-99	-99
$Kdgov$	0	0	$Kimw$	0	0
$Tdgov$	1	1	$Pmwset$	0	0
$Vmax$	1	1	$aset$	10	10
$Vmin$	0	0	Ka	10	10
$Tact$	0.15	0.15	Ta	0.1	0.1
$Kturb$	2.7	2.7	Db	0	0
$wfnl$	0.205	0.205	Tsa	1	1
Tb	2.5	2.5	Tsb	10	10
Tc	0.8	0.8	Rup	99	99
$Flag$	0	0	$Rdown$	-99	-99

Disturbance: The disturbance simulated to obtain the dynamic response of the system was a bolted, three phase to ground fault on the line between buses 4 and 5. The fault was located at 33% of line length from bus 5. The fault was initiated at 0.1 seconds and was removed after 10 cycles at 0.267 seconds [53].

Results: Rotor speed deviation from 60 Hz and voltage r.m.s values are used as the comparison variables in this, and the rest of the TPDA verification case studies (except for case study 5). Three metrics are used to compare the results of dynamic simulation with PSLF® for the two variables [17], [53]. These are:

1. **Plots of trajectories**: Plots of trajectories of rotor speed deviations and terminal voltages are used as visual aids for comparison of TPDA's performance with PSLF®. These plots help in quickly assessing the overall performance of TPDA; if the shapes of trajectories obtained from TPDA are similar to those obtained from PSLF®, it implies that TPDA correctly captured the evolution of power systems states.
2. **Correlation coefficients**: To quantify the degree of match in the shape of the trajectories of the comparison variables, a correlation coefficient is calculated as:

$$Correlation(\mathbf{x},\mathbf{y}) = \frac{\sum_{i=1}^{N}(x_i - \bar{x})(y_i - \bar{y})}{\sqrt{\sum_{i=1}^{N}(x_i - \bar{x})^2 \sum_{i=1}^{N}(y_i - \bar{y})^2}}$$

,where, **x** and **y** are the data vectors whose correlation coefficient is to be determined; x_i and y_i are the i^{th} elements of vectors **x** and **y**; $\bar{x}$ and $\bar{y}$ are the means of vectors **x** and **y**.

3. **Root Mean Square Errors** (RMSEs): To quantify the degree of match in values of the comparison variables, an RMSE is calculated as:

$$RMSE(\mathbf{x},\mathbf{y}) = \sqrt{\frac{\sum_{i=1}^{N}(x_i - y_i)^2}{N}}$$

Figures 20 and 21 show the plots of rotor speed deviations and generator terminal voltages, respectively. Tables 17 and 18 list the correlation coefficients and RMSEs for the two variables.

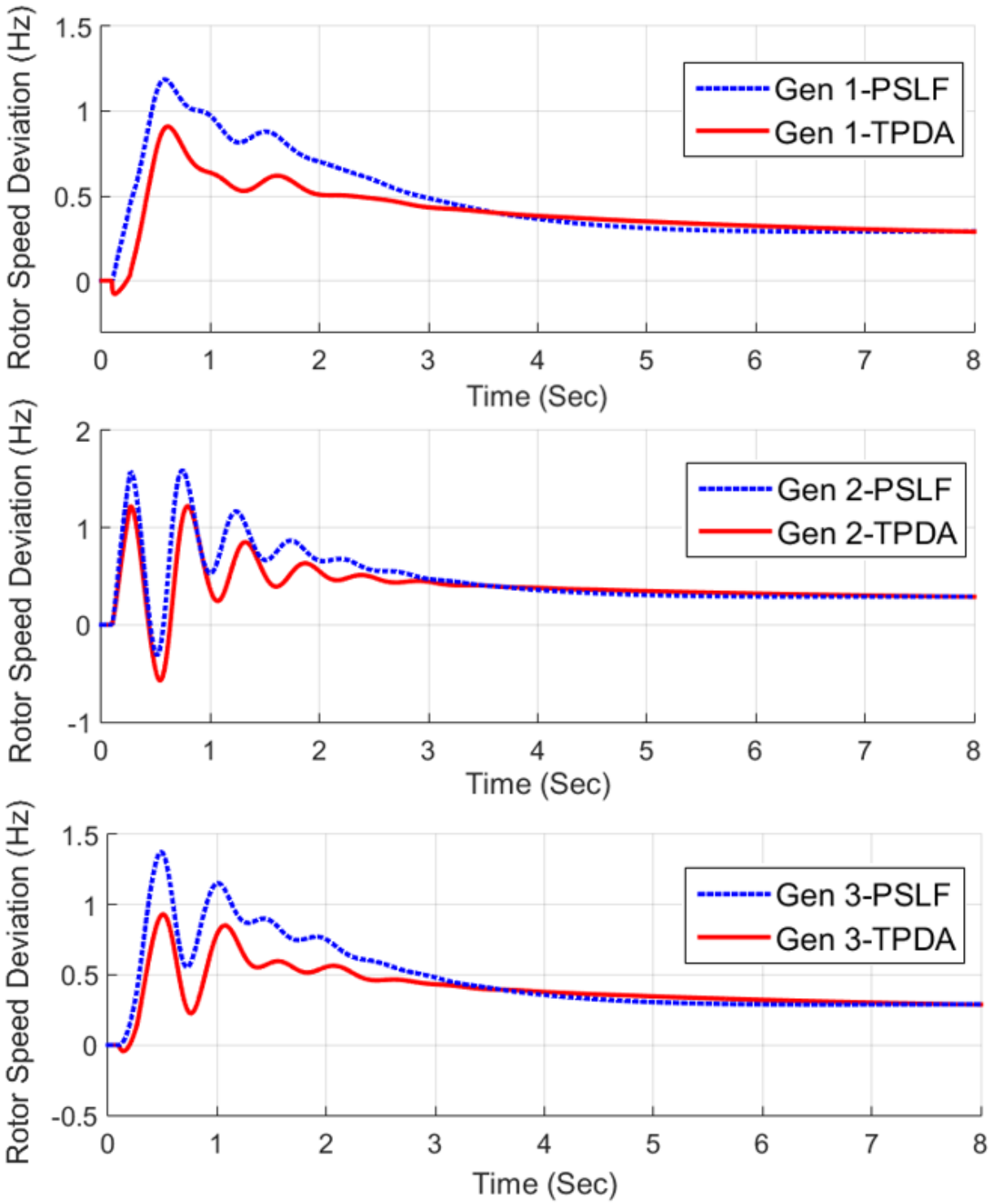

Fig. 20: Rotor Speed Deviations (Hz) in TPDA Verification Case Study 1

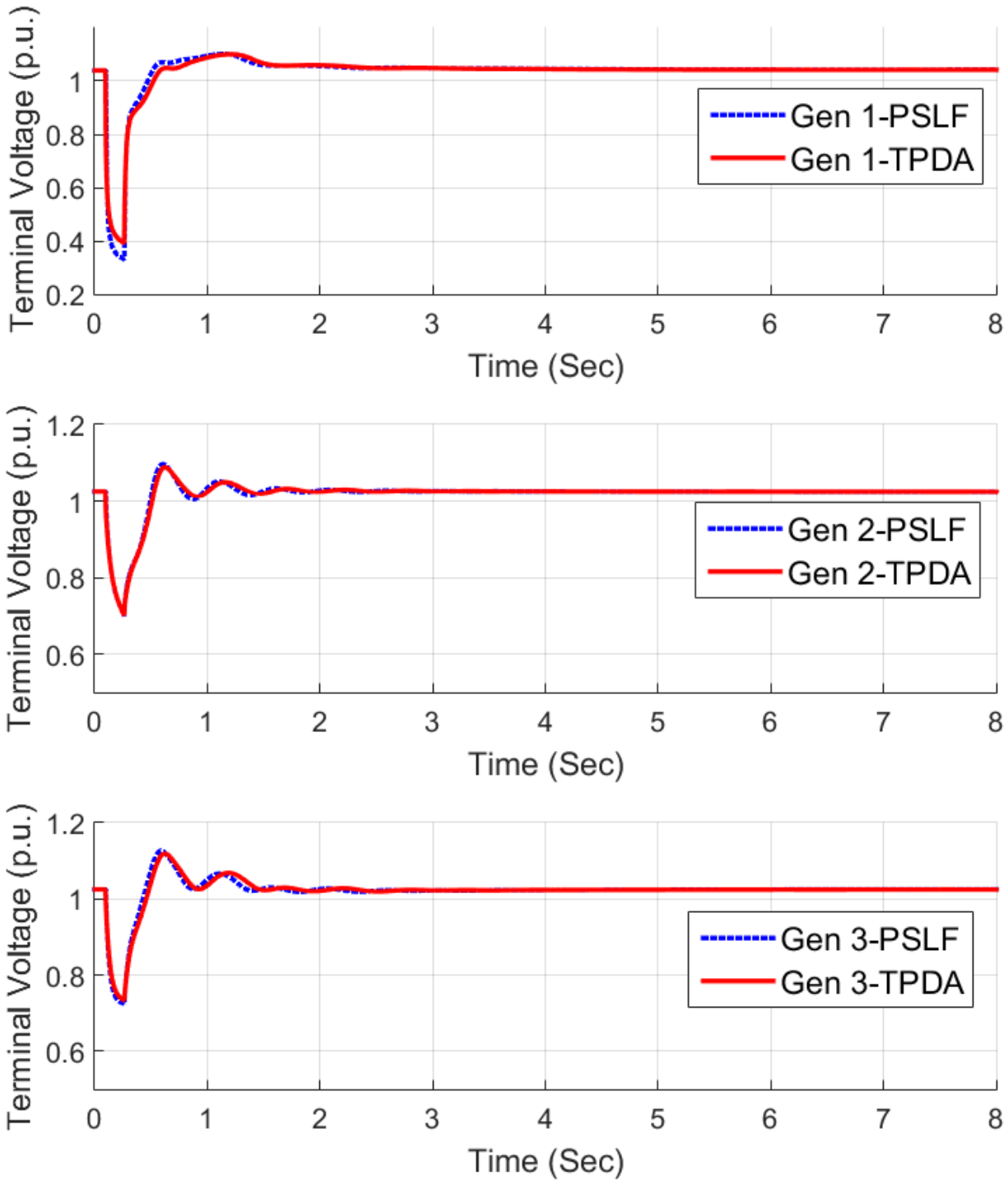

Fig. 21: Generator Terminal Voltages (p.u.) in TPDA Verification Case Study 1

Table 17: Correlation Coefficients of Rotor Speeds and Generator Terminal Voltages in TPDA Verification Case Study 1

Generator	Rotor Speed	Terminal Voltage
Gen 1	91.2%	98.4%
Gen 2	88.5%	99.7%
Gen 3	92.7%	99.4%

Table 18: RMSEs of Rotor Speeds and Generator Terminal Voltages in TPDA Verification Case Study 1

Generator	Rotor Speed (Hz)	Terminal Voltage (p.u. X 100%)
Gen 1	0.143	2.23%
Gen 2	0.164	0.45%
Gen 3	0.149	0.61%

Figures 20 and 21 and tables 17 and 18 show that the rotor speed and generator terminal voltage trajectories match well between TPDA and PSLF®. The correlation coefficients of the two variables are close to unity and the RMSEs are small. These observations suggest that TPDA was able to correctly simulate the dynamics of the WSCC system during the given fault.

It should also be noted that the models were initialized correctly as the rotor speeds and generator terminal voltages stay at their initial values till the disturbance is initiated. This verifies the initialization procedure of TPDA for balanced networks that was discussed in Chapter 3.

5.2.2 Case Study 2

Objective: The objective of this case study was to verify the performance of TPDA for an unbalanced disturbance. Since ATP can simulate multi-phase networks and does not require the network to be balanced, it was used to verify the performance of TPDA against an unbalanced disturbance.

Network Topology: The network topology of case study 1 was used in this case study.

Dynamic Equipment Models: The GENROU model of a synchronous generator with the parameters given in Table 14 was used in the case study. The exciter and governor models were not used. Since an unbalanced disturbance was simulated, the zero sequence impedance was also used. Its value was the same as the value of Xl in Table 14.

Disturbance: The unbalanced disturbance was simulated by suddenly increasing Phase A load on buses 5 and 6, by 90 MW and 75 MW, respectively, at 0.5 seconds and then suddenly restoring the original load at 1 second. The load increase at 0.5 seconds corresponds to 214% and 250% increase in the initial phase A load on buses 5 and 6, respectively.

Results: Similar to case study 1, rotor speeds and voltages were used to verify TPDA with ATP in this case study. Since ATP generates sinusoidal waveforms for voltages, the r.m.s value of the nominal frequency component of the waveform was extracted to perform the comparison with TPDA. Fig. 22 shows the rotor speeds of the three generators and Table 19 lists the rotor speed correlation coefficients and RMSEs for the three generators. The three phase voltages at buses 5, 6 and 8 are shown in Fig. 23-25 (per unitized based on the initial bus voltages). Table 20 shows the correlation coefficients, while Table 21 shows the RMSEs for three phase voltages at the terminals of the three generators and buses 5, 6 and 8.

Table 19: Correlation Coefficients and RMSEs of Rotor Speeds in TPDA Verification Case Study 2

Generator	Correlation Coefficients	RMSEs (Hz)
Gen 1	99.7%	0.054
Gen 2	99.7%	0.054
Gen 3	99.7%	0.051

Table 20: Correlation Coefficients of Voltages in TPDA Verification Case Study 2

Generator	Phase A	Phase B	Phase C	Average
Bus 5	96.1%	95.7%	89.3%	93.70%
Bus 6	95.8%	96.7%	87.7%	93.40%
Bus 8	88.6%	95.7%	93.4%	92.57%
Gen 1	82.9%	96.2%	84.2%	87.77%
Gen 2	83.7%	93.6%	94.6%	90.63%
Gen 3	66.1%	97.9%	88.4%	84.13%

Table 21: RMSEs of Voltages in TPDA Verification Case Study 2

Generator	Phase A (p.u. X 100%)	Phase B (p.u. X 100%)	Phase C (p.u. X 100%)	Average (p.u. X 100%)
Bus 5	1.66%	1.71%	1.32%	1.56%
Bus 6	1.74%	1.63%	1.39%	1.59%
Bus 8	1.57%	0.89%	0.98%	1.15%
Gen 1	1.97%	2.64%	1.82%	2.14%
Gen 2	1.51%	0.98%	0.92%	1.14%
Gen 3	1.99%	0.65%	1.17%	1.27%

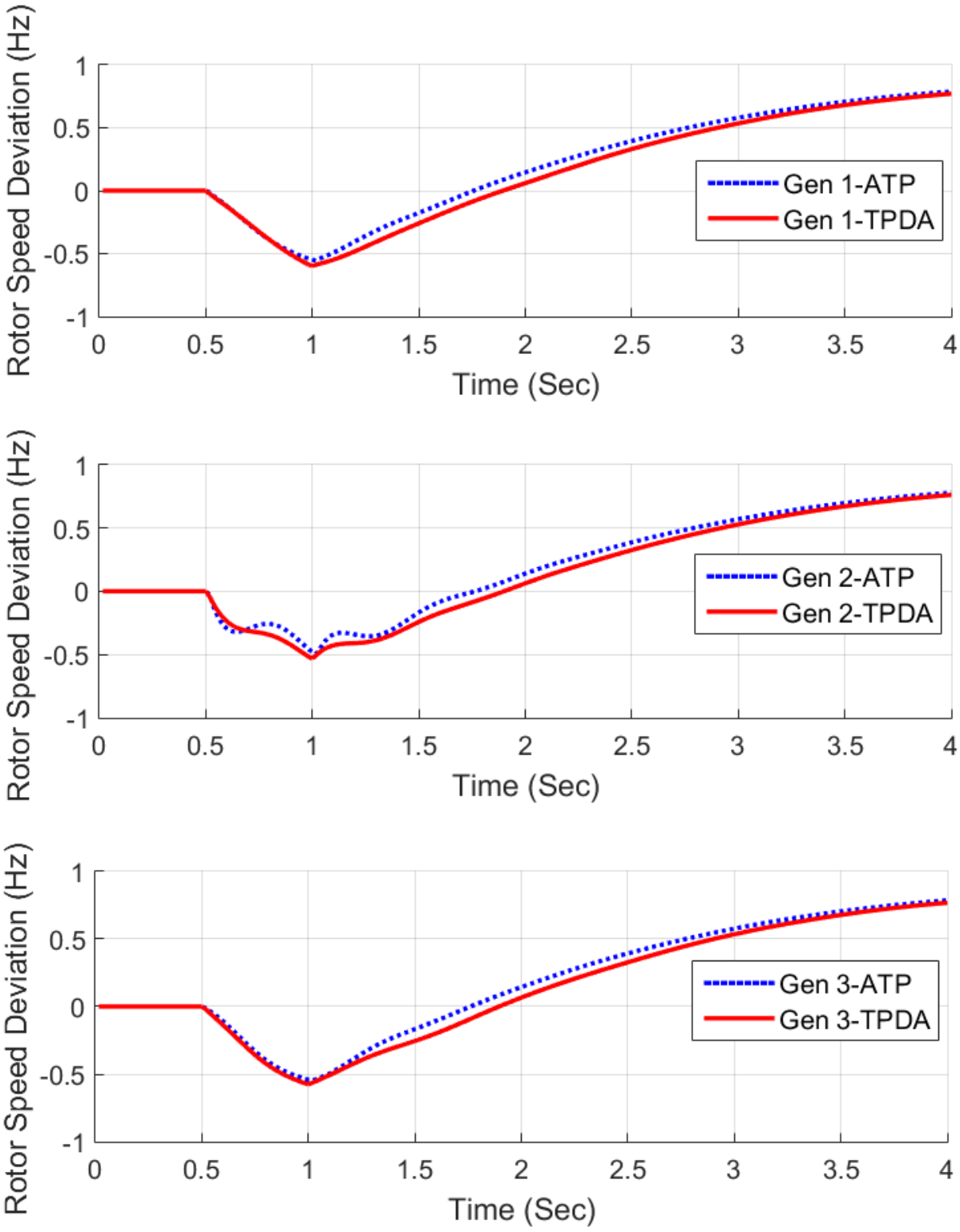

Fig. 22: Rotor Speed Deviations (Hz) in TPDA Verification Case Study 2

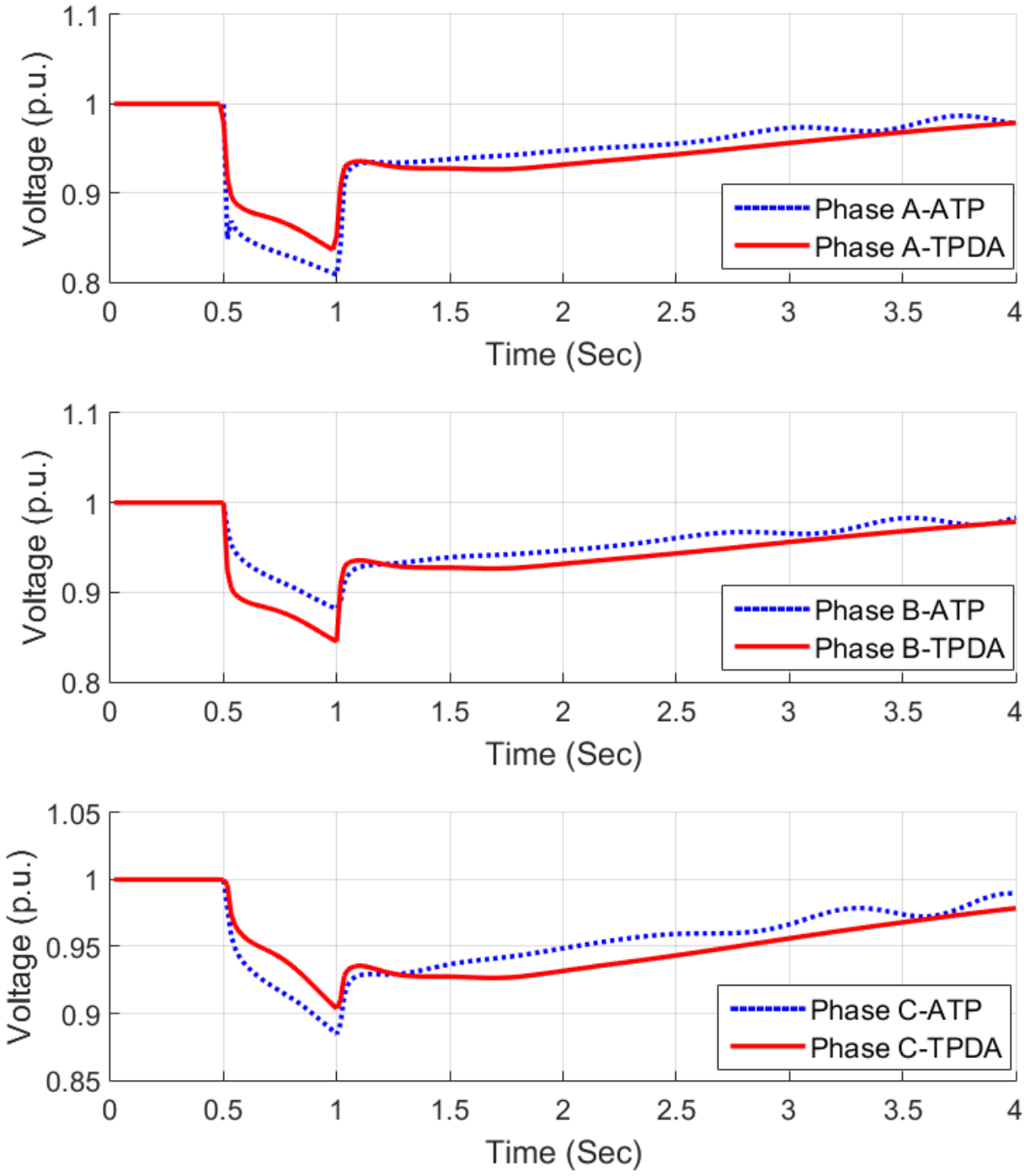

Fig. 23: Three Phase Voltages at Bus 5 in TPDA Verification Case Study 2

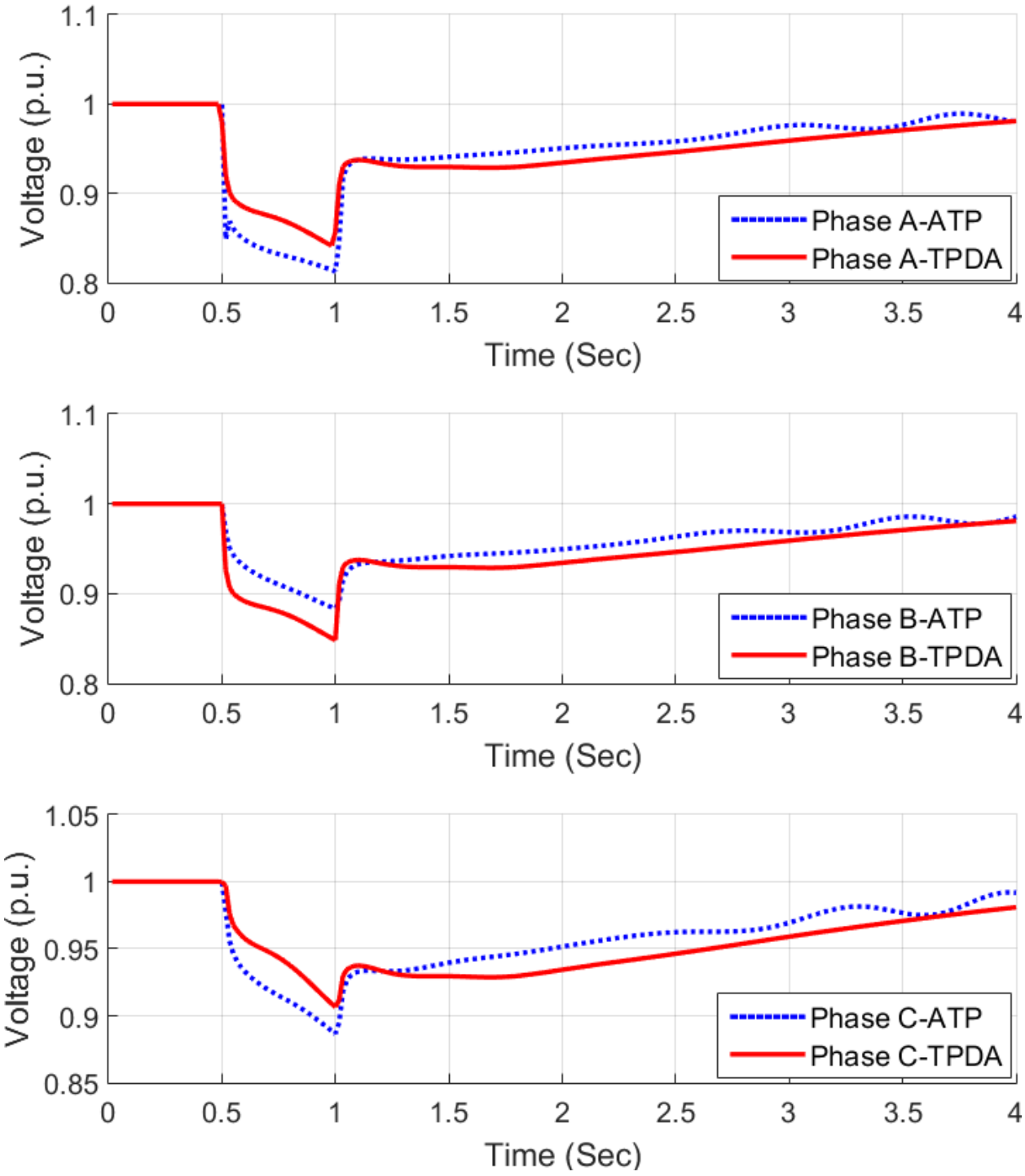

Fig. 24: Three Phase Voltages at Bus 6 in TPDA Verification Case Study 2

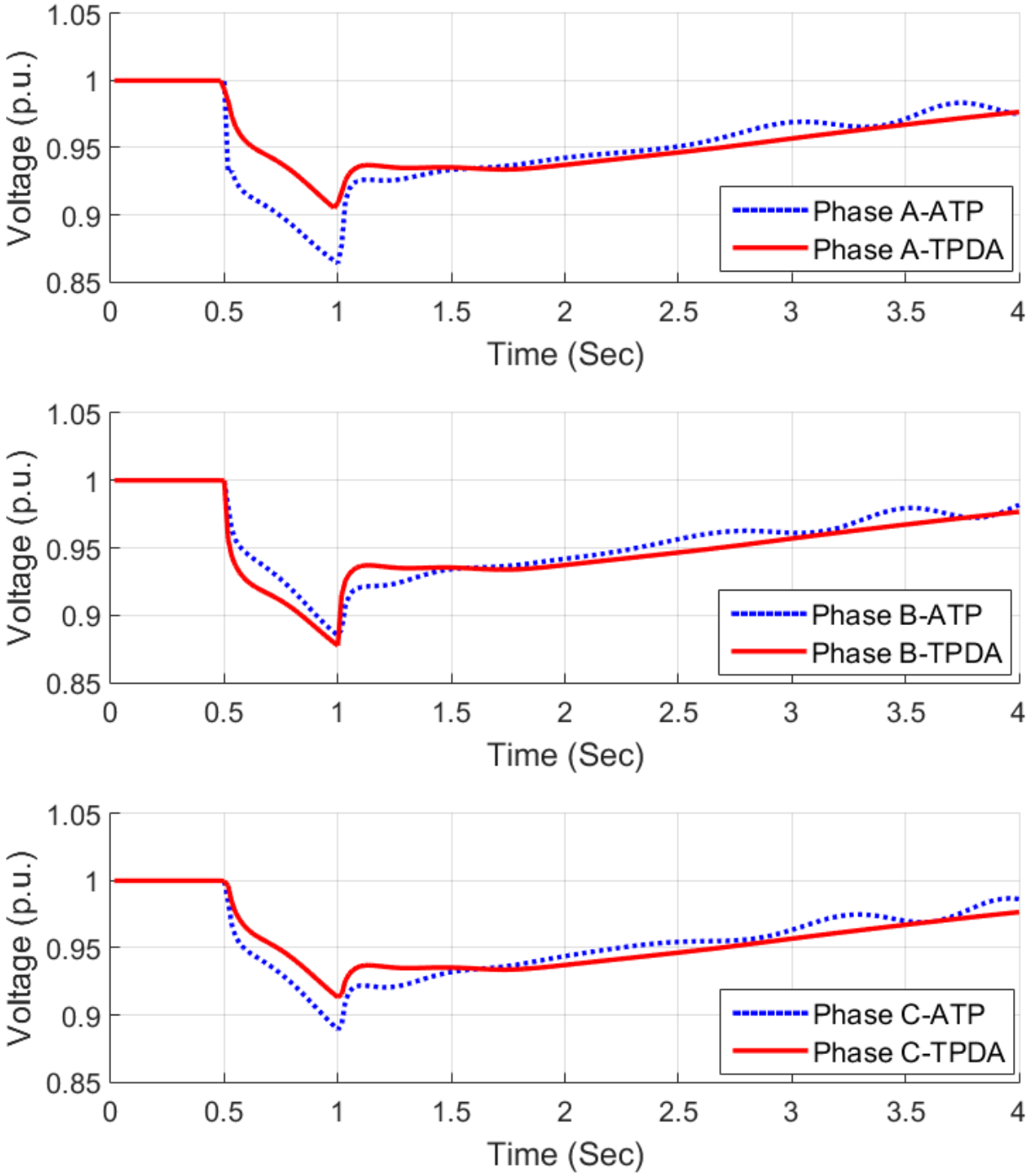

Fig. 25: Three Phase Voltages at Bus 8 for TPDA Verification Case Study 2

Above tables and figures show that TPDA was able to simulate unbalanced disturbances accurately, as the dynamic simulation results under the unbalanced loading match well with ATP.

5.2.3 Case Study 3

Objective: The objective of this case study was to verify the performance of TPDA with PSLF® for a larger system than that used in case studies 1 and 2. The approach for performing the analysis and verifying the results was similar to the one adopted in case study 1.

Network Topology: The network used in this case study was the IEEE 39 bus system. The parameters of this model can be found [49]. Constant impedance load model was assumed for all the loads in the network. The one line diagram of the IEEE 39 bus system as drawn in DEW is shown in Fig. 26. Bus numbers are marked by numerals in Fig. 26.

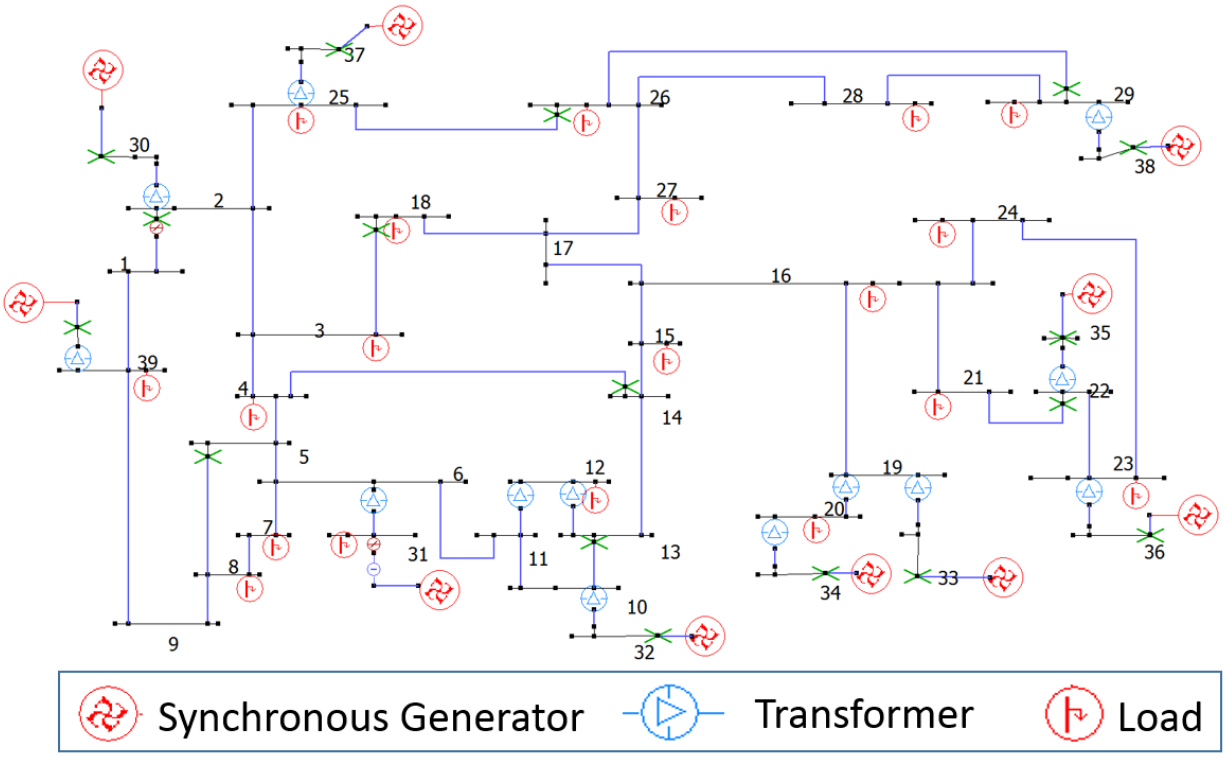

Fig. 26: One Line Diagram of the IEEE 39 Bus System built with DEW

Dynamic Equipment Models: The GENROU model of synchronous generator with the parameters given in Table 22 was used in the case study. Exciters and turbine/governors were not modeled.

Table 22: GENROU Model Parameters for Case Studies 3 and 4

Parameters	Gen 30	Gen 31	Gen 32	Gen 33	Gen 34
$Rating\ (MW)$	400	700	700	700	600
$T'd0$	6.7	7.8	8.69	8.4	8.3
$T''d0$	0.38	0.021	0.3793	1.36	0.4867
$T'q0$	2.5	1.604	1.5	0.44	0.7
$T''q0$	0.25	0.06	0.25	0.0733	0.0667
H	35.8	24	28.6	26	34.8
D	0	0	0	0	0
Xd	0.2495	2.1	0.262	0.67	0.254
Xq	0.237	1.8	0.258	0.62	0.241
$X'd$	0.0531	0.25	0.0436	0.132	0.05
$X'q$	0.0876	0.27	0.166	0.166	0.0814
$X''d$	0.00425	0.01	0.00349	0.0106	0.004
$X''q$	0.00425	0.01	0.00349	0.0106	0.004
Xl	0.00304	0.0171	0.00295	0.0054	0.00224
$S(1.0)$	0.081	0.165	0.081	0.081	0.081
$S(1.2)$	0.271	0.414	0.271	0.271	0.271
Ra	0	0	0	0	0
$rcomp$	0	0	0	0	0
$xcomp$	0	0	0	0	0
Parameters	Gen 35	Gen 36	Gen 37	Gen 38	Gen 39
$Rating\ (MW)$	700	600	600	800	1500
$T'd0$	8.66	8.0	4.79	8.79	10.2
$T''d0$	0.3773	0.4467	0.3193	0.68	0.08
$T'q0$	1.5	2.0	3.96	3.96	1.0
$T''q0$	0.25	0.0683	0.3267	0.33	0.03
H	26.4	24.3	34.5	34.5	42
D	0	0	0	0	0
Xd	0.295	0.29	0.2106	0.2106	0.1
Xq	0.292	0.28	0.205	0.205	0.069
$X'd$	0.049	0.057	0.057	0.057	0.031
$X'q$	0.186	0.0911	0.0587	0.0587	0.021
$X''d$	0.00392	0.00456	0.00456	0.00248	0.0011
$X''q$	0.00392	0.00456	0.00456	0.00248	0.0011
Xl	0.00322	0.0028	0.00298	0.00125	0.0008
$S(1.0)$	0.081	0.081	0.081	0.081	0.081
$S(1.2)$	0.271	0.271	0.271	0.271	0.271
Ra	0	0	0	0	0
$rcomp$	0	0	0	0	0
$xcomp$	0	0	0	0	0

Disturbance: 1,500 MW and 552 MVAR balanced load increase at Bus 4 was simulated to compare the dynamic response of TPDA with ATP [17]. The increase was 300% of the original nominal load (load at 1.0 p.u. voltage) at the bus. The disturbance was initiated at the end of 0.1 second and removed at the end of 0.3 second.

Results: Plots of rotor speed deviations and voltages, and the correlation coefficients and RMSEs between TPDA and PSLF® for these variables were used to verify the performance of TPDA. The verification results are shown in Fig. 27 and Fig. 28 and Table 23.

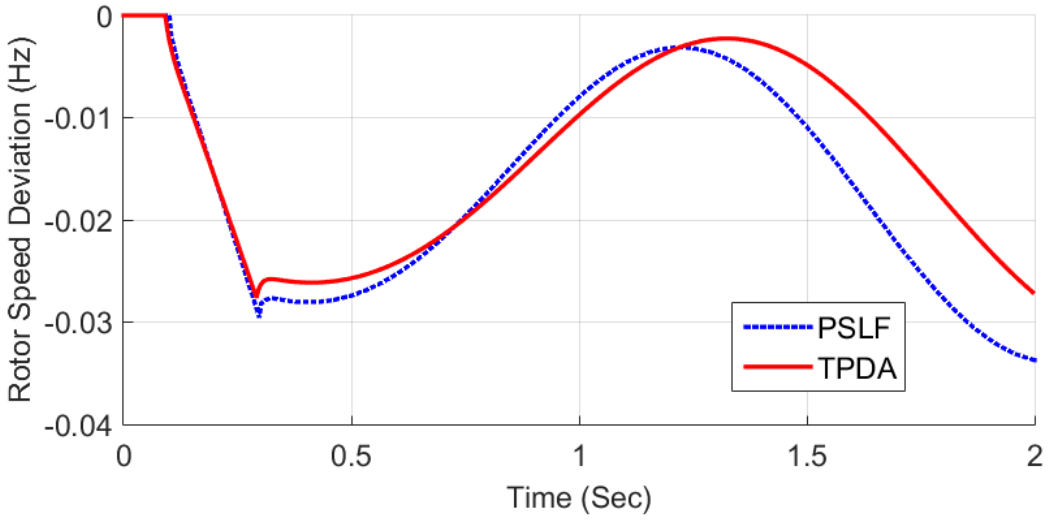

Fig. 27: Rotor Speed Deviation of Generator at Bus 31 in TPDA Verification Case Study 3

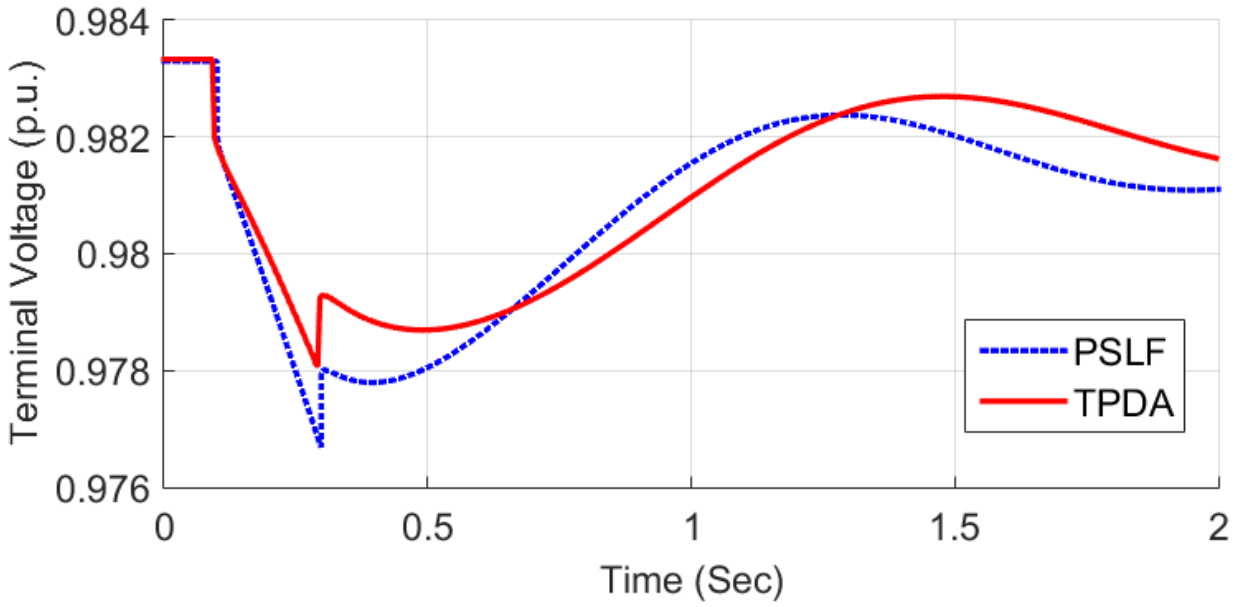

Fig. 28: Terminal Voltage of Generator at Bus 32 in TPDA Verification Case Study 3

Table 23: Rotor Speed Deviation and Voltage Correlation Coefficients and RMSEs between TPDA and PSLF® in TPDA Verification Case Study 3 [17]. © 2016 IEEE

Generator Bus #	Correlation Coefficients		Root Mean Square Error	
	Rotor Speed	Voltage	Rotor Speed (Hz)	Voltage (p.u. X 100%)
30	97%	99%	0.002	0.04%
31	92%	98%	0.005	0.26%
32	96%	94%	0.006	0.07%
33	98%	99%	0.002	0.03%
34	99%	81%	0.002	0.03%
35	99%	99%	0.002	0.04%
36	98%	95%	0.002	0.04%
37	92%	98%	0.003	0.04%
38	97%	96%	0.002	0.03%
39	98%	98%	0.002	0.03%

5.2.4 Case Study 4

Objective: The objective of this case study was to verify the performance of TPDA under unbalanced disturbances with a larger network. Similar to case study 2, ATP was used as the verification software.

Network Topology: The network topology of case study 3 was used in this case study.

Dynamic Equipment Models: The GENROU model of synchronous generator with the parameters given in Table 22 was used in the case study. Exciters and turbine/governors were not modeled.

Disturbance: The load on phase A of bus 12 was increased by 280 MW and 2,870 MVAR [17], while the load on phases B and C was not changed, to simulate the unbalanced disturbance. The increase was about 99 times the original nominal phase A load (load at 1.0 p.u. voltage) of the bus. The disturbance was initiated at the end of 0.1 second and removed at the end of 0.3 seconds.

Results: Plots of rotor speed deviations and voltages, and the correlation coefficients and RMSEs between TPDA and ATP for these variables were used to verify the performance of TPDA. Some of the verification results are shown in figures 29 and 30 and tables 24 and 25.

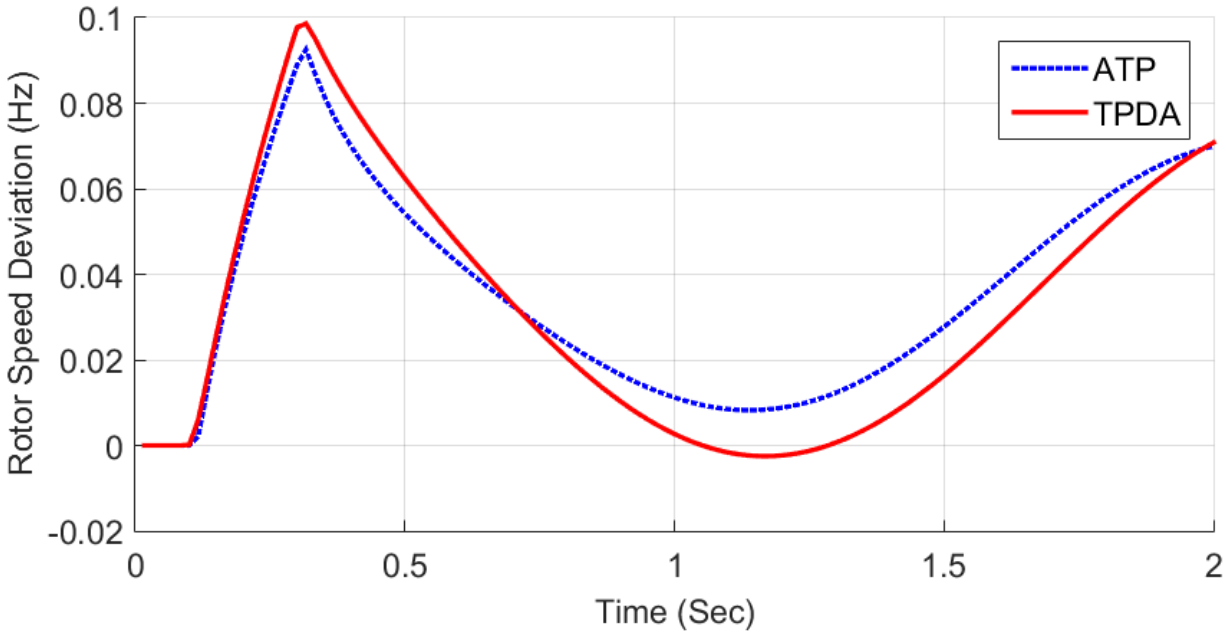

Fig. 29: Rotor Speed Deviation of Generator at Bus 31 in TPDA Verification Case Study 4

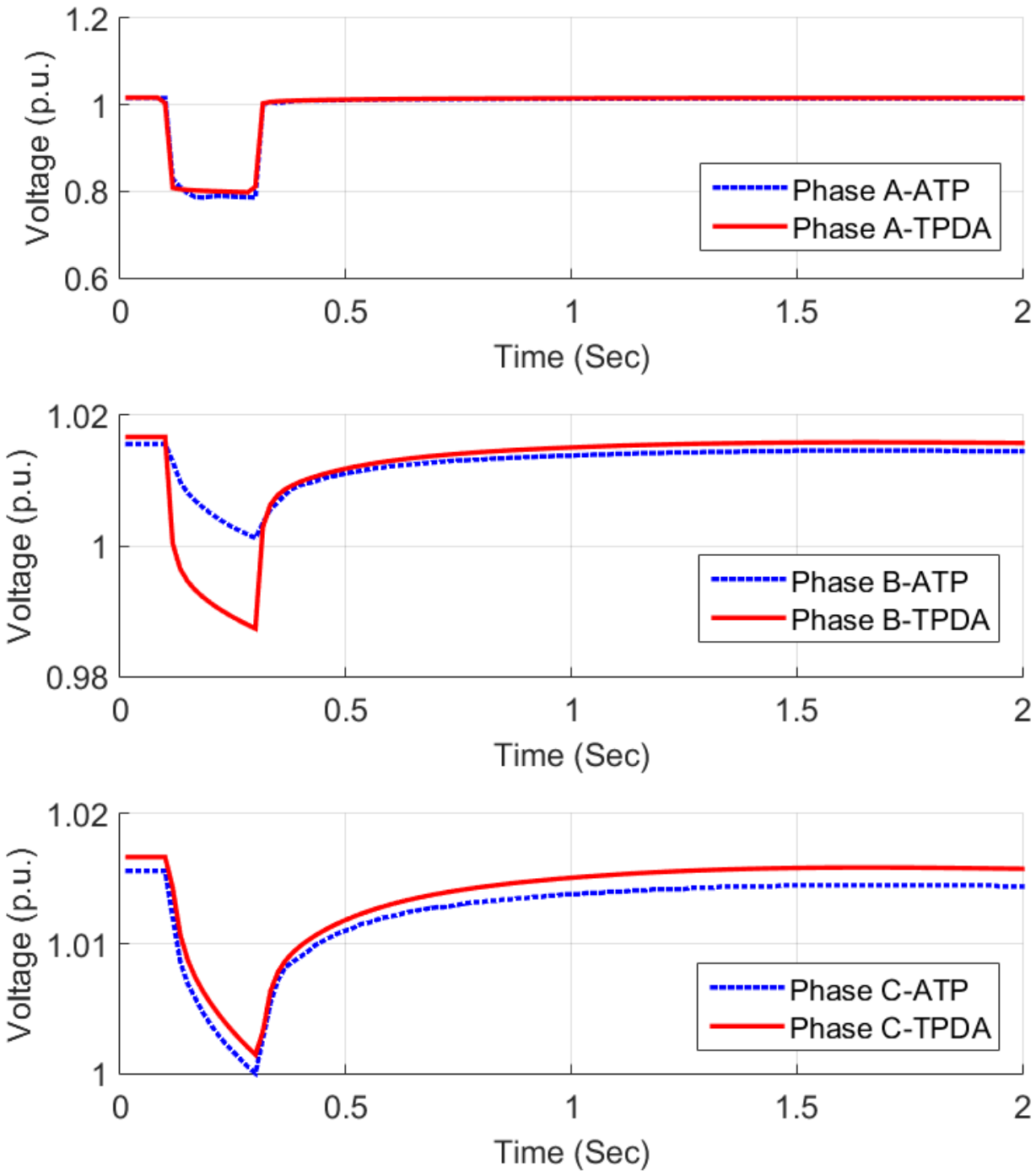

Fig. 30: Three Phase Voltage at Bus 11 in TPDA Verification Case Study 4

Table 24: Correlation Coefficients and RMSEs of Rotor Speed Deviation between TPDA and ATP in TPDA Verification Case Study 4 [17]. © 2016 IEEE

Generator Bus #	Correlation Coefficients	Root Mean Square Error (Hz)
30	99%	0.0003
31	98%	0.0013
32	95%	0.0015
33	98%	0.0004
34	98%	0.0005
35	99%	0.0003
36	99%	0.0003
37	98%	0.0004
38	97%	0.0007
39	99%	0.0004

Table 25: Correlation Coefficients and RMSEs of Bus 11 Voltages between TPDA and ATP in TPDA Verification Case Study 4

	Correlation Coefficients	Root Mean Square Error (p.u. X 100%)
Phase A	100%	0.47%
Phase B	92%	0.44%
Phase C	100%	0.13%

Results of case studies 3 and 4 show that TPDA was able to simulate the dynamics the of power system accurately for the IEEE 39 bus system for both balanced and unbalanced disturbances. These case studies corroborate with the verification of TPDA that was performed in case studies 1 and 2.

5.2.5 Case Study 5

Objective: The objective of the case study was to show that when the network is unbalanced from the start of the simulation, the initialization approach discussed in chapter 3 results in the system being practically at the steady state right from the start.

Network: The IEEE 39 bus network topology of case studies 3 and 4 was used. The unbalance was simulated by decreasing all phase B loads by 4% and increasing all phase C loads by 4%. As before, a constant impedance load model was assumed.

Dynamic Equipment Models: The GENROU model for generators, the ST1A model for exciters and the TGOV1 model for turbine/governors, were used. The parameters of the generator and exciter models were the same as shown in Tables 22 and 15, respectively. The exciter parameter ta in Table 15 was 0.02 in this case study for all the generator exciters. The turbine/governor parameters are shown in Table 26 (governor ratings were kept the same as the generator ratings shown in Table 22).

Table 26: Parameters for the TGOV1 Turbine/Governor Model used in TPDA Verification Case Study 5

Parameter	Value
r	0.05
$T1$	0.5
$vmax$	1
$vmin$	0
$T2$	0.3
$T3$	1
Dt	0

Disturbance: No disturbance was created in this case study as the objective was to check the validity of the initialization procedure for unbalanced networks.

Results: The plots of rotor speeds (Fig. 31), and the terminal voltage of the generator at bus 38 (Fig. 32) below show that the stable steady state is present practically from the start. The maximum deviation of rotor speed from the nominal frequency (60 Hz) is less than 0.001 Hz, or 0.0017%, implying that the steady state is practically present from the start. Similarly, the maximum deviation of the terminal voltages of generator at bus 38 from their initial values is around 0.02%,

while the final steady state voltages are around 0.01% different from their initial values. Table 27 summarizes the maximum and steady state generator terminal voltage deviations from the initial power flow calculated voltages. The table shows that all the generator voltages are practically at steady state from the start of the simulation.

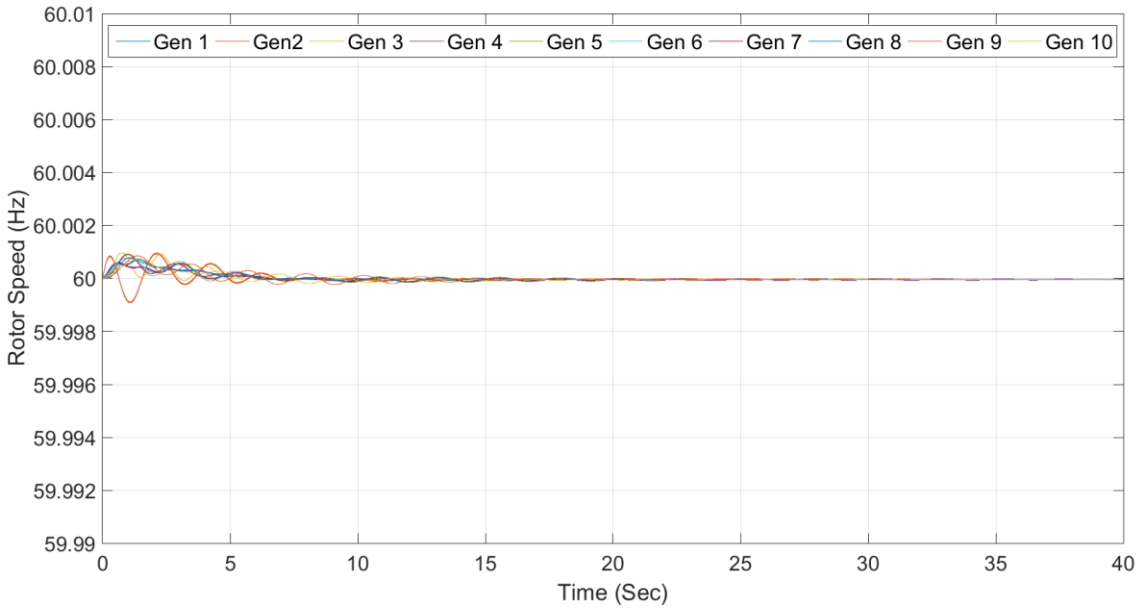

Fig. 31: Rotor Speeds of all the Generators in TPDA Verification Case Study 5

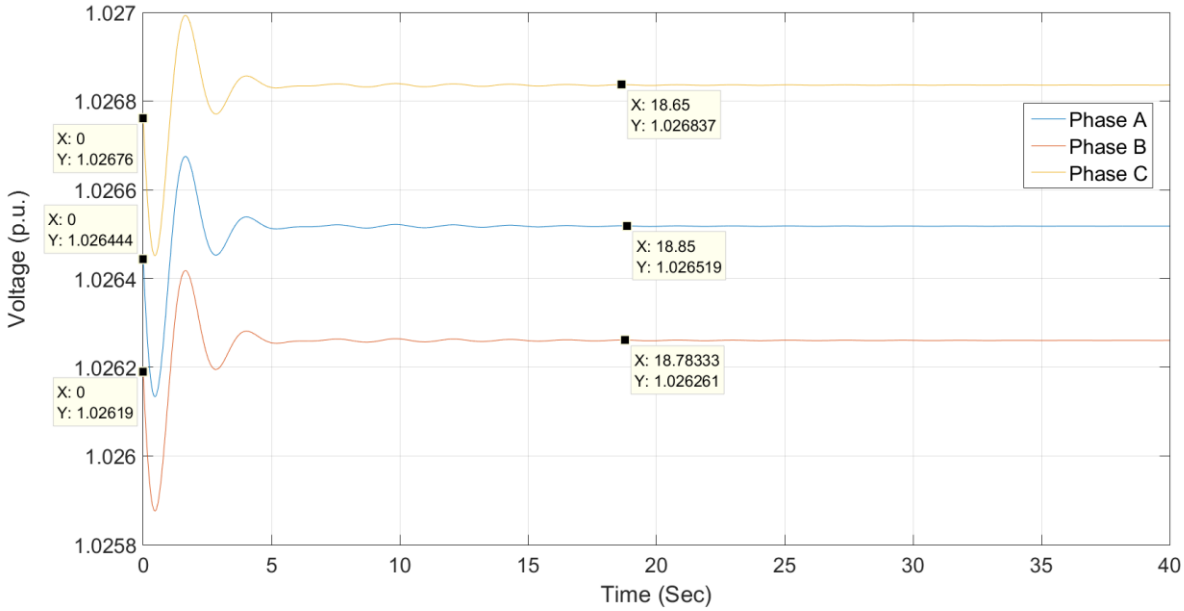

Fig. 32: Terminal Voltage at Generator Bus 38 in TPDA Verification Case Study 5

Table 27: Maximum and Steady State Voltage Deviations from Initial Voltages in TPDA Verification Case Study 5

	Maximum Deviation			Steady State Deviation		
Generator Bus #	Phase A (%)	Phase B (%)	Phase C (%)	Phase A (%)	Phase B (%)	Phase C (%)
30	0.03	0.03	0.03	0.02	0.02	0.02
31	0.09	0.09	0.09	0.09	0.09	0.08
32	0.02	0.02	0.02	0.01	0.01	0.01
33	0.02	0.03	0.02	0.01	0.02	0.01
34	0.03	0.03	0.03	0.01	0.01	0.02
35	0.02	0.02	0.02	0.01	0.01	0.01
36	0.02	0.02	0.02	0.01	0.01	0.01
37	0.03	0.03	0.03	0.01	0.01	0.01
38	0.02	0.02	0.02	0.01	0.01	0.01
39	0.01	0.01	0.01	0.01	0.01	0.01

5.3 Verification of the D-PV Model

This section presents two studies that were performed to verify the D-PV model that was developed in Chapter 4. The first study verifies the ability of the D-PV model to change its output based on the incident solar irradiation by comparing its output with a Simulink based detailed pulse width modulation (PWM) controlled inverter model. The second study verifies the control algorithm of the D-PV model when it is interfaced with unbalanced networks.

5.4 Verification of the D-PV Model under Solar Transients

Two tests were performed in this study to verify the accuracy of the D-PV model while simulating solar transients. The verifications were performed against the detailed Simulink model of a solar PV unit that included a PWM controlled inverter model [75]. The network topology used for the test is given in Fig. 33. The Maximum Power Point Tracking (MPPT) module of the Simulink solar PV model was disabled for the test as the D-PV model does not include a MPPT module. Network parameters used in the tests are given in Table 28, while the parameters required to model the solar panel can be found in the Simulink model of [75]. In both the tests, the solar PV unit was injecting 240 kW at the start of the simulations.

Table 28: Network Parameters for the Verification of the D-PV Model under Solar Transients

Component Name	R (ohms)	X (ohms)
T1: 0.25-4.16 kV	0.0	0.0
Line 1	0.0	0.07775
Line 2	0.0	0.05007
T2: 4.16-12.47 kV	0.08653 (4.16 kV side)	0.51917 (4.16 kV side)
Line 3	0.0	0.1555

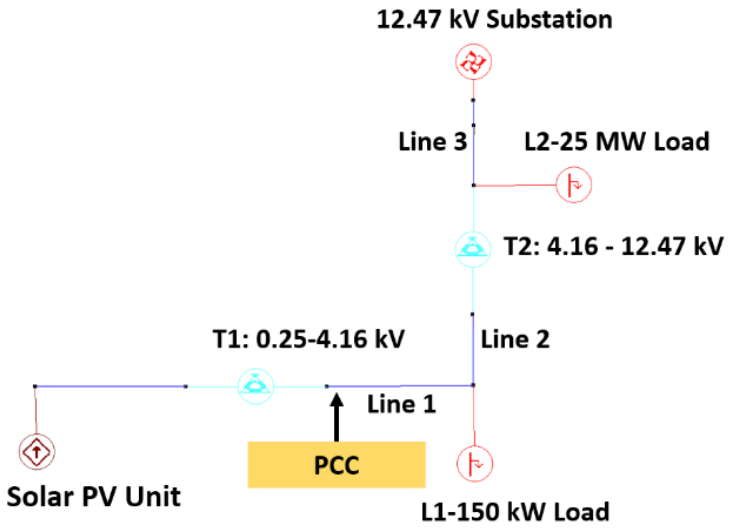

Fig. 33: Network Topology used for Verification of the D-PV Model under Solar Transients

5.4.1 Test 1

In the first test, loads L1 and L2 were fixed at the values shown in Fig. 33. The solar transient and the resulting currents injected on the low voltage side of transformer T1 by the D-PV and Simulink models are shown in Fig. 34, which shows that the current profiles generated by TPDA and Simulink match closely. The near transient free current waveform from Simulink also verifies the assumption made in the D-PV model about the high bandwidth of inverter controllers.

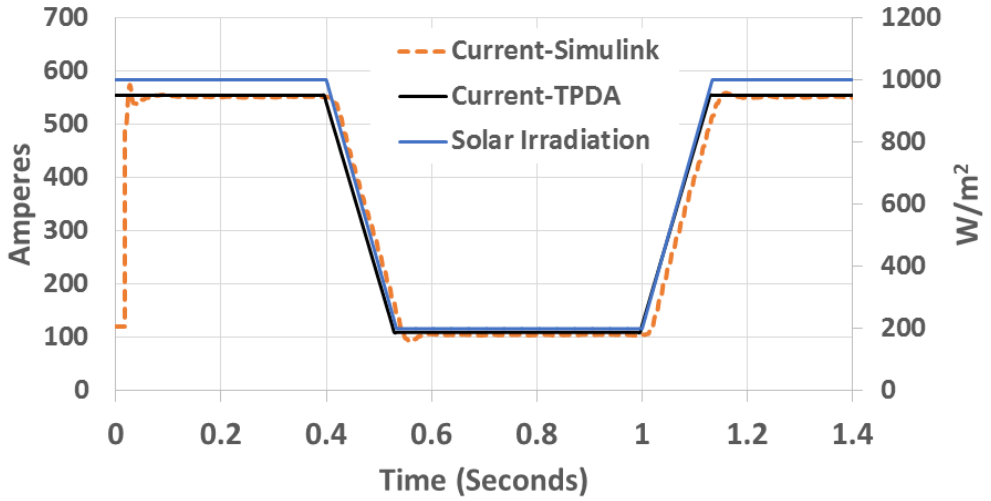

Fig. 34: Solar Irradiation Transient and Injected Currents on the Low Voltage side of Transformer T1 by the Solar PV Unit

5.4.2 Test 2

The second test used a much slower solar transient than test 1, a gradient of 50 $W/m^2/second$. The solar transient profile used in the study is shown in Fig. 35. The network topology used for this test was the same as that used in test 1, however, load L1 was changed from 150 kW to 1 MW and Load L2 was changed from 25 MW to 2 MW. The initial power output of the solar inverter was kept the same as before, i.e., 240 kW.

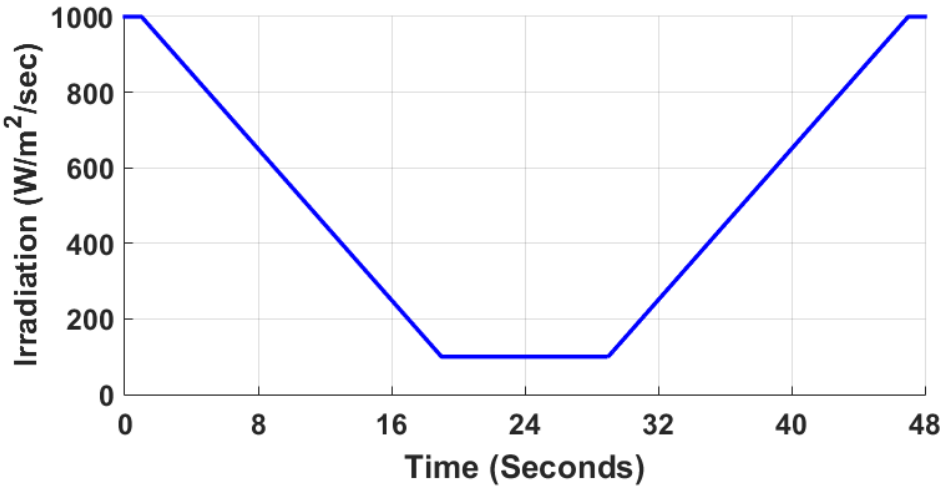

Fig. 35: Solar Transient Profile

Fig. 36 compares the ac line currents injected by the solar PV models on the low voltage side of transformer T1, while Fig. 37 shows the line currents on the high voltage side of T1, which is the PCC. Both the figures show that, similar to test 1, the currents injected by the D-PV model (as simulated in TPDA) and Simulink's detailed inverter model match well. This case study provides further verification of the ability of the D-PV model to vary its output current according to the incident solar irradiation.

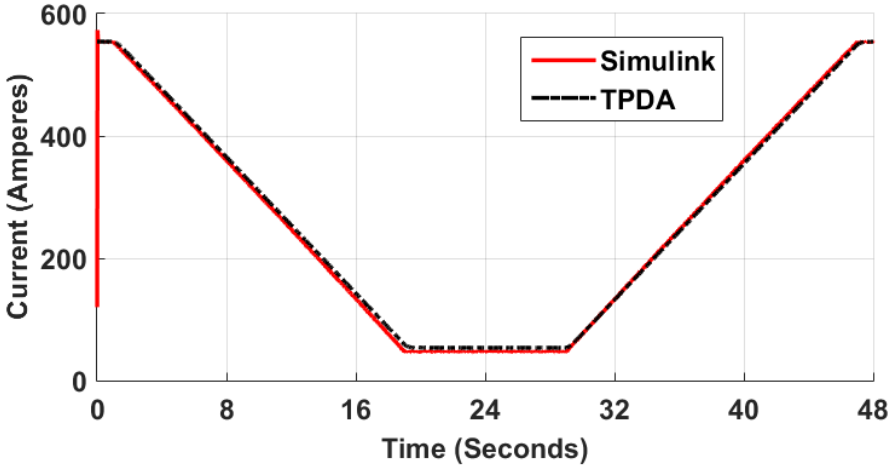

Fig. 36: Line Current Injected by the Solar PV Models on the Low Voltage side of Transformer T1

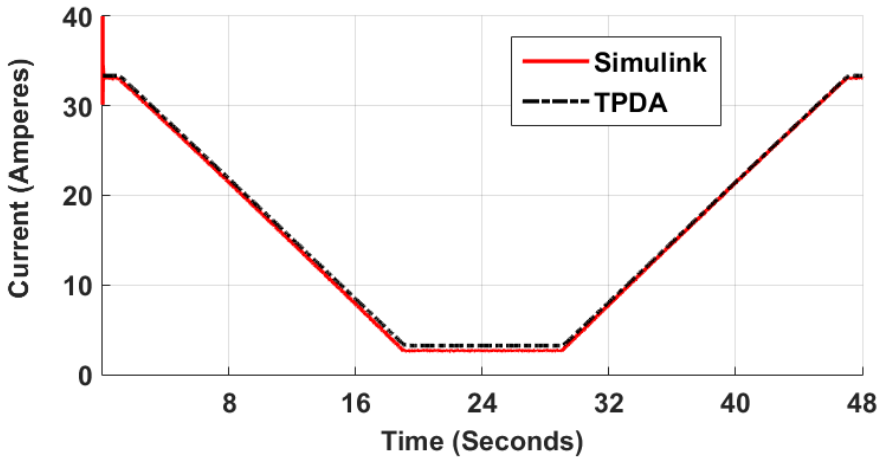

Fig. 37: Line Current Injected by the Solar PV Models on the High Voltage side of Transformer T1

5.5 Verification of the D-PV Model Control Methodology under Network Unbalance

As discussed in chapter 4, the D-PV model injects balanced currents at the PCC. Reference [70] discusses a method for controlling solar PV inverters such that they inject balanced currents at the PCC. Moreover, the approach used in the D-PV model to obtain the current control expressions of chapter 4 is similar to that used in [70]. Therefore, the circuit given in [70] was used to compare the performance of the D-PV model with the detailed switching model of the PV inverter in [70] when the inverter is interfaced with an unbalanced network.

As mentioned in [70], the circuit was balanced at the start of the simulation and the voltage source was forced to generate unbalanced voltages after 0.05 seconds. As discussed in Chapter 4, the interaction of unbalanced voltages and balanced currents results in generation of instantaneous power at the PCC that includes a second harmonic component superimposed on the dc component. This observation can be made in Fig. 38, which shows the profile of the real power generated by the D-PV module using TPDA. The profile matches closely with the profile given in [70], and the second harmonic oscillations are observed after 0.05 seconds. However, the average real power stays the same throughout the simulation, since the reference real power did not change from its initial value. This shows that the D-PV model was able to control the real power at the PCC under unbalanced network conditions. It should be noted that the shape of the oscillations does not appear sinusoidal in Fig. 38 because the integration step used in TPDA is $1/4^{th}$ of a cycle.

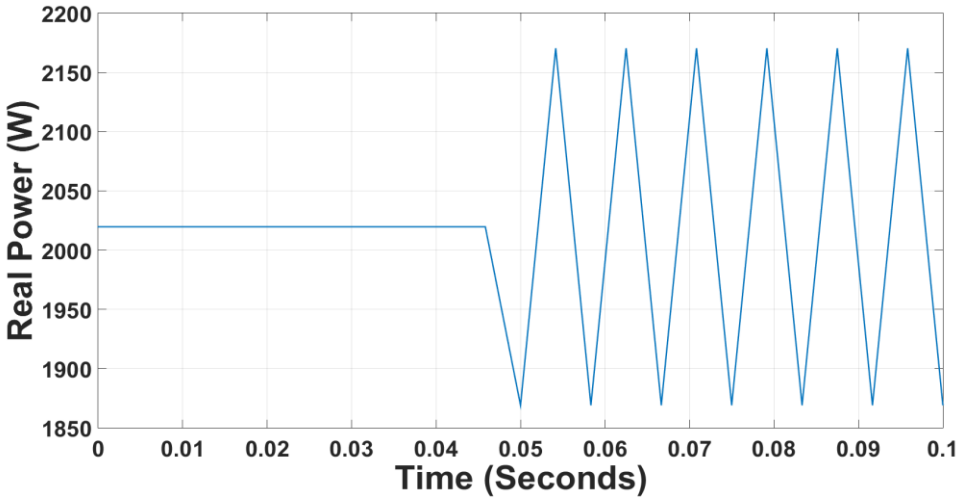

Fig. 38: Real Power at Inverter Terminal obtained with the D-PV model

5.6 Concluding Remarks

This chapter demonstrated that TPDA was able to accurately simulate the dynamics of power systems under balanced and unbalanced network conditions, as the rotor speed and voltage profiles matched well between TPDA and PSLF® and ATP. In case study 5 it was shown that the initialization procedure used in TPDA resulted in the steady state being present from the start of the simulation when the network was unbalanced. At the end of the chapter, verifications for the D-PV model were presented to show that the model was capable of changing its output based on incident solar irradiation, and could generate reference real and reactive powers when the network was unbalanced.

This chapter clears the way for using TPDA and the D-PV model to study the impact of solar PV-based DG on the dynamics of power systems using three phase integrated T&D network models. Such studies are discussed in the next chapter.

CHAPTER 6: SOLAR PV IMPACT ASSESSMENT STUDIES USING TPDA

6.1 Introduction

The objective of this chapter is to demonstrate the application of TPDA in evaluating the impact of solar PV-based DG on the dynamics of power systems. Through a series of studies it will be shown that using three phase transmission network models and integrated T&D network models enable progressively more accurate assessment of the impact of solar PV on power systems dynamics than traditional dynamic simulation programs that use a positive sequence transmission network model. The simulations for all the studies are performed using TPDA and the solar PV units are modeled using the D-PV model.

The chapter is divided into three major sections. In the first section the approach used for preparing the network models for the studies is presented. This section identifies the steps followed for obtaining the integrated T&D model (referred to as the hybrid model, hereafter), and the corresponding balanced and unbalanced transmission only models (referred to as T-only models, hereafter). In the second section detailed description of case studies is provided. These case studies are intended to compare the dynamic response of the hybrid and T-only models when solar PV is added to these models. Addition of solar PV units to the network models, their locations, types of disturbances, and scenarios studied are discussed in detail in this section. Finally, the third section presents and discusses the results of the case studies.

6.2 Developing Network Models for the Case Studies

The discussion of the network models begins with the steps followed to develop the hybrid model. The creation of balanced and unbalanced T-only models from the hybrid model is also discussed.

6.2.1 Developing the Hybrid Model

The hybrid network model was developed using the publically available, standard IEEE models of transmission and distribution systems. The reason for this choice of network topologies was to enable easy sharing of data and results with the power systems community.

The IEEE 39 bus system was used to model the transmission network topology of the hybrid model. The IEEE 39 bus system has 19 load buses, which represent the aggregated load of the distribution networks that are supplied from these buses, but are not represented in the model. The original intent was to replace all the 19 aggregated loads by 19 distribution networks that were made from IEEE 123 bus distribution feeders [76]. However, this would require adding hundreds of distribution feeders to the IEEE 39 bus system, as each IEEE 123 bus feeder can supply limited power without excessive voltage drop. This can be seen from Fig. 39, which shows that at around twice the nominal loading the minimum voltage in the 123 bus feeder drops below 0.9 p.u. which is outside the typical acceptable service voltage levels [77]. Therefore, assuming each feeder could pick up 7.6 MW of load without causing voltage violations, the number of feeders needed to pick up the 19 aggregated loads of the IEEE 39 bus system are given in Table 29. The nominal load values in Table 29 are based on [49].

While it is possible to model 808 feeders in DEW, and hence simulate them in TPDA, it was decided to limit the effort required to build the hybrid model, as a smaller model could also be used to demonstrate the advantages of using hybrid network models for evaluating the impact of solar PV units on power systems dynamics. Therefore, the nominal loads of the IEEE 39 bus system were reduced to 10% of their original values. The resulting actual power flows at 12 of the 19 load buses were distributed over 12 distribution networks, each of which consisted of 8 IEEE 123 bus feeders (actual and nominal loads were different due to the constant impedance load

model). This load distribution limited the maximum loading on any IEEE 123 bus feeder in a distribution network to about 5 MW, although individual feeder loads varied as the nominal values of feeder loads were scaled using scaling factors calculated as: Aggregated actual load at the transmission bus/total power that 8 feeders would supply at 1.0 p.u. voltage. Fig. 40 compares the actual aggregated loads of the 19 load buses in the T-only model and the power flow at the transmission buses of the hybrid model. The actual loads at the transmission load buses in the T-only and hybrid models closely match. Sources of differences include:

- Constant impedance load model assumed in the T-only model and the ZIP (constant impedance (Z), constant current (I) and constant power (P)) load model assumed in the hybrid model
- Losses in the distribution networks that were absent in the T-only model.

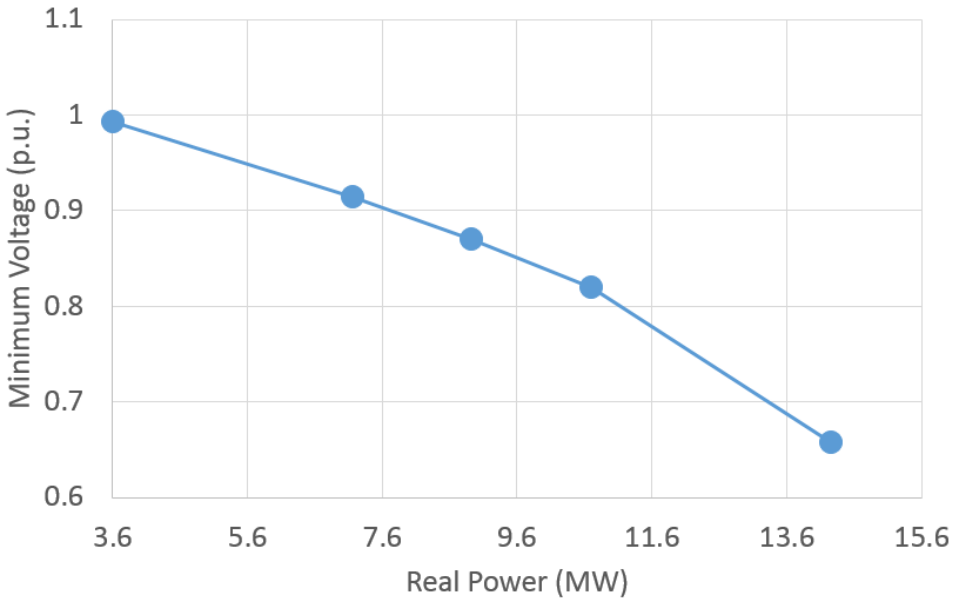

Fig. 39: Variation of Minimum Voltage vs Total Load in the IEEE 123 bus Feeder

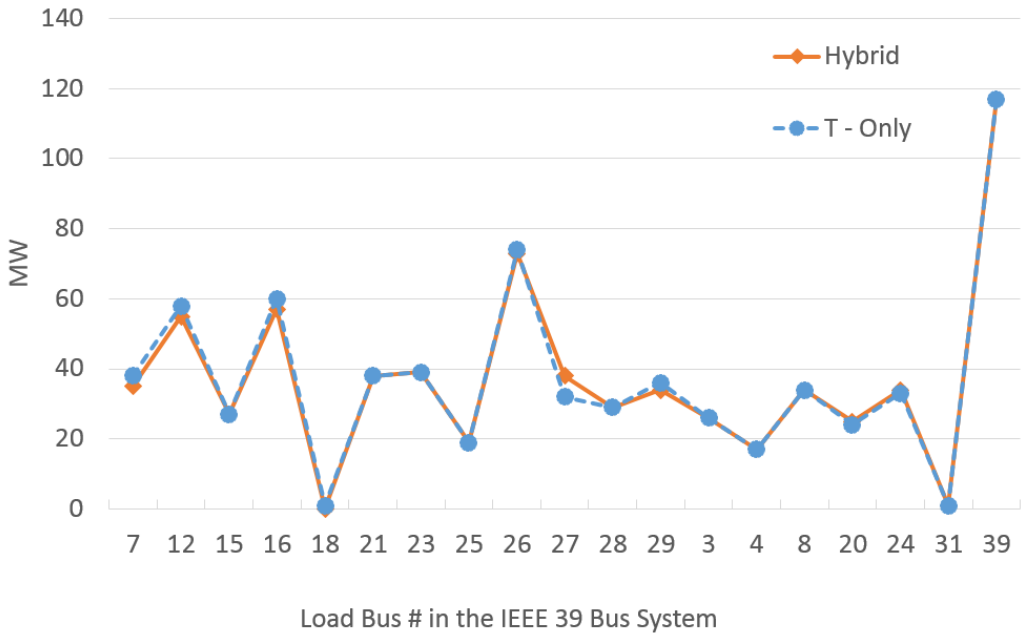

Fig. 40: Actual Load at the Transmission Load Buses in the T-Only Model and the Hybrid Model when the Nominal Load of the IEEE 39 Bus System Load is scaled to 10% of the Original Load

Table 29: Number of IEEE 123 Bus Feeders required to serve all Loads of the IEEE 39 Bus System

Load Bus #	Nominal Load (MW)	# of IEEE 123 Bus Feeders
3	322	45
4	500	69
7	234	32
8	522	72
12	8	1
15	320	44
16	329	46
18	158	22
20	680	94
21	274	38
23	247	34
24	309	43
25	224	31
26	139	19
27	281	39
28	206	29
29	284	39
31	9	1
39	1,104	153
Total	6,150	808

The hybrid model also contains detailed distribution substation models, whose configuration is shown in Fig. 41. The advantage of including the substation model is that it provides the capability

to evaluate the system stability when the network is reconfigured to restore power to loads that may lose power due to fault clearing [17].

Table 30 summarizes the number of components in the hybrid model. Compared to 128 components in the T-Only model, the hybrid model has over 33,000 components, which is an increase in system size of over 250 times. The schematic of the hybrid model built in DEW is shown in Fig. 42.

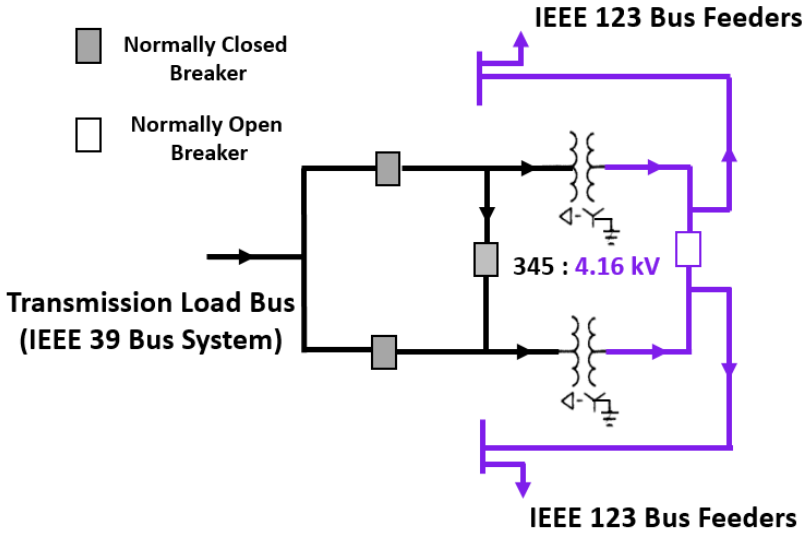

Fig. 41: Distribution Substation Configuration in the Hybrid Model

Table 30: Components in the Hybrid Model

Component	Quantity	Component	Quantity
Buses	11,847	Breakers/Switches	1,154
1-Phase Distribution Lines	5,280	1-Phase Loads	7,584
2-Phase Distribution Lines	288	2-Phase Loads	96
3-Phase Distribution Lines	5,280	3-Phase Loads	500
3-Phase Underground Cables	480	Voltage Regulators	384
Transformers	134	Fixed Shunt Capacitors	384
Synchronous Generators	10	3- Phase Transmission Lines	46
Total	33,457		

6.2.2 Preparing the Unbalanced T-Only Model from the Hybrid Model

To create the unbalanced T-only model, total phase-wise nominal loads of the distribution networks in the hybrid model were calculated for all the distribution networks. The phase wise nominal load values were assigned as nominal values of aggregated loads at the transmission buses, and the distribution networks were removed. The nominal values of the 7 aggregated loads in the hybrid model did not need to be changed. The constant impedance load model was assumed for the unbalanced T-only model.

6.2.3 Preparing the Balanced T-Only Model from the Unbalanced T- Only Model

As discussed earlier, the hybrid model was prepared from the balanced IEEE 39 bus system whose nominal load was reduced to 10% of the original load. Therefore, the balanced T-only model was already available. However, to ensure that the balanced and unbalanced T-only model loads had the same total nominal powers, the loads of the balanced T-only model were modified. The total unbalanced nominal load at each load bus of the unbalanced T-only model was divided into three equal parts and assigned to each phase of the load bus of the balanced T-only model.

Fig. 43 compares the actual power flows at the load buses for the hybrid, unbalanced T-only and balanced T-only models. The figure shows that the actual power flows at the load buses between the three models match well.

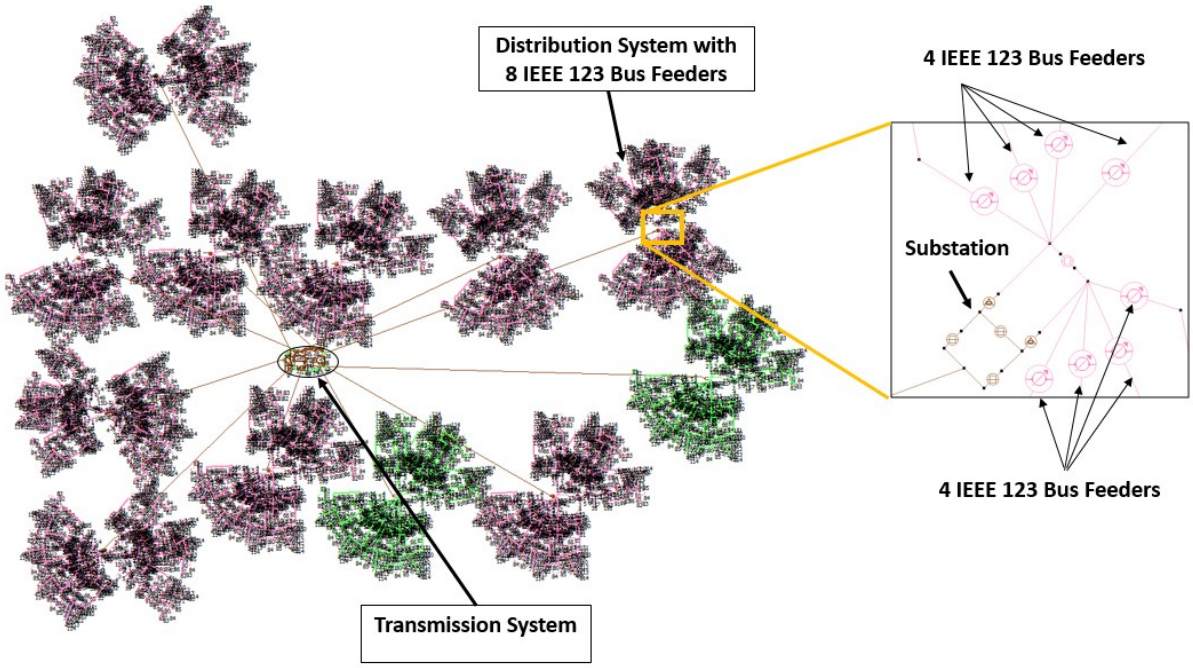

Fig. 42: Schematic of the Hybrid Model

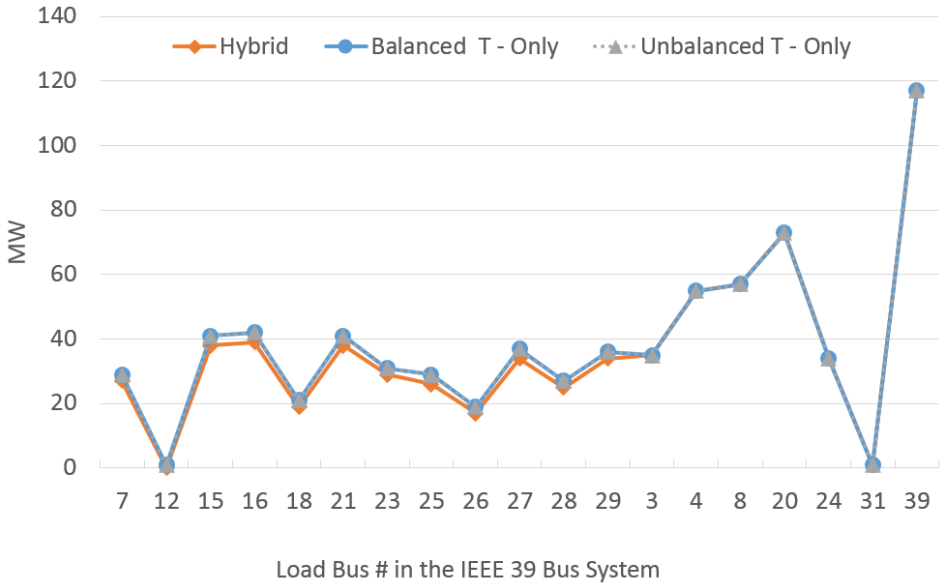

Fig. 43: Actual Load at the Transmission Load Buses in Hybrid, Unbalanced T-only and Balanced T-only Models

6.3 Description of Case Studies

Two case studies will be discussed in this section, each of which will consist of multiple scenarios to demonstrate the progressively more accurate solar PV impact assessment that can be

obtained using three phase and hybrid network models instead of the traditional dynamic simulation programs that use positive sequence transmission network models.

The two case studies discussed in this section use the D-PV model to simulate the dynamics of solar PV units in the power system. The case studies focus on two factors that improve accuracy:

- Ability to model network configurations and protection schemes that require three phase modeling (e.g. Single Pole Tripping (SPT))
- Ability to model and locate solar PV units accurately in hybrid models.

In case study 1, the impact of a bolted (zero impedance) single line to ground (SLG) fault on rotor speeds and voltages, under 0%, 5% and 10% PV penetration levels (% of total load) will be simulated, in the T-only model. In case study 2, the dynamic response of the hybrid model to a SLG fault and solar transient under 10% PV penetration level will be studied.

The remainder of this section will focus on describing the addition of solar PV units in the hybrid and T-only network models; simulation and clearing of the SLG fault; and simulation of solar transients.

6.3.1 Modeling Solar PV Penetration

Case Study 1

In case study 1, the T-only unbalanced and T-only balanced network models described in the previous section (hereafter referred to as base case 1 and base case 2, respectively) were used to model 5% and 10% PV penetration scenarios. In the 5% scenario, 26 MW of solar PV generation was added at bus 18 and 10 MW of solar PV generation was added at bus 12. In the 10% PV penetration scenario, an additional 20 MW and 12 MW of solar PV generation was added at buses 21 and 23, respectively. It was assumed that solar PV generation added at the transmission buses was an aggregate of all the distribution connected solar PV units that were generating equal power

in each phase. Therefore, three single phase solar PV units were modeled at each bus such that the three phase currents were balanced. This assumption needed to be made because, unlike the hybrid model, the T-only models do not model the distribution network in which the solar PV units are connected. The reference reactive power for solar PV units was specified to be zero. The dynamics of the solar PV units was modeled using the D-PV model.

To compensate for the addition of solar PV generation, the synchronous generator at bus 30 was removed in the 5% PV penetration scenario while the generator at bus 36 was additionally removed in the 10% PV penetration scenario. Fig. 44 shows the one-line diagram of the IEEE 39 bus system where the buses mentioned above are highlighted.

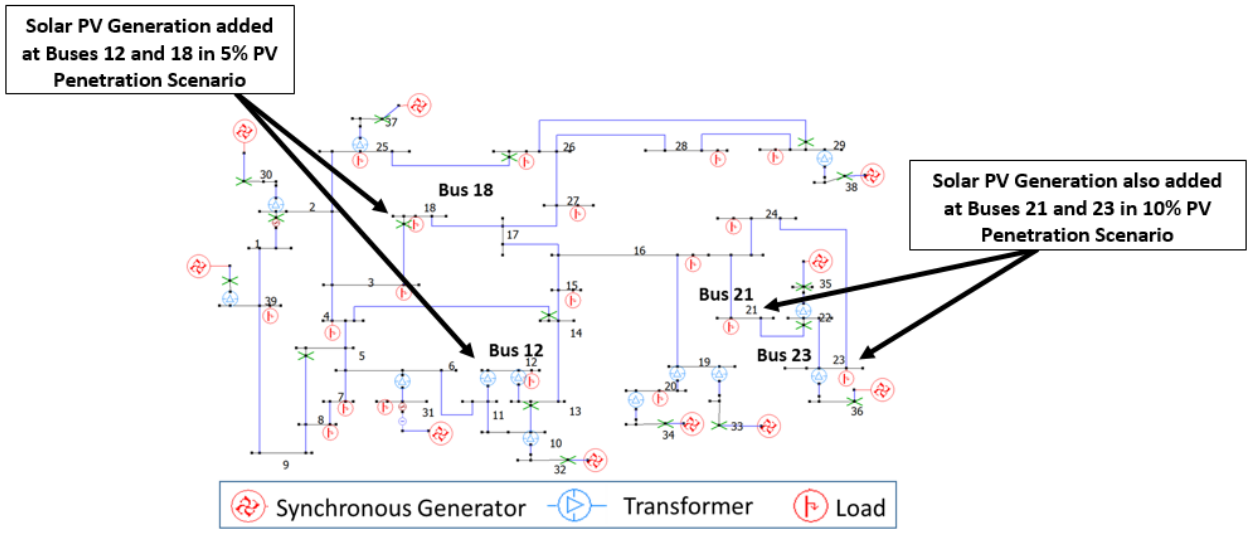

Fig. 44: Location of Solar PV Generation in Case Study 1

Case Study 2

The network model used in case study 2 was the hybrid model that was described in the previous section. It is referred to as the hybrid base case from hereafter. In case study 2, only the 10% PV penetration scenario was simulated. However, unlike case study 1, three phase solar PV units were added at their actual locations, i.e. at various locations inside the distribution networks

that were supplied by transmission buses 12, 18, 21 and 23. Unlike case study 1, the solar PV units did not have to be aggregated, as the distribution networks were modeled in the hybrid model.

Two capacity ratings were used for the solar PV units, 1 MW and 2MW, which resulted in a total of 58 solar PV units being added to the four distribution networks. The locations of solar PV units in the distribution networks is shown in Fig. 45. Please note that not all the distribution feeders had solar PV units connected at the solar PV generation locations marked in Fig. 45. Some feeders had a solar PV unit at only one of the three locations, while others had solar PV units at all the three locations.

Similar to case study 1, the D-PV model was used to model the dynamics of solar PV units, where the reference reactive power was specified to be zero. Table 31 shows the number and capacity of solar PV units added in the four distribution networks. Moreover, similar to the 10% PV penetration scenario of case study 1, synchronous generators at buses 30 and 36 were removed to compensate for the addition of solar PV units.

Table 31: Distributed Solar PV Units in Case Study 2

Distribution network connected to transmission bus #:	# of 1 MW Units	# of 2 MW Units	Total Units
12	8	1	9
18	16	5	21
21	16	2	18
23	8	2	10

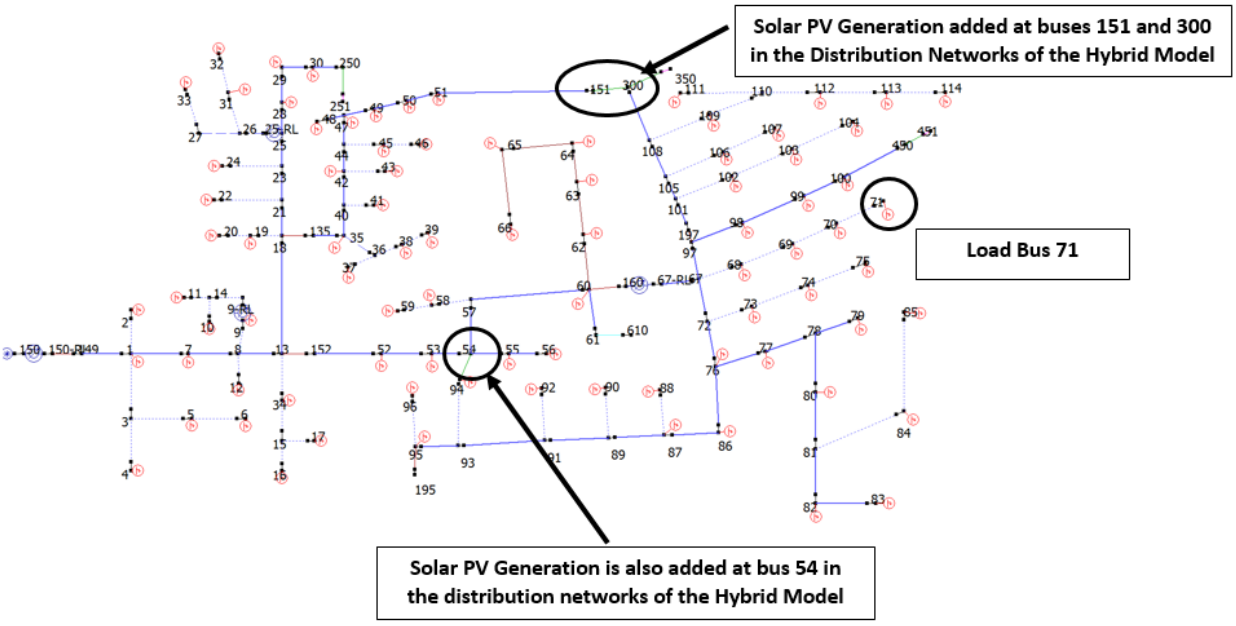

Fig. 45: Location of Solar PV Generation in the Hybrid Model

6.3.2 Fault Simulation

Case Study 1

The solid SLG fault, used to disturb the system from steady state in case study 1, was located at bus 18 of the transmission system. However, the approach for simulating the SLG fault was different in cases derived from base cases 1 and 2.

For cases derived from base case 1, the SLG fault was simulated by connecting an almost zero voltage, single phase voltage source to phase A of bus 18 at the end of the 5th cycle. In cases derived from base case 2, where the network and loads were balanced, the approach adopted in traditional dynamic simulation programs [7] was followed, where the negative and zero sequence

Thevenin impedance at bus 18 was calculated for a solid SLG fault, and the sum of these impedances was added as fault impedance of a three phase fault. The positive, negative and zero sequence Thevenin impedances for the bolted SLG fault at bus 18 were all equal to $1.3151 + 15.9840j$ ohms (all the transmission lines had equal positive, negative and zero sequence impedances).

The fault was cleared by opening lines 3-18 and 17-18 (see Fig. 44 for the locations of these lines), and tripping the solar PV unit at bus 18. In cases derived from base case 1, single pole tripping (SPT) was implemented to clear the fault by opening only phase A of the lines and the solar PV unit. On the other hand, in cases obtained from base case 2, three pole tripping (TPT) was used to clear the fault because these cases were designed as proxies for simulating dynamics using traditional programs, where only TPT can be implemented.

The fault was cleared after 10 nominal frequency cycles, and breakers on lines 3-18 and 17-18 were reclosed 30 cycles later. The tripped solar PV generation was restored 5 seconds after the fault was cleared.

Case Study 2

The SLG fault was simulated in the same manner as in the cases based on the unbalanced T-only network model of case study 1, i.e. SLG fault with SPT.

6.3.3 Solar Transient in Case Study 2

Two cases were prepared to model and study the impact of solar irradiation transients on power systems dynamics using hybrid models. Solar transients arise from the movement of clouds over solar PV units. Since hybrid models enable the modeling of geographic diversity of solar PV units, the impact on power systems of cloud cover moving across a distribution network and affecting the solar PV units at different times can be accurately simulated. In both cases the initial value of

solar irradiance was $1000 W/m^2$. It was assumed that the solar transient only affected the solar PV units in the distribution network connected to transmission bus 18. The rate of change of irradiation was assumed to be -200 $W/m^2/second$ and the ramp was assumed to last for 4.5 seconds, at which point it was assumed that the cloud had completely covered the distribution network. Solar irradiation was kept fixed at 100 $W/m^2/second$ thereafter for all the solar PV units connected to the distribution network supplied by transmission bus 18. The difference between the two cases was that in the first case the solar transient occurred simultaneously over all 21 solar PV units, and in the second case the solar transient at each unit was delayed by one second.

Table 32 summarizes the cases simulated in case studies 1 and 2.

Table 32: Simulations Performed in Case Studies 1 and 2

<table>
<tr><th>Case Study #</th><th>Base Case</th><th>Case Title</th><th>Solar PV</th><th>Disturbance</th><th>Dynamic Models</th></tr>
<tr><td rowspan="6">1</td><td rowspan="3">Base Case 1 (Unbalanced T-only Network Model)</td><td>Case 1.1</td><td>0%</td><td rowspan="3">SLG Fault with SPT</td><td rowspan="9">Generator: GENROU
Exciter: ST1A
Governor: TGOV1
Solar PV: D-PV
(Parameters for these models are the same as given in the previous chapter)</td></tr>
<tr><td>Case 1.2</td><td>5%</td></tr>
<tr><td>Case 1.3</td><td>10%</td></tr>
<tr><td rowspan="3">Base Case 2 (Balanced T-only Network Model)</td><td>Case 2.1</td><td>0%</td><td rowspan="3">SLG Fault simulated as equivalent Three Phase Fault with TPT</td></tr>
<tr><td>Case 2.2</td><td>5%</td></tr>
<tr><td>Case 2.3</td><td>10%</td></tr>
<tr><td rowspan="3">2</td><td rowspan="3">Hybrid Base Case (Hybrid Network Model)</td><td>Hybrid Case 1</td><td>10%</td><td>SLG Fault with SPT</td></tr>
<tr><td>Hybrid Case 2</td><td>10%</td><td>Simultaneous Solar Transient*</td></tr>
<tr><td>Hybrid Case 3</td><td>10%</td><td>Sequential Solar Transient**</td></tr>
</table>

* Solar transient starts at 0.5 seconds and ends at 4.5 seconds

** Solar transient at the i^{th} solar PV unit starts at $0.5 + (i - 1)$ seconds and ends at $0.5 + 4.5 + (i - 1)$ seconds; $i = 1\ to\ 21$

6.4 Case Study Results

Plots of deviation of rotor speeds from nominal speed (60 Hz), and voltage magnitudes are used to compare the dynamic response of the power system in the two case studies. The deviation of the rotor speed from nominal is chosen because standards, such as NERC's PRC-024-2 [78], define the acceptable frequency profile for the generators, and frequency excursions beyond this region can trip generators, which can be detrimental to the stability of a power system.

Case Study 1

The rotor speed deviations for the generator connected at bus 31 are shown in Fig. 46. Since the generators were in synchronism in all the cases simulated in case study 1, rotor speed deviations of other generators are not shown. Fortunately, the rotor speeds of generators in all the cases stayed within the acceptable region [78]. The following observations regarding rotor speed deviation from nominal frequency can be made from Fig. 46:

- The lowest points in the rotor speed deviation profiles are observed for cases 2.2 (-0.014 Hz) and 2.3 (-0.015 Hz), which are about 300% lower than the lowest points in the deviation profiles of cases 1.2 and 1.3 (-0.005 Hz). The reason for larger rotor speed deviations in cases 2.2 and 2.3 than in cases 1.2 and 1.3 is the larger mismatch between initial generation of the synchronous generators and the generation after the fault is cleared.

  In cases 2.2 and 2.3, solar PV generation was lost in all the three phases of Bus 18 due to TPT, which was not restored till 5.25 seconds. In cases 1.2 and 1.3, however, solar PV generation of only phase A was lost due to SPT. Since the real power output of the remaining solar PV units did not change (because the solar irradiation did not change), the electrical power demand from the synchronous generators increased from their initial values, which caused the rotor speeds to decrease (the turbine/governors could not increase the mechanical power fast enough

to arrest the decline in rotor speeds). Since the system wide increase in power demand from the synchronous generators was larger in cases 2.2 and 2.3 (~28 MW), compared to cases 1.2 and 1.3 (~10 MW), the rotor speeds reduced more in the former. The rotor speeds continued to decrease till 5.25 seconds after which the tripped solar PV units were restored, resulting in the restoration of the initial conditions and the rotor speed deviations eventually settled to zero in cases 1.2, 1.3, 2.2 and 2.3.

- Rotor speed deviation is the lowest for cases 1.1 and 2.1. This is due to the restoration of the initial conditions in 0.75 seconds, immediately after the breakers are reclosed, compared to 5.25 seconds for the cases with solar PV.

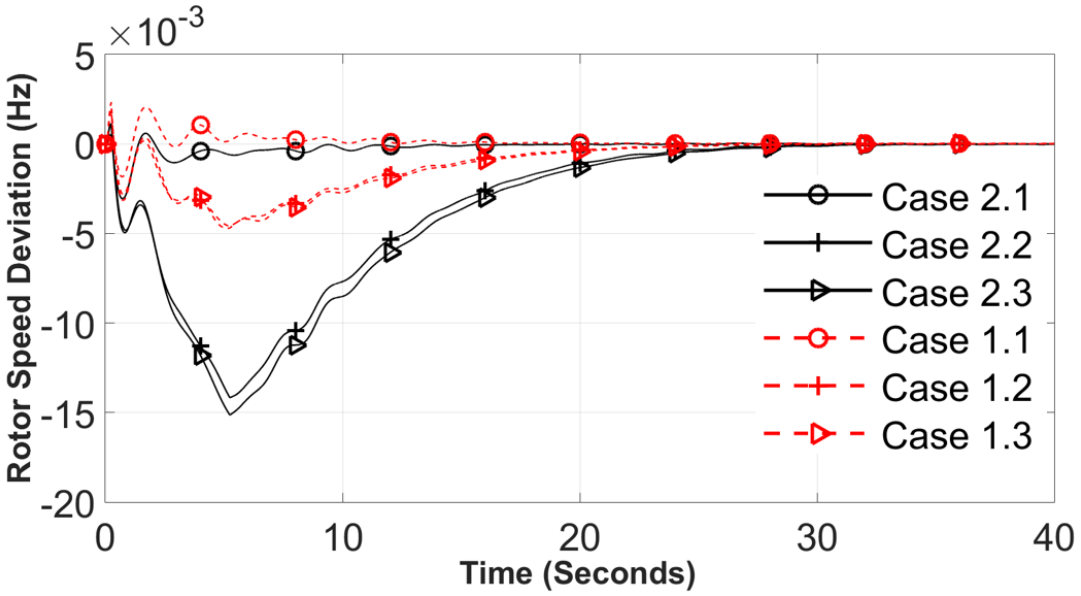

Fig. 46: Rotor Speed Deviation of Generator at Bus 31

Three phase voltages at bus 3, which is adjacent to bus 18, are plotted in Fig. 47, from which the following observations can be made:

- During the fault, the three phase voltages in cases 1.2 and 1.3 are not equal, and phase A voltage is significantly lower than the voltages obtained in cases 2.2 and 2.3. On the other hand, phase

B and C voltages in cases 1.2 and 1.3 are significantly higher (close to 1.05 p.u.) than those obtained in cases 2.2 and 2.3.

- Cases 1.2 and 1.3 show that the voltage on phase A drops below 0.5 p.u., and stays there for the duration of the fault. Such voltage sags can result in power quality issues, such as stalling of air-conditioners [17]. However, in cases 2.2 and 2.3, phase A voltage stays close to 0.8 p.u. for 10 cycles, a level which ITIC compliant equipment should be able to sustain without any effect on performance.
- Unlike the rotor speeds, restoration of solar PV generation has negligible effect on the voltage profile of bus 3. This is evident from the imperceptible effect on the voltages after 5.25 seconds.

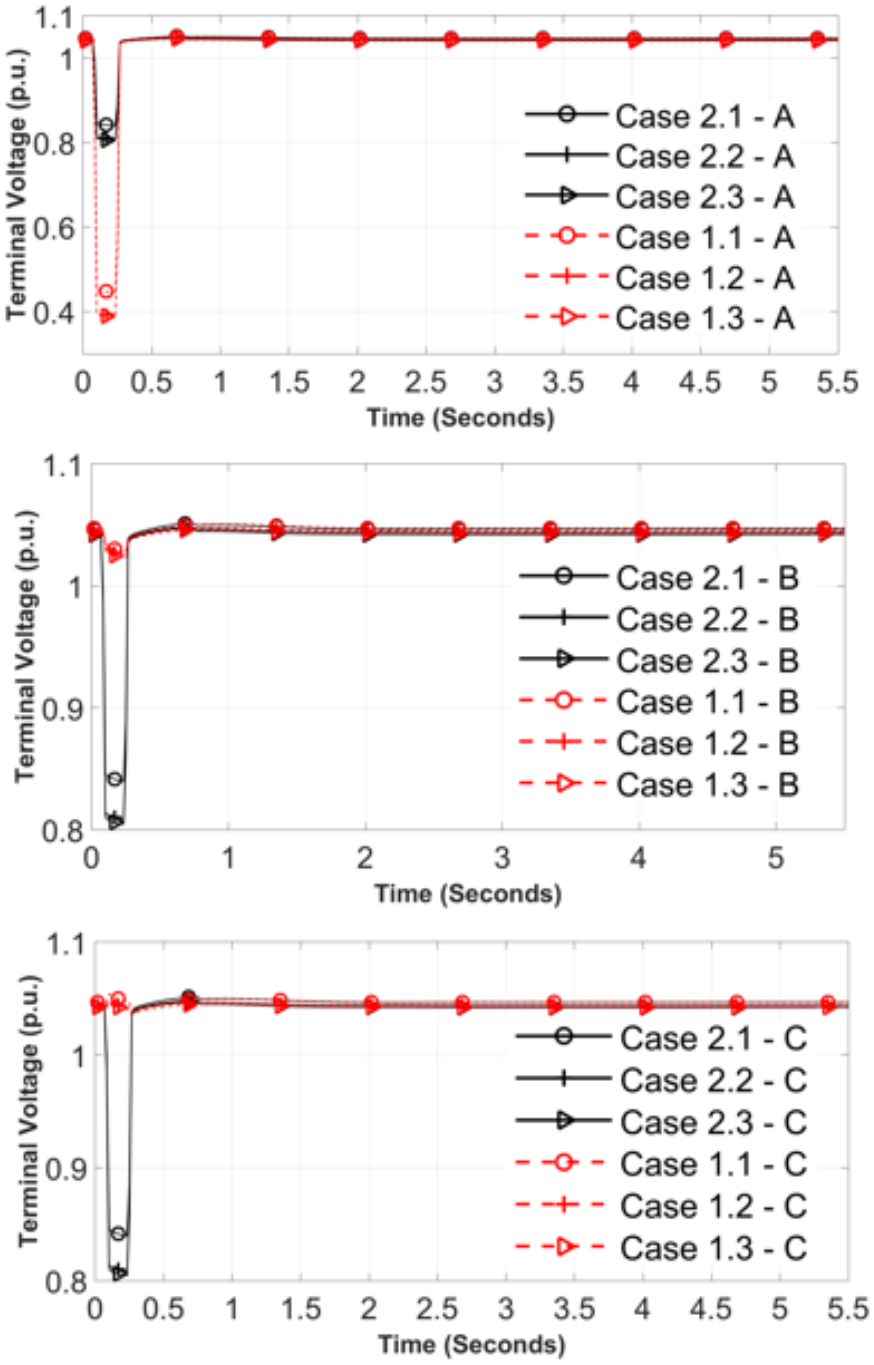

Fig. 47: Three Phase Voltages at Bus 3 in Case Study 1

Based on the above observations for rotor speeds and bus voltages, it can be concluded that using three phase network models for studying the dynamic response of power systems in the presence of solar PV provides an opportunity to evaluate scenarios that cannot be studied using traditional dynamic simulation programs that assume a balanced network topology – SPT and its

effects on power systems dynamics is one example of such a scenario. Moreover, dynamic response obtained using three phase models can be significantly different from that obtained using positive sequence models to the extent that potentially undesirable conditions may not be recognized with traditional simulation techniques, as was observed in the case of voltage sags on phase A.

Case Study 2 – Hybrid Case 1

The rotor speed of the generator at bus 31 is shown in Fig. 48. This case is very similar to case 1.3 of case study 1. However, a comparison of rotor speed deviation (with Fig. 46) shows that the lowest point in the deviation profile for this case (-0.003 Hz) is 167% higher than that for case 1.3 (-0.005 Hz).

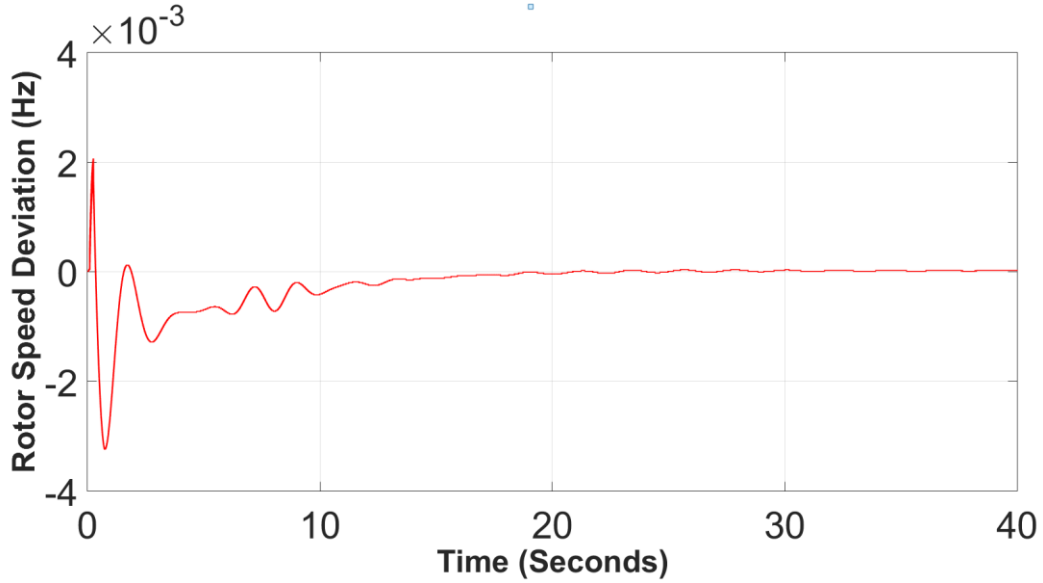

Fig. 48: Rotor Speed of Generator at Bus 31 (Hybrid Case 1)

Terminal voltages at phase A of transmission bus 18, and distribution buses 54, 71 (locations marked in Fig. 45), and 300, which are supplied by the transmission bus, are shown in Fig. 49. Key observations from the figure are:

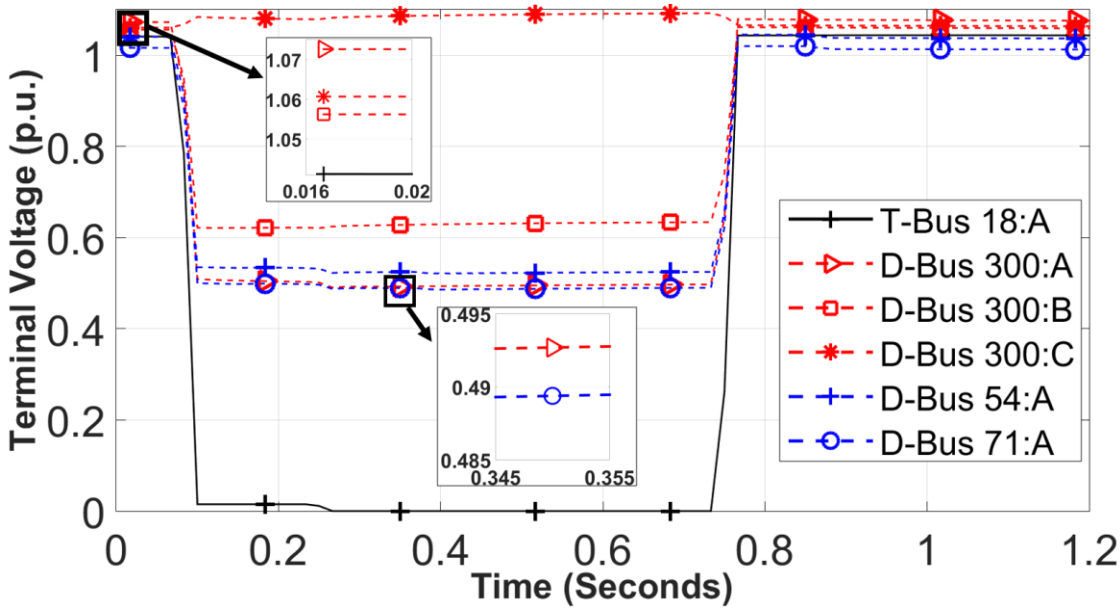

Fig. 49: Voltage at Transmission (T) Bus 18 and Distribution (D) Buses supplied by Bus 18 (Hybrid Case 1)

- Pre-fault steady state voltages at the distribution buses are different from the transmission bus voltage which supplies them. For example, the voltage at phase A of bus 300 is 1.07 p.u., compared to the transmission bus voltage of 1.04 p.u.
- While phase A voltage at the transmission bus drops to zero during the fault, and stays at zero after the fault is cleared, (till the tripped phase is restored after 30 cycles of fault clearing), voltages at distribution buses 300, 54 and 71 stay above 0.45 p.u. for the entire duration of the simulation. As mentioned earlier, buses 300 and 54 are the PCC for solar PV units.

The above observations can be explained using Fig. 50, which shows the post fault configuration of bus 18 in case study 2. Fig. 50 shows that when the SLG fault is cleared by opening phase A of the breakers, all three transformer windings remain energized. Moreover, if the transformer is ideal, the Delta-Wye (Dy1) connection and symmetry of windings result in phase C on the Wye side having the same per unit voltage as the BC winding, while phases A and B will have half the BC winding voltage. These assertions are corroborated by the three phase voltages of Bus 300 in Fig. 50, where the small difference in A and B phase voltages is due to the bus

location downstream of the transformer. Fig. 50 also shows that at bus 300 the lowest voltage, which is at phase A, stays above 0.5 p.u. due to which the solar PV unit connected to this bus does not trip (As per 1547.a guidelines [79], solar PV units may remain online for at least 1 second if the voltage is between 0.45 and 0.6 p.u.).

Similar voltage profiles at the PCC of the remaining 20 solar PV units prevents them from tripping due to which, the initial conditions are restored in 0.75 seconds against 5.25 seconds for case 1.3. As a result, the rotor speed deviation from nominal for the hybrid case 1 is less than that for case 1.3.

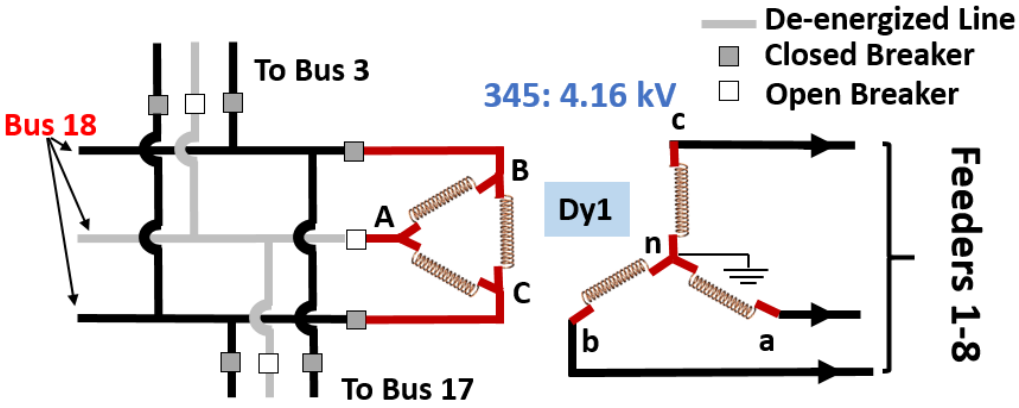

Fig. 50: Bus 18 Post Fault Configuration in Hybrid Case 1

These results demonstrate that assessing the impact of solar PV on power system dynamics using hybrid models not only allows the evaluation of scenarios that cannot be simulated using balanced network models, but also provides insights about the dynamic response of the power systems that cannot be revealed, even with three phase T-only models. The difference in responses between hybrid and T-only models for the same disturbance can be significantly different, as is seen above.

Case Study 2 – Hybrid Case 2 and 3

The effects that solar transient had on rotor speeds and distribution system voltages in hybrid cases 2 and 3 are shown in Fig. 51 and Fig. 52, respectively.

The following observations can be made from these figures:

- The solar transient does not have an adverse impact on system stability in both the cases. While rotor speeds and terminal voltages drop, the drop is gradual (at different rates), and does not result in loss of synchronism or voltage collapse.
- The final steady state of the system in both cases is identical up to the 3rd decimal place. This can be attributed to the same final irradiation level at all the solar PV units and intentional blocking of distribution network controllers, such as capacitors and tap-changing transformers during the simulation.
- Although the final steady states are almost identical, the time taken to reach the steady states is significantly different. For example, while the steady state of the voltage at bus 300 in hybrid case 2 is reached in about 5 seconds, in hybrid case 3 the voltage reaches the steady state in about 21 seconds.
- The rate of change of both rotor speeds and terminal voltages between the initial and final steady states is lower in hybrid case 3 than in hybrid case 2.

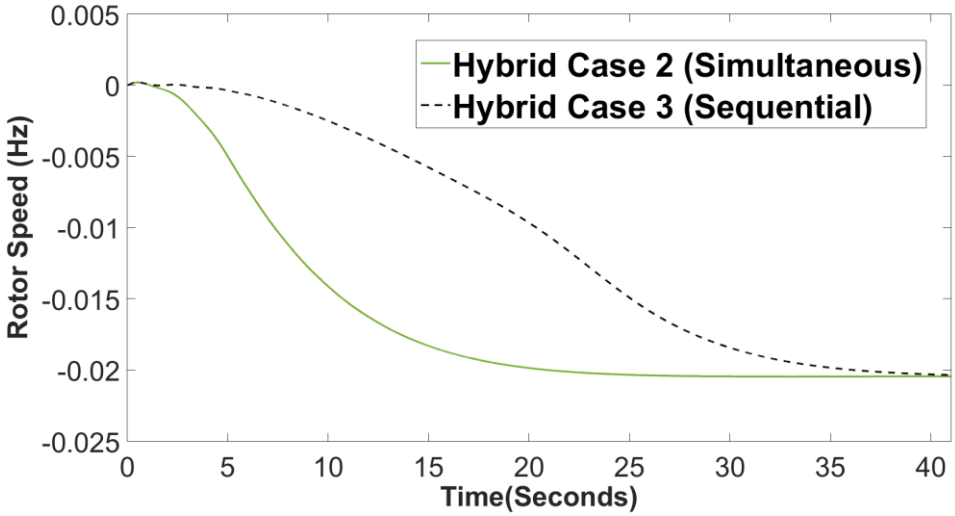

Fig. 51: Rotor Speed Deviation in Hybrid Cases 2 and 3

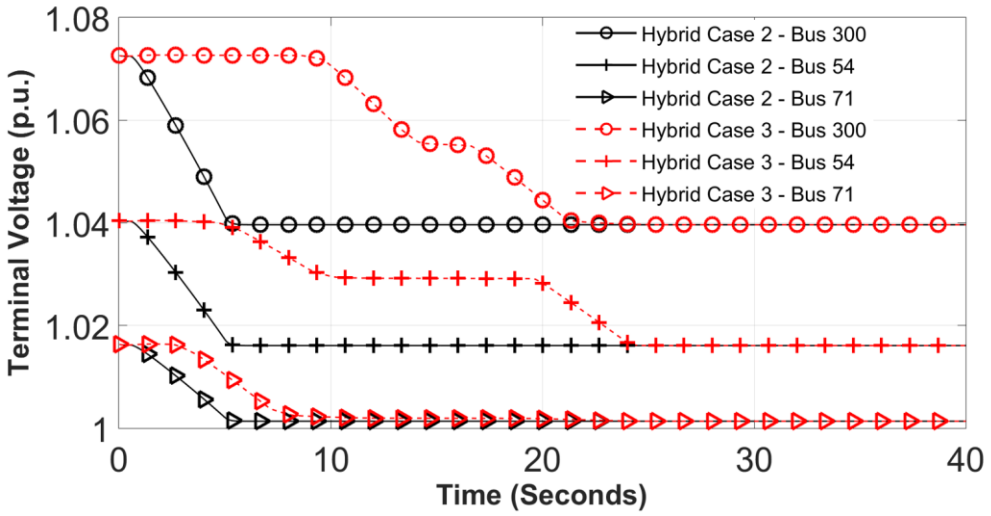

Fig. 52: Phase A Voltages at Three Distribution Buses in Hybrid Cases 2 and 3

These observations illustrate that the dynamic response of a power system to solar transients depends on the way solar transients are simulated. A more realistic solar transient simulation in hybrid case 3 resulted in a less severe transient response as seen by the lower rate of change of rotor speeds and terminal voltages. In hybrid cases 2 and 3, nonlinear distribution system controllers, such as capacitor banks and voltage regulators, were blocked from controlling voltages. If, however, these controllers were allowed to operate, the difference in time required to arrive at steady states in the two cases suggests that the controllers would have responded differently in the two cases, potentially resulting in different final steady states. Hybrid network models enable accurate analysis of the impact of various profiles of solar transients as they provide the ability to model the geographic diversity of solar PV units that are distributed across the distribution networks.

6.5 Concluding Remarks

The objective of this chapter was to highlight the advantages of using three phase transmission network models and hybrid models for studying the impact of solar PV generation on power

systems dynamics. Using TPDA and the D-PV model for simulating the dynamics of solar PV units, a series of simulations were performed which showed that:

- The dynamic response of power systems obtained with three phase transmission network models and hybrid models can be significantly different from the response obtained with traditional dynamic simulation programs.
- Using hybrid models for studying the impact of solar PV-based DG on dynamics of power systems can reveal insights about power systems dynamics that cannot be revealed with transmission only network models.
- The manner in which a solar transient is simulated affects the dynamic response of a power system, indicating the need for accurate simulation of solar transients, which is only possible with hybrid network models, as they allow the geographic diversity of solar PV units to be accurately modeled.

CHAPTER 7: CONCLUSIONS, CONTRIBUTIONS AND FUTURE WORK

7.1 Conclusions and Contributions

A new approach for studying the dynamics of power systems has been presented in the dissertation. Instead of simplifying the power system models such that they can be simulated using existing programs, the analysis approach and program presented in the dissertation enables simulation of power system dynamics using accurate models of power systems, where the artificial distinction between transmission and distribution networks is eliminated; assumption of balanced transmission networks is not required; and detailed models of substations connecting the transmission and distribution networks are included in the power system models. The theory and results discussed show that it is possible to develop a program that can simulate power system dynamics using such accurate models, and solar PV impact studies performed using the program and integrated transmission and distribution system models provide insights about the dynamic response of power systems that cannot be obtained using traditional dynamic simulation approaches that rely on transmission only models.

Power system planners can benefit from the research presented in the dissertation as it provides them the ability to accurately evaluate the impact of distributed generation on the dynamics of their networks. Since accurate network models are used in the studies and locational diversity of distributed generation is preserved, the results of such studies can be used by the planners to specify with greater confidence the penetration levels of distributed generation that can be safely accommodated in the network and the upgrades that will be needed to increase the penetration levels of distributed generation.

A brief summary of the major contributions of the dissertation is given below. The major contributions are:

1. Discussion on the fundamental concepts of graph trace analysis, particularly the concept of edge-edge graphs and their inherent ability to exploit the sparse nature of electric networks for minimizing storage requirements. It is shown that storage for edge-edge graphs of circuit models with no parallel components is the same as that used for their sparse adjacency matrices. In addition, equations for solving radial, looped and multi-source circuits are written by tracing through their edge-edge graphs, and it is shown that solving these equations solves the circuits correctly. The ability of graph trace analysis based power flow analysis algorithms to solve both radial and looped circuits enables them to solve integrated transmission and distribution system models.
2. A three phase dynamic simulation approach and program (TPDA) which can simulate electromechanical transients using three phase differential algebraic equations. Since TPDA uses algebraic equations based models of electric networks, it can be used to simulate the dynamics of utility scale integrated transmission and distribution system models.
3. A new dynamic model for small solar PV units, the D-PV model. This model can interface with unbalanced networks and independently control real and reactive power injections at the point of common coupling. The impact of transformer configuration on the real and reactive power control equations can be incorporated into the model, which is a novelty. Since solar PV-based distributed generation is connected to distribution networks, which are unbalanced, the D-PV model does not need to assume a balanced point of common coupling, thereby eliminating the resulting inaccuracies in dynamic simulations. Moreover, the D-PV model includes a model of solar panel arrays, which enables it to change its real power output in response to the incident solar irradiation. Therefore, impact of solar transients on power systems dynamics can be simulated.

4. A new approach for evaluating the impact of solar PV-based distributed generation on the dynamics of power systems using utility scale integrated transmission and distribution system models. These studies demonstrate that:
    a. It is important to include detailed distribution substation models, and three phase models of transformers, in power system models. These modeling features are currently neglected in system wide dynamics studies. It was shown in chapter 6 that the presence of a Wye-ground-Delta transformer in the distribution substation kept load and solar PV units energized before and after the single line to ground fault was cleared, which resulted in faster restoration of the initial system configuration and lesser deviation of generator rotor speeds from their nominal values. This observation could not have been made if the distribution substation was not modeled in detail in the study.
    b. Transmission only models are inadequate for studying solar transients as the geographical diversity of solar PV units cannot be modeled in transmission only models, where several solar PV units are modeled as one large solar PV unit connected to the transmission bus. It was shown in Chapter 6 that with integrated transmission and distribution system models realistic solar transient profiles can be simulated, which result in different voltage profiles at different locations in the distribution system and different rotor speed profiles than are obtained by assuming an unrealistic solar transient profile that affects all solar PV units at the same time.

7.2 Future Work

The dissertation presented a new way of thinking about and solving the power systems dynamic simulation problem. It also made available a program, a solar PV model, and a study approach that

can be used as building blocks for future research using integrated transmission and distribution system models of power systems. Some of the potential areas of research include:

- Modeling of equipment with slower dynamics such as boilers, over/under excitation limiters, and automatic generation control to more accurately simulate how solar PV transients can impact the dynamics of power systems. Dynamic models of distribution level controllers such as tap changers, switched capacitors and voltage regulators can also be included in such studies.
- As smart inverter based solar PV units start to proliferate in the power system, interactions among the controllers of such inverters, and with other distribution level controllers can be studied, and the impact of such interactions on power systems dynamics can be evaluated.
- Integrated transmission and distribution system models also provide the opportunity for more accurate fault induced delayed voltage recovery (FIDVR) studies as the locational impact of air conditioners can be included. Moreover, the impact of solar PV generation in voltage recovery after faults can also be evaluated.
- Besides applying TPDA for performing studies such as the ones discussed above, research efforts on developing standard integrated transmission and distribution system models can be very useful. Such a model can be used to test and verify integrated transmission and distribution system analysis algorithms that have been developed, or will be developed in the future.
- Finally, the concept of integrated transmission and distribution network models can be extended to include other physical domains, such as the gas and water infrastructure and communication networks. Such a multi domain model of the electric grid can help in improving the efficiency and reliability of power system operations and planning by enabling power

system engineers to make decisions based on the actual interactions between various domains, instead of modeling such interactions based on predefined sets of rules.

BIBLIOGRAPHY

[1] D. P. Kothari and I.J. Nagrath, *Modern Power System Analysis*, 3rd ed., New Delhi: Tata McGraw Hill, 2003.

[2] W. F. Tinney and J. W. Walker, "Direct solutions of sparse network equations by optimally ordered triangular factorization," *in Proceedings of the IEEE*, vol. 55, no. 11, pp. 1801-1809, Nov. 1967. doi: 10.1109/PROC.1967.6011

[3] W. F. Tinney and C. E. Hart, "Power Flow Solution by Newton's Method," *in IEEE Transactions on Power Apparatus and Systems,* vol. PAS-86, no. 11, pp. 1449-1460, Nov. 1967. doi: 10.1109/TPAS.1967.291823

[4] W. Tinney and W. Meyer, "Solution of large sparse systems by ordered triangular factorization," *in IEEE Transactions on Automatic Control*, vol. 18, no. 4, pp. 333-346, Aug 1973. doi: 10.1109/TAC.1973.1100352

[5] B. Stott, "Review of load-flow calculation methods," in *Proceedings of the IEEE*, vol. 62, no. 7, pp. 916-929, July 1974. doi: 10.1109/PROC.1974.9544

[6] Stott, B., "Power System Dynamic Response Calculations," *in Proceedings of the IEEE*, vol.67, no.2, pp. 219-241, Feb. 1979. doi: 10.1109/PROC.1979.11233

[7] P. Kundur, *Power System Stability and Control*, New Delhi: Tata McGraw Hill, 2012.

[8] R. Concepcion, M. Donnelly, R. Elliot, and J. Sanchez-Gasca "Extended-Term Dynamic Simulations with High Penetrations of Photovoltaic Generation," Sandia National Laboratories, SAND2016-0065, Jan. 2016. [Online]. Available: http://prod.sandia.gov/techlib/access-control.cgi/2016/160065.pdf. [Accessed: Oct. 1, 2016].

[9] W.H. Kersting, *Distribution System Modeling and Analysis*, CRC Press LLC, 2002.

[10] R. D. Zimmerman, "Comprehensive Distribution Power Flow: Modeling, Formulation, Solution Algorithms and Analysis," Ph.D. dissertation, Cornell University, ProQuest Dissertations Publishing, 1995.

[11] D. Shirmohammadi, H.W. Hong, A. Semlyen, and G.X. Luo, "A compensation-based power flow method for weakly meshed distribution and transmission networks," *in IEEE Trans Power Systems*, vol.3, no.2, pp. 753-762, May 1988. doi: 10.1109/59.192932

[12] G. W. Chang, S. Y. Chu and H. L. Wang, "An Improved Backward/Forward Sweep Load Flow Algorithm for Radial Distribution Systems," *in IEEE Transactions on Power Systems*, vol. 22, no. 2, pp. 882-884, May 2007. doi: 10.1109/TPWRS.2007.894848

[13] Environmental Protection Agency, “Distributed Generation of Electricity and its Environmental Impacts,” US Environmental Protection Agency (EPA). [Online]. Available: https://www.epa.gov/energy/distributed-generation . [Accessed: Oct. 1, 2016].

[14] Navigant Consulting, "Assessment of Demand-Side Resources within the Eastern Interconnection," EISPC and NARUC, Mar. 2013. [Online]. Available: http://pubs.naruc.org/pub/536D6C3B-2354-D714-5123-0C220D38FEA2 . [Accessed: Nov. 17, 2016].

[15] B. Owens, "The Rise of Distributed Power," General Electric Company, 2014. [Online]. Available: https://www.ge.com/sites/default/files/2014%2002%20Rise%20of%20Distributed%20Power.pdf. [Accessed: June 05, 2016].

[16] National Grid, “Chapter 4 - System Inertia: System Operability Framework 2015,” National Grid, Nov. 2015. [Online]. Available: http://www2.nationalgrid.com/UK/Industry-information/Future-of-Energy/System-Operability-Framework/ . [Accessed: Oct. 1, 2016].

[17] H. Jain, A. Parchure, R. P. Broadwater, M. Dilek and J. Woyak, "Three-Phase Dynamic Simulation of Power Systems Using Combined Transmission and Distribution System Models," in *IEEE Transactions on Power Systems*, vol. 31, no. 6, pp. 4517-4524, Nov. 2016. doi: 10.1109/TPWRS.2016.2535297

[18] R.S. Thallam, S. Suryanarayanan, G.T. Heydt, and R. Ayyanar, "Impact of Interconnection of Distributed Generation on Electric Distribution Systems – A Dynamic Simulation Perspective,” in *Proceedings 2006 IEEE Power Engineering Society General Meeting*, 18-22 June 2006. doi: 10.1109/PES.2006.1709140

[19] Z. Miao, M.A. Choudhry, and R.L. Klein, "Dynamic simulation and stability control of three-phase power distribution system with distributed generators," in *Proceedings IEEE Power Engineering Society Winter Meeting*, 27-31 Jan, 2002. doi: 10.1109/PESW.2002.985165

[20] B.W. Lee and S.B. Rhee, "Test requirements and performance evaluation for both resistive and inductive superconducting fault current limiters for 22.9 kV Electric Distribution Network in Korea," *IEEE Transactions on Applied Superconductivity*, vol. 20, no. 3, pp. 1114-1117, June 2010. doi: 10.1109/TASC.2010.2040256

[21] E. Nasr-Azadani, C.A. Canizares, and K. Bhattacharya, "Modeling and stability analysis of distributed generation," in *Proceedings IEEE Power and Energy Society General Meeting*, 22-26 July 2012. doi: 10.1109/PESGM.2012.6345141

[22] E. Nasr-Azadani, C.A. Canizares, D.E. Olivares, and K. Bhattacharya, "Stability analysis of unbalanced distribution systems with synchronous machine and DFIG based distributed generators," in *IEEE Transactions on Smart Grid*, vol.5, no. 5, pp. 2326-2338, Sept. 2014. doi: 10.1109/TSG.2014.2321709

[23] I. Xyngi, A. Ischenko, M. Popov, and L. van der Sluis, "Transient stability analysis of a distribution network with distributed generators," in *IEEE Transactions on Power Systems*, vol. 24, no. 2, pp. 1102-1104, May 2009. doi: 10.1109/TPWRS.2008.2012280

[24] M. Reza, J.G. Slootweg, P.H. Schavemaker, W.L. Kling, and L van der Sluis., "Investigating impacts of distributed generation on transmission system stability," in *Proceedings IEEE Bologna Power Tech Conference*, 23-26 June 2003. doi: 10.1109/PTC.2003.1304341

[25] S. Achilles, S. Schramm, and J. Bebic, "Transmission System Performance Analysis for High-Penetration Photovoltaics," National Renewable Energy Laboratory, NREL/SR-581-42300, Feb. 2008. [Online]. Available: https://www1.eere.energy.gov/solar/pdfs/42300.pdf. [Accessed: June 05, 2016].

[26] N.W. Miller, M. Shao, S. Pajic, and R. D'Aquila, "Western Wind and Solar Integration Study Phase 3-Frequency Response and Transient Stability," National Renewable Energy Laboratory, NREL/SR-5D00-62906, Dec. 2014. [Online]. Available: http://www.nrel.gov/docs/fy15osti/62906.pdf . [Accessed: May 16, 2016].

[27] B. Tamimi, C. Cañizares and K. Bhattacharya, "System stability impact of large-scale and distributed solar photovoltaic generation: The case of Ontario, Canada," in *IEEE Transactions on Sustainable Energy*, vol. 4, no. 3, pp. 680-688, July 2013. doi: 10.1109/TSTE.2012.2235151

[28] S. Eftekharnejad, V. Vittal, G. T. Heydt, B. Keel and J. Loehr, "Impact of increased penetration of photovoltaic generation on power systems," *IEEE Transactions on Power Systems*, vol. 28, no. 2, pp. 893-901, May 2013. doi: 10.1109/TPWRS.2012.2216294

[29] Y. T. Tan and D. S. Kirschen, "Impact on the Power System of a Large Penetration of Photovoltaic Generation," *in Proceedings PES General Meeting,* 24-28 June 2007. doi: 10.1109/PES.2007.385563

[30] H. Liu, L. Jin, D. Le and A. A. Chowdhury, "Impact of high penetration of solar photovoltaic generation on power system small signal stability," in *Proceedings International Conference on Power System Technology (POWERCON),* 24-28 Oct., 2010. doi: 10.1109/POWERCON.2010.5666627

[31] K.P. Schneider, J.C. Fuller, F.K. Turner, and Y. Chen, "Modern Grid Strategy: Enhanced GridLAB-D Capabilities Final Report," Pacific Northwest National Laboratory, PNNL-18864, Sept. 2009. [Online]. Available: http://www.pnnl.gov/main/publications/external/technical_reports/PNNL-18864.pdf . [Accessed: Oct. 2, 2016].

[32] B. Palmintier, *et al*, "Final Technical Report: Integrated Distribution-Transmission Analysis for very High Penetration Solar PV," National Renewable Energy Laboratory, NREL/TP-5D00-65550, Jan. 2016. [Online]. Available: http://www.nrel.gov/docs/fy16osti/65550.pdf . [Accessed: Oct. 2, 2016].

[33] P. Evans, “Verification of Energynet® methodology,” California Energy Commission, CEC-500-2010-021, Dec. 2010. [Online]. Available: http://www.energy.ca.gov/2010publications/CEC-500-2010-021/CEC-500-2010-021.PDF. [Accessed: Oct. 27, 2015].

[34] S. Zhong and A. Abur, "Effects of nontransposed lines and unbalanced loads on state estimation," in *Proceedings IEEE Power Engineering Society Winter Meeting*, 27-31 Jan. 2002. doi: 10.1109/PESW.2002.985151

[35] K. A. Birt, J. J. Graffy, J. D. McDonald and A. H. El-Abiad, "Three phase load flow program," in *IEEE Transactions on Power Apparatus and Systems*, vol. 95, no. 1, pp. 59-65, Jan. 1976. doi: 10.1109/T-PAS.1976.32077

[36] NERC System Protection and Control Subcommittee, “Power Plant and Transmission System Protection Coordination,” North American Electric Reliability Corporation, Revision 1, July 2010. [Online]. Available: - http://www.nerc.com/docs/pc/spctf/Gen%20Prot%20Coord%20Rev1%20Final%2007-30-2010.pdf. [Accessed: Aug. 23, 2016].

[37] A. P. S. Meliopoulos, B. Fardanesh and S. Zelingher, "Power system state estimation: modeling error effects and impact on system operation," in *Proceedings of the 34th Annual Hawaii International Conference on System Sciences*, 6 Jan. 2001. doi: 10.1109/HICSS.2001.926269

[38] M.M. Adibi, D.P. Milanicz, T.L. Volkmann, "Asymmetry issues in power system restoration," in *IEEE Transactions on Power Systems*, vol.14, no.3, pp.1085-1091, Aug. 1999. doi: 10.1109/59.780930

[39] V. Spitsa, *et al* "Three–Phase Time–Domain Simulation of Very Large Distribution Networks*,"* in *IEEE Trans. Power Delivery*, vol.27, no. 2, pp.677-687, April 2012. doi: 10.1109/TPWRD.2011.2179069

[40] “DEW/ISM,” Electrical Distribution Design, Inc. (EDD). [Online]. Available: http://www.edd-us.com/dewism/ . [Accessed: Nov. 17, 2016].

[41] M. Dilek, F. de Leon, R. Broadwater and S. Lee, "A Robust Multiphase Power Flow for General Distribution Networks," in *IEEE Transactions on Power Systems*, vol. 25, no. 2, pp. 760-768, May 2010. doi: 10.1109/TPWRS.2009.2036791

[42] M.W. Davis, R. Broadwater, and J. Hambrick, “Modeling and Testing of Unbalanced Loading and Voltage Regulation,” National Renewable Energy Laboratory, NREL/SR-581-41805. [Online]. Available: http://www.nrel.gov/docs/fy07osti/41805.pdf. [Accessed: Sept. 10, 2016].

[43] R. Broadwater, “Integrated System Models Graph Trace Analysis,” Electrical Distribution Design, Inc. (EDD), 2012. [Online]. Available: http://www.edd-us.com/wp-

content/uploads/2016/09/ISM-GTA%20DEW%20BNL%20Presentation.pdf . [Accessed: Sept. 18, 2016].

[44] H. Jain, K. Rahimi, A. Tbaileh, R. P. Broadwater, A.K. Jain and M. Dilek, "Integrated transmission & distribution system modeling and analysis: Need & advantages," in *Proceedings IEEE Power and Energy Society General Meeting (PESGM)*, 17-21 July 2016. doi: 10.1109/PESGM.2016.7741235

[45] Erwin Kreyszig, "Graphs and Combinatorial Optimization," in Advanced Engineering Mathematics, 8th ed., Singapore, John Wiley & Sons, 1999.

[46] E. Horowitz, S. Sahni, and S. Rajasekaran, "Elementary Data Structures," in *Computer Algorithms C++: C++ and Psuedocode Versions*, New York, Computer Science Press, 1997.

[47] W.D. Willis, "Trees," in *A Beginner's Guide to Graph Theory*, 2nd ed., Boston, Birkhauser, 2007.

[48] P.W. Sauer and M.A. Pai, "Multimachine Dynamic Models," in Power System Dynamics and Stability", Champaign, Stipes Publishing LLC, 2006.

[49] IEEE 39 Bus System, Illinois Center for a Smarter Electric Grid (ICSEG). [Online]. Available: http://publish.illinois.edu/smartergrid/ieee-39-bus-system. [Accessed: Nov. 17, 2016].

[50] A. Medina et al., "Harmonic Analysis in Frequency and Time Domain," in *IEEE Transactions on Power Delivery*, vol. 28, no. 3, pp. 1813-1821, July 2013. doi: 10.1109/TPWRD.2013.2258688

[51] P. W. Sauer and M. A. Pai, "Power system steady-state stability and the load-flow Jacobian," in *IEEE Transactions on Power Systems*, vol. 5, no. 4, pp. 1374-1383, Nov. 1990. doi: 10.1109/59.99389

[52] Electromagnetic Transients Program (EMTP) Theory Book, Bonneville Power Administration (BPA), Portland, OR, 1986.

[53] H. Jain, A. Parchure, R.P. Broadwater, M. Dilek and J. Woyak, "Three phase dynamics analyzer - a new program for dynamic simulation using three phase models of power systems," presented at the IEEE ICPS/PCIC Conference, Hyderabad, India, 19-21 Nov. 2015.

[54] F. Lee and R. Broadwater, "Distributed algorithms with theoretic scalability analysis of radial and looped load flows for power distribution systems," in *Electric Power Systems Research*, vol. 65, no. 2, pp. 169-177, May, 2003. http://dx.doi.org/10.1016/S0378-7796(03)00021-X

[55] R. H. Salim and R. A. Ramos, "Analyzing the effect of the type of terminal voltage feedback on the small signal dynamic performance of synchronous generators," in *Proceedings Bulk*

*Power System Dynamics and Contro*l, i*REP Symposium*, 1-6 Aug. 2010. doi: 10.1109/IREP.2010.5563298

[56] *IEEE Recommended Practice for Excitation System Models for Power System Stability Studies*, IEEE Standard 412.5-2005, pp.1-93, Apr. 2006. doi: 10.1109/IEEESTD.2006.99499

[57] Task Force on Turbine-Governor Modeling, "Dynamic Models for Turbine-Governors in Power System Studies", IEEE Power and Energy Society, Technical Report PES-TR1, January 2013. [Online]. Available: http://resourcecenter.ieee-pes.org/pes/product/technical-publications/PESTR1 [Accessed: Nov. 18, 2017].

[58] Energy Information Administration, "Wind and Solar Data and Projections from the U.S. Energy Information Administration: Past Performance and Ongoing Enhancements," US Energy Information Administration, Mar. 22, 2016. [Online]. Available: https://www.eia.gov/forecasts/aeo/supplement/renewable/ . [Accessed: Oct. 11, 2016].

[59] V. Brandwajn, W. S. Meyer and H. W. Dommel, "Synchronous Machine Initialization for Unbalanced Network Conditions within an Electromagnetic Transients Program," *in Proceedings Power Industry Computer Applications Conference*, 15-19 May 1979. doi: 10.1109/PICA.1979.720043

[60] *IEEE Standard for Cylindrical-Rotor 50 Hz and 60 Hz Synchronous Generators Rated 10 MVA and Above,* IEEE Standard C50.13-2014 (Revision of IEEE Std C50.13-2005), pp.1-63, May 9 2014. doi: 10.1109/IEEESTD.2014.6811137

[61] F. Ghassemi and M. Perry, "Review of Voltage Unbalance Limit in the GB Grid Code CC.6.1.5 (b)," National Grid, Oct. 2014. [Online]. Available: http://www2.nationalgrid.com/WorkArea/DownloadAsset.aspx?id=37643. [Accessed: Nov. 17, 2016].

[62] Shaimaa Abd Alla Omran, "Control Applications and Economic Evaluations of Distributed Series Reactors in Unbalanced Electrical Transmission Systems," Ph.D. dissertation, Virginia Polytechnic Institute and State University, Blacksburg, 2015. [Online]. Available: https://vtechworks.lib.vt.edu/handle/10919/52240. [Accessed: Nov. 17, 2016].

[63] K. Rahimi, H. Jain and R. Broadwater, "Application of Distributed Series Reactors in relieving congestion costs," in *Proceedings IEEE/PES Transmission and Distribution Conference and Exposition (T&D)*, 3-5 May 2016. doi: 10.1109/TDC.2016.7519898

[64] K. Rahimi, H. Jain, R. Broadwater and J. Hambrick, "Application of Distributed Series Reactors in voltage balancing," in *Proceedings IEEE Power & Energy Society General Meeting*, 26-30 July 2015. doi: 10.1109/PESGM.2015.7286015

[65] Western Electricity Coordinating Council Modeling and Validation Work Group, "WECC solar plant dynamic modeling guide," Western Electricity Coordinating Council, Apr. 2014. [Online]. Available:

https://www.wecc.biz/_layouts/15/WopiFrame.aspx?sourcedoc=/Reliability/WECC%20Solar%20Plant%20Dynamic%20Modeling%20Guidelines.pdf&action=default&DefaultItemOpen=1. [Accessed: Feb. 18, 2016].

[66] E. Muljadi, M. Singh, and V. Gevorgian, "User guide for PV dynamic model simulation written on PSCAD platform," National Renewable Energy Laboratory, NREL/TP-5D00-62053, Nov. 2014. [Online]. Available: http://www.nrel.gov/docs/fy15osti/62053.pdf. [Accessed: Feb. 20, 2016].

[67] J. A. Nelson, "Effects of cloud-induced photovoltaic power transients on power system protection," Master of Science Thesis, Department of Electrical Engineering, California Polytechnic State University, San Luis Obispo, 2010. [Online]. Available: http://digitalcommons.calpoly.edu/theses/430/ . [Accessed: Feb. 19, 2016].

[68] E. Muljadi, M. Singh, and V. Gevorgian, "PSCAD Modules Representing PV Generator," National Renewable Energy Laboratory, NREL/TP-5500-58189, Aug. 2013. [Online]. Available http://www.nrel.gov/docs/fy13osti/58189.pdf . [Accessed: March 01, 2016].

[69] C. Schauder, "Advanced inverter technology for high concentration levels of PV generation in distribution systems," National Renewable Energy Laboratory, Mar. 2014. [Online]. Available NREL website: http://www.nrel.gov/docs/fy14osti/60737.pdf. [Accessed: Nov. 1, 2015].

[70] D.J. Rincón, M.A. Mantilla, J. F. Petit, G. Ordóñez, and O. Sierra, "Control of Three Phase Inverters for Renewable Energy Systems under Unbalanced Grid Voltages," International Journal of Renewable Energy Research, vol. 5, no. 2, 2015.

[71] R.A. Gannett, "Control Strategies for High Power Four-Leg Voltage Source Inverters," Master of Science Thesis, Virginia Polytechnic Institute and State University, Blacksburg, 2001. [Online]. Available: https://theses.lib.vt.edu/theses/available/etd-07302001-133659/ . [Accessed: Mar. 01, 2016].

[72] E. Muljadi, M. Singh, R. Bravo, and V. Gevorgian, "Dynamic model validation of PV inverters under short-circuit conditions," in *Proceedings IEEE Green Technologies Conference*, 4-5 Apr. 2013. doi: 10.1109/GreenTech.2013.23

[73] Electronic Code of Federal Regulations (Title 10, Chapter 11, Subchapter D, Part 431, Subpart K-Distribution Transformers), US Department of Energy. [Online]. Available: http://www.ecfr.gov/cgi-bin/text-idx?SID=fb9b81787f3d7d4d7c453df82505b3aa&mc=true&node=sp10.3.431.k&rgn=div6%20-%20se10.3.431_1196 . [Accessed: Nov. 17, 2016].

[74] L. Pereira, J. Undrill, D. Kosterev, and S. Patterson, "A New Thermal Governor Modeling Approach in the WECC," in *IEEE Transactions on Power Systems*, vol. 18, no. 2, pp. 819-829, May 2003. doi: 10.1109/TPWRS.2003.811007.

[75] MathWorks, "250-kW Grid-Connected PV Array," [Online]. Available: http://www.mathworks.com/help/physmod/sps/examples/250-kw-grid-connected-pv-array.html . [Accessed: Nov. 17, 2016].

[76] Distribution Test Feeders (123-bus Feeder), IEEE Power and Energy Society. [Online]. Available: http://www.ewh.ieee.org/soc/pes/dsacom/testfeeders/index.html. [Accessed: Oct. 31, 2015].

[77] "Voltage Tolerance Boundary," Pacific Gas and Electric Company, Jan. 1999. [Online]. Available: http://www.pge.com/includes/docs/pdfs/mybusiness/customerservice/energystatus/powerquality/voltage_tolerance.pdf. [Accessed: Nov. 11, 2016].

[78] *Generator Frequency and Voltage Protective Relay Settings*, NERC Std. PRC-024-2, May 2015. [Online]. Available: http://www.nerc.com/pa/Stand/Generator%20Verification%20Project%20200709%20Related%20File/PRC-024-1_WebEx_Slides_2009Feb26.pdf . [Accessed: Nov. 17, 2016].

[79] *IEEE Standard for Interconnecting Distributed Resources with Electric Power Systems - Amendment 1*, IEEE Std 1547a-2014 (Amendment to IEEE Std 1547-2003), pp.1-16, May 21 2014. doi: 10.1109/IEEESTD.2014.6818982

APPENDIX: REUSE OF IEEE ARTICLES

This dissertation has reused some portions of articles, which the author published with IEEE as the first author. The reuse is as per the IEEE reuse policy for Thesis and Dissertation, according to which a formal reuse license is not required to be obtained. At the time of writing of the dissertation, the policy is available here: https://www.ieee.org/publications_standards/publications/rights/permissions_faq.pdf. A snapshot of the relevant section from the above pdf is given below:

- **Does IEEE require individuals working on a thesis or dissertation to obtain formal permission for reuse?**

The IEEE does not require individuals working on a thesis to obtain a formal reuse license, however, you must follow the requirements listed below:

Textual Material

Using short quotes or referring to the work within these papers) users must give full credit to the original source (author, paper, publication) followed by the IEEE copyright line © 2011 IEEE.

In the case of illustrations or tabular material, we require that the copyright line © [Year of original publication] IEEE appear prominently with each reprinted figure and/or table.

If a substantial portion of the original paper is to be used, and if you are not the senior author, also obtain the senior author's approval.